UNIVERSITÀ DI PARMA

UNIVERSITA' DEGLI STUDI DI PARMA

DOTTORATO DI RICERCA IN FISICA

CICLO XXXV

GRAPHENE-BASED MATERIALS FOR APPLICATION IN INNOVATIVE SUPERCAPACITORS

Coordinatore:

Chiar.mo Prof. Carretta Stefano

Supervisore:

Chiar.mo Prof. Daniele Pontiroli

Dottorando: Morenghi Alberto

Anni Accademici 2019/2020 – 2021 /2022

"A plausible future requires factual present"

Snyder, 2018

INDEX

1. INTRODUCTION

1.1. Background

The glaciers are melting, the level of the seas is growing, the desertification is advancing, natural disasters are increasingly common. They are consequences of the Earth temperature growth driven by the greenhouse gas emissions. The energetic production is responsible for the 87% of global greenhouse gas emissions, which are divided unequally between countries. There is a correlation between the wellness and the CO_2 emissions; since the current technology relies most on the use of fossil fuels, the poorer countries have the lowest level of emissions, because they lack access to such energy sources and, therefore, they are suffering of energy poverty. On the other hand, in the countries on the right side of Figure 1.1.1, living conditions are better, people are not suffering of energy poverty and, consequently, the greenhouse gas emissions of richest countries are too high to be sustainable. In order to keep the increase of the global average temperature well below 2°C above pre-industrial levels, which is the goal of the Paris Agreement, emissions must fall to the net-zero level within the coming decades. Firstly, it means that richer countries must switch from fossil to sustainable energy sources, maintaining their living conditions. Secondly, that the poorer countries should improve their wellness without increasing their emissions, but this will not be possible until the cheapest energy source is fossil-based [1].

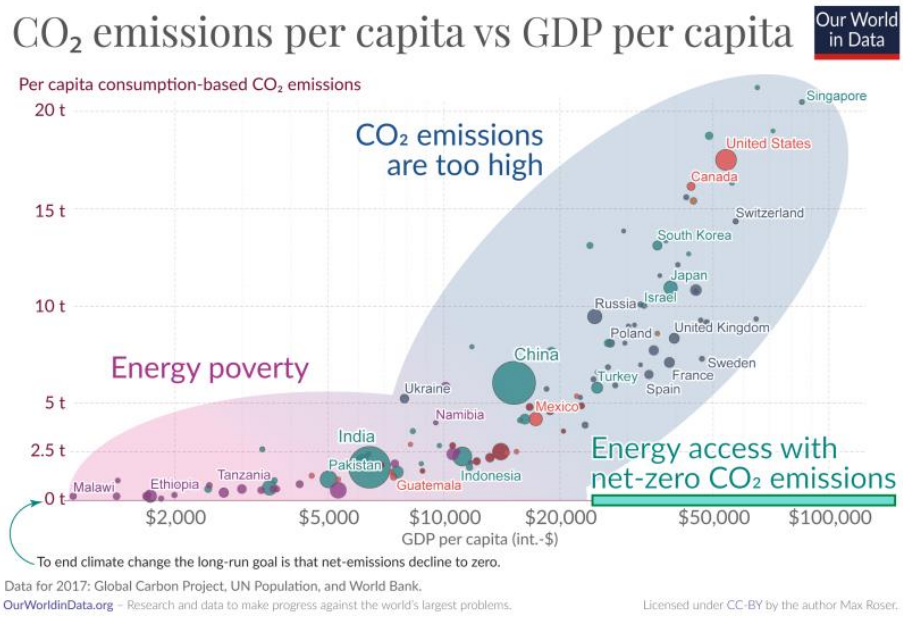

Figure 1.1.1: CO_2 emissions per capita as a function of gross domestic product per capita [1].

The European Parliament and the Council decided on 6 April 2022 for a General Union Environment Action Programme to 2030, confirming the Union's environmental agenda of the 7th EAP focusing on the achievement of climate neutrality by 2050 at the latest. The 8th EAP should accelerate the green transition, to a sustainable, renewable energy-based and competitive circular economy. As decided by the 8th EAP, the energy production from renewable sources is quickly increasing in Europe, relying mostly on the improvement of wind and solar sources, reaching in the 2021 the production of slightly less of 700 TWh, as outlined in figure 1.1.2.

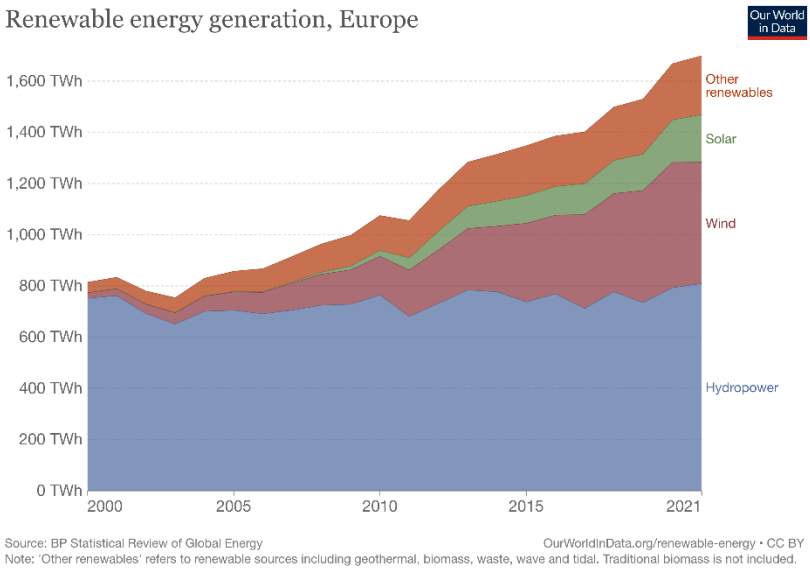

Figure 1.1.2: European renewable energy generation trend between 2000 and 2021 [1].

The use of solar panels and wind turbines is constantly increasing and the amount of renewable energy consumption should reach the 32% of the total within the 2030. On the other hand, these types of sources are suffering of instability since they depend on the weather. In particular, there is a time discontinuity in the power generation. It varies between the night and the day, in the same day and from day to day. This behavior translates into the presence of production peaks and of periods of low power generation, which completely do not match with the electrical grid demand. In order to solve these discontinuity issues, the peak shaving techniques can be used. Peak shaving is a set of strategies, based on energy storage devices, which acts as intermediary between the power generation plant and the consumption users. Precisely, their use enables to reduce the power demand at the highest consumption periods, relying on the energy generated during the low power demand periods [2]. Moreover, the switch between fossil fuels-based market and renewables-based one determines that also the automotive sector, which is responsible for the 16.2% of the greenhouse gas emissions [1], must rely on newly energy storage technology. The current options to directly store electrical energy are batteries and supercapacitors. These two technologies are compared in the Ragone plot in Figure 1.1.3, highlighting the range of the specific power and of the specific energy currently achieved for both of them and their time of charge along the diagonal lines [3].

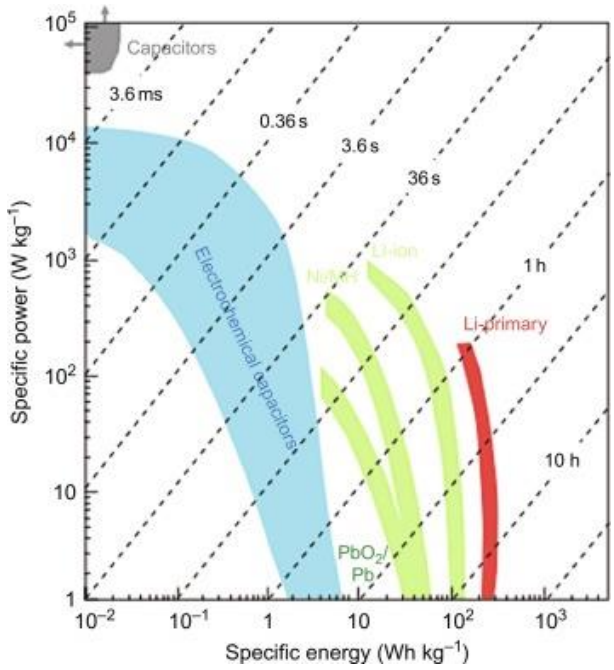

Figure 1.1.3: Ragone Plot: Energy storage devices plotted as a function of specific energy and specific power. [3]

Batteries are based on the electrochemical accumulation of charges through reduction and oxidation bulk reactions occurring in an electrochemical cell. Thanks to their ability of store a high energy amount per kilogram, nowadays rechargeable batteries represent the leading technology for the energy accumulation. On the other side, this technology still has many drawbacks, such as poor cyclability, as it can operate only for few thousands charge/discharge cycles with acceptable capacity retention. Secondly, batteries possess rather low specific energy and power, as compared with fossil fuels; this fact determines the oversizing of battery packs for reaching the required energy and power output demand, further increasing their cost. Moreover, batteries low specific power determines a slow charge rate, which limits the charging time in the order of hours. Lastly, they still display many sustainability, eco-compatibility and safety problems, since they rely on the use of toxic and pollutant elements such us manganese, nickel and cobalt, and on the use highly flammable liquid organic electrolytes [4].

The second option for the energy storage is represented by supercapacitors (SCs), which rely on the electrochemical accumulation of charges that are based on electrostatic and pseudocapacitive effects, instead of bulk redox reactions. Since, from a kinetic point of view, these mechanisms are faster than bulk redox reactions, SCs can achieve higher specific power than batteries, allowing their application wherever a high power, instead of a high energy amount, is needed. For the same reason, they can be charged very quickly, ranging from few seconds to few minutes. Furthermore, their accumulation effects are highly reversible enabling an almost unlimited cyclability. Additionally, the usual materials used have a high degree of eco-compatibility, sustainability and safety. On the other hand, as compared with secondary batteries, they display a limited specific energy.

Currently, SCs find application in the automotive, in the grid, in the renewables and in the industrial sectors. Research is ongoing in order to extend their availability for optimizing the application in combination or in substitution of traditional energy storage devices [5]. Specifically, in the last decade, research focused their efforts towards four specific SC application sectors, highlighted in Figure 1.1.4.

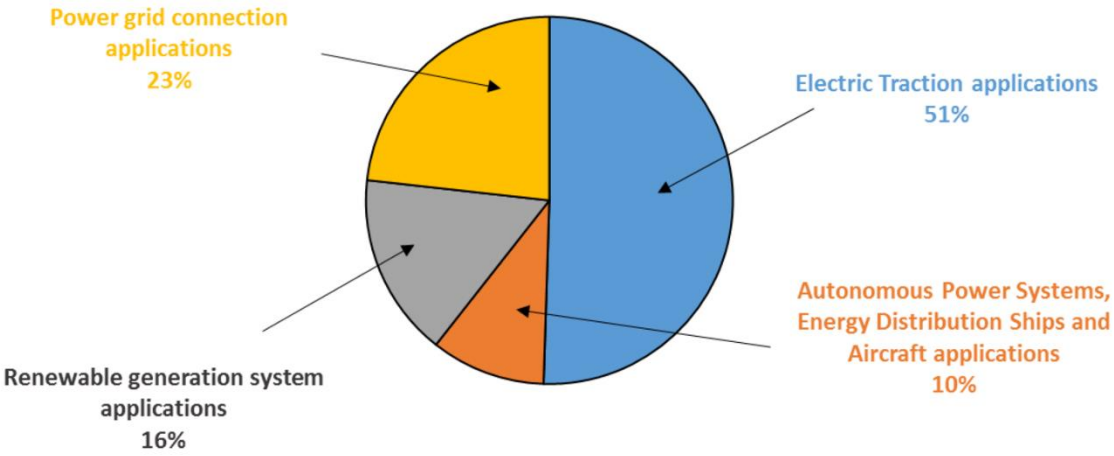

Figure 1.1.4: Classification of the research publications related to supercapacitors in the last decade respect their application.

More in details, in the automotive sector a SC can be coupled with fuel cells or batteries to level the power demand load. When the vehicle is demanding a high power consumption, for example during acceleration or when starting, the SC can support the fuel cell or the battery in supplying the required energy. On the contrary, during low power demand the vehicle is powered by the fuel cell, or the battery, and the SC is charged. This process reduces the power demand to the main powering system, enabling to lower its size with benefits in terms of cost and weight [6–8]. Moreover, using SCs, the voltage fluctuations at the battery electrodes, due for example to the acceleration, are mostly deleted. Thus, SCs reduce the batteries stress, extending their cycle life and efficiency [8]. Tipically, in electric vehicles SCs are used in energy recovery systems, such as regenerative breaking and suspensions. Since these systems, recovering energy from breaking or suspension shocks, produce high power, SCs are the best way to store this energy, to preserve batteries from degradation [9,10].

Regarding renewables and grid systems, SC find application in the peak shaving technology. Since the renewable energy generation suffer of discontinuity, the grid alone does not support the required level of power demand, causing problems such as power failure, instability and voltage fluctuations. The peak shaving technique can solve these grid issues and SCs, thanks to their reversibility and power capability, are valuable candidates, storing energy during periods of high generation and releasing it during high power consumption demand [2,11].

Moreover, SCs, in their miniaturized version, represent an ideal choice to supply energy in the so-called Internet of Things (IoT) applications, such as watches, cloths, shoes and all wearable

consumer technologies. Their role consists in powering sensors, assuring both fast rechargeable times, efficiency and long-life spans. In order to be used at the large scale in IoT sector, micro-SCs need flexible designs and an environmentally friendly nature, therefore using environmental non-dangerous materials [12].
Looking to the future, the enhancement of the specific energy of SCs could allow their use on a large scale, achieving better efficiency, longer lifespan, and higher power than batteries.

1.2 From capacitors to supercapacitors

1.2.1 Dielectric capacitors

An electric capacitor, named first generation capacitor, is a device able to store charge through an electrostatic field. It has a sandwich structure which is composed of two conductive plates enclosing a dielectric or insulator, as shown in Figure 1.2.1. Once an external voltage difference, hence an electrostatic field, is applied across the plates, the positive charges accumulate on one plate (positive electrode) and negative charges accumulate on the other plate (negative electrode). Removing the external voltage difference, the charges remain separated on the plates and the capacitor is charged. The voltage difference between the electrodes is called the cell voltage of the SC. Once the two electrodes are connected by a wire, with or without a load, the charges flow through the wire and the capacitor discharges.

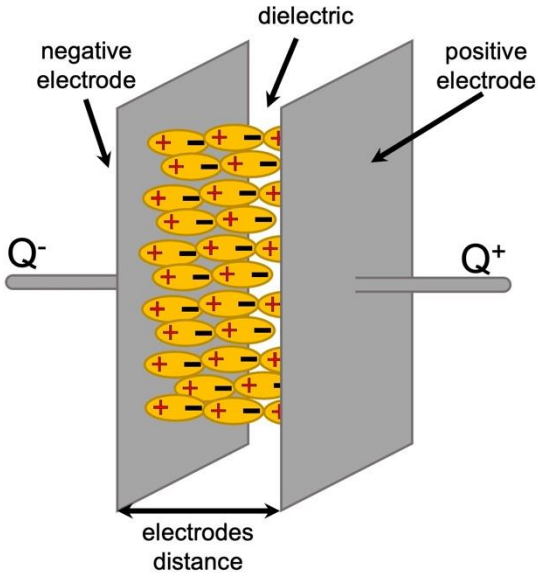

Figure 1.2.1: Dielectric capacitor structure.

$$C = \frac{Q}{\Delta V} = \frac{\varepsilon A}{d} = \frac{\varepsilon_0 \varepsilon_r A}{d} \qquad \textit{Eq. 1}$$

The parameter that describes the ability to store charges is the capacitance *C*, shown in Equation 1, which is dependent on the materials properties and on the geometry. For instance, *A* is the surface area of the plates, *d* is the distance between them and $\varepsilon_0 \varepsilon_r$ are the vacuum electric permittivity and the relative dielectric constant of the dielectric material, respectively. The choice of the dielectric affects the maximum voltage difference that can be applied between the electrodes, since a higher voltage may break the insulation, resulting in a flow of electrons inside of the capacitor and in the device breakdown. An appropriate dielectric material briefly consists of an insulator material, where no charges are moving and, once the voltage is applied, the molecules polarize in the direction of the applied electric field.

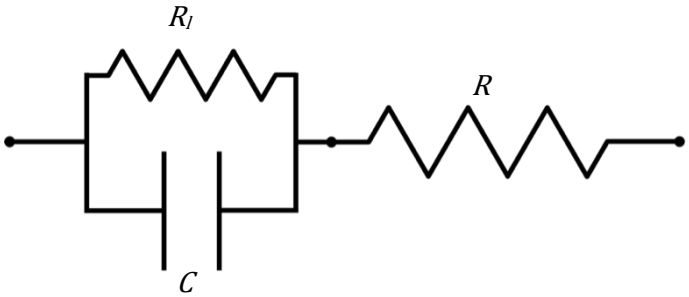

Figure 1.2.2: Equivalent circuit of a real capacitor.

$$I = \frac{V}{R_{tot}} e^{-t/R_{tot}C} \qquad \textit{Eq. 2}$$

The mechanism of charge storage is purely electrostatic, no chemical reaction is involved, therefore the kinetic is fast. Beyond the capacitance, a real capacitor has an intrinsic resistance (R_l) in parallel with the capacitance, dependent on the dielectric material, and another resistance (R) in series, which relies on the electrode contacts and on the capacitor materials. Its equivalent circuit is described by Figure 1.2.2. During charging and discharging phases, closing the circuit on a generator or on a load, the current which flows is described by the Equation 2, where V is the applied voltage, R_{tot} is the total series resistance (eventually the load resistance plus the capacitor series resistance), C is the capacitance and t is the time. $R_{tot}C$ is an important parameter of a capacitor which is named time constant, and consists in the time necessary for charging and discharging the device up to 63%. Since the area of the plates is of 10^{-3} m^2 magnitude order, the distance between the electrodes is around 10^{-4} m and the dielectric constant is between 10^{-12} and 10^{-7}, following the equation 1, the capacitance falls in the range 10^{-6}-10^{-12} F depending mainly on the dielectric material used. Capacitor capacitance common values are listed in the table 1.1.

Table 1.1: Characteristics of common dielectric materials used in capacitors.

Material	***Capacitance (F)***	***Relative dielectric constant*** ε_r	***Dielectric strength (MV/m)***
Air	$10^{-10} - 10^{-9}$	1.0005	3
Paper	$10^{-9} - 10^{-6}$	$2 - 6$	16
Glass	$10^{-12} - 10^{-10}$	$4.8 - 8$	$9 - 20$
Mica	$10^{-9} - 10^{-6}$	7	118
Ceramics	$10^{-13} - 10^{-5}$	$12 - 400{,}000$	very high values

The dielectric strength defines which is the maximum voltage applicable between the electrodes without undergoing into dielectric electrical breakdown, which consists in the rising of an electrically conductive path through the dielectric and therefore, in the runaway of the device. The resistance in parallel of the capacitor in the Fig. 1.2.2 is the source of the leakage current which is dependent on the insulation resistance and induce self-discharging processes.

(a) $$E = \frac{1}{2} C \Delta V^2$$

(b) $$P = \frac{1}{2} I \Delta V$$

Eq. 3

Capacitors find application in almost every electronic and electrical system for a fast energy storage, which is proportional to the capacitance following equation 3a. Moreover, since the self-discharging current is comparable with their capacitance, capacitors cannot maintain the stored energy for a long time. For these reasons, they are not used for the purpose of storing energy for long time, but they find application as a circuital component and or in high power systems since they feature a high-power capability, evaluated through equation 3b.

1.2.2 Electrolytic capacitors

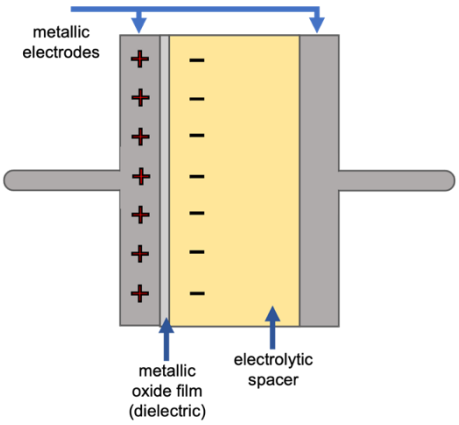

Figure 1.2.3: Electrolytic capacitor scheme.

An electrolytic capacitor is a particular type of polarized capacitor that has high capacitance values. It consists of a metallic electrode (typically aluminum, niobium, or tantalum), a thin oxide film of the same metal as a dielectric and a semi-liquid electrolyte which acts as the second electrode (typically the anode). Since the thickness of the metal oxide is typically few nanometers, the capacitance value reaches some Farads per device. Being the energy proportional to the capacitance following equation 3, electrolytic capacitors are able to achieve a capacitance up to few Farads. Electrolytic capacitors embody the second-generation capacitors.

1.3 Electrochemical double-layer supercapacitors

Electrochemical double-layer SCs represent the third generation capacitors. They are composed by two porous electrodes parted by a separator soaked with an electrolyte, as described by Figure 1.3.

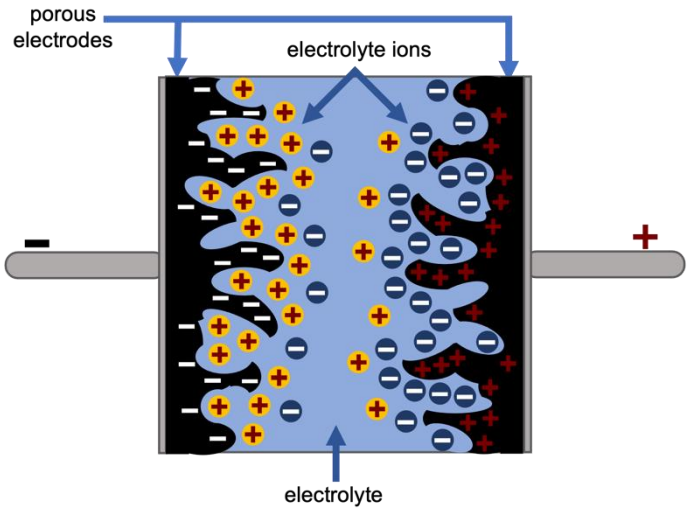

Figure 1.3: Electrochemical double-layer supercapacitor scheme.

Once the voltage is applied between the electrodes, the electrolyte ions approach the surface of the electrodes balancing the charges accumulated on the electrode and forming an electrical double-layer. The electrical double-layer and its theory are at the bases of SC application.

Since the capacitance is proportional to the area exposed to the electrolyte following equation 2, most of the SCs use activated carbons as electrodes, which consist of a highly disordered porous carbon matrix with high surface area [13]. Beside activated carbons, also graphene gained a growing attention, thanks its high surface area, hierarchical porosity and good conductivity. As far as the electrolyte is concerned, a wide range is available, ranging from aqueous to organic and ionic liquids [14,15]. Even though the SCs have greater capacitances with respect common capacitors, they can store a smaller energy amount than batteries. Therefore, to close the stored energy distance between batteries and SCs, many strategies are pursued. Firstly, the introduction of redox reactions, such as pseudocapacitive effects or battery-like reactions, enable to enhance the specific energy. Pseudocapacitive effects are fast redox reactions localized at the electrode surface, which do not slow the kinetics of the charge accumulation. They rely on uncommon metals, such as ruthenium, molybdenum and

manganese in their oxidized forms, and on conductive redox active polymers. Battery-like reactions, on the other way, tend to slow down the kinetics, which should be controlled by a good dispersion and by the nano-engineering of redox active metals in carbon matrix. Such SCs are named hybrid SCs. Recently, the class of hybrid SCs has been parted into hybrid capacitors based on pseudocapacitive effects and on the so called supercapatteries, which are hybrid SCs relying on battery-like reactions [16–18]. Furthermore, the specific energy can be enhanced designing asymmetric SCs. This peculiar strategy, coupling two different electrode materials, enables to enlarge the working voltage window and therefore the stored energy following equation 3 (a) [19]. Each aspect, briefly described here, will be further explored in the next chapter.

1.4 Graphene

Electrodes play a fundamental role in SCs. For instance, conductive materials with high surface areas and a porosity, ranging from the nano to the micro scale, are needed for the electrodes. In fact, carbon-based materials, owning very high specific surface areas and a wide ranged porosity, are mainly used. Among these, graphene exhibits an enormous potential, having a theoretical specific surface area of 2600 m^2/g and a very good electrical conductivity. In particular, bulk graphene produced by scalable and cost-effective methods, such as the thermal exfoliation of graphite oxide (TEGO) or the photo-thermal conversion to graphene of suitable precursors with the use of laser (LIG), presents good conductive properties and a hierarchical porosity, fitting with the SC electrodes requirements. Furthermore, both TEGO and LIG can be easily decorated with metal, metal oxides and other nanoparticles, whose presence can strongly enhance the stored energy. These materials will be described in depth in the fourth chapter.

1.5 Redox-active materials

In order to enhance the specific energy stored in SCs, redox-active materials can be used. In this work we investigated the effect of the decoration of graphene with $Ni(OH)_2$ and TiO_2 nanoparticles on the electrochemical performance of hybrid supercapacitors.

Recently, the interest of the scientific community on $Ni(OH)_2$ based electrode materials has greatly increased, due to its high theoretical capacity, low cost, high chemical stability, well defined redox transitions, high rate performance. Typically, $Ni(OH)_2$-based positive electrodes are coupled with negative carbon electrodes in asymmetric devices operating with aqueous electrolytes [20,21].

On the other hand, TiO_2, which is a well known anode material for Li-ion batteries, can display fast and reversible surface or near-surface redox reactions, hence it is considered a promising material for SCs. Furthermore, it recently gained a growing attention, due to its high specific energy density, low cost, non-toxicity, environmental friendliness, and abundant availability.

1.6 Aim of the thesis

As previously discussed, SCs have the potential to be largely applied for energy storage applications, either alone or coupled with batteries, but their energy capability must be enhanced for closing the energy-gap with batteries [22]. Based on this premise, strong research for newly nanostructured electrode materials and high specific energy SCs must be pursued. The aim of this thesis is to investigate **graphene-based materials** for the application in the **SC electrodes** exploiting **different strategies and SC designs**. In this thesis, the properties of graphene related materials and their application in different typologies of SC are investigated to increase their energy storage capacity. The materials and typologies of SC explored and discussed are:

- **Asymmetric and hybrid supercapacitor based on TEGO decorated with nickel nanoparticles**. This work exploits two different strategies for enhancing the specific stored energy. The first strategy relies on the introduction of battery-like redox reactions in the cathode, through the decoration of TEGO with nickel nanoparticles

uniformly dispersed in the carbon matrix. Thanks to the high reactivity of Ni nanoparticles, it is easy to convert them in the Ni(OH)2 redox active material. The second one relies on the coupling of the battery-like positive electrode with a pure capacitive TEGO, therefore, building an asymmetric device, with the aim to enlarge the working voltage window using an aqueous electrolyte.

- **Microsupercapacitors based on laser induced graphene and laser induced graphene decorated with titanium dioxide**. The aim of this work is to build planar, flexible and highly scalable micro-SCs based on the laser induced graphene technology. Two types of SCs are explored. The former is a symmetric SC with both the electrodes made from pure laser induced graphene. The latter is a symmetric hybrid SC where both the electrodes are made of titanium dioxide decorated laser induced graphene.
- **Lithium-ions capacitors based on TEGO**. The aim of this work is to build a completely TEGO-based capacitor exploiting the wide voltage window assured by an organic lithium-based electrolyte and approaching the conditions used in batteries. Specifically, TEGO is used both as a purely capacitive material and as a source of redox reactions in an asymmetric hybrid capacitor design.

2. THEORY OF SUPERCAPACITORS

This chapter will be dedicated to the deepening of the of SCs properties beginning from their fundamental theory, i.e. the electrical double layer, until their late hybridizations with battery-like materials. In fact, besides the ideal SCs based only on electrostatic effects, their family includes a wide range of devices. In particular, the name SC is used, so far, also for those devices that uses hybrid materials, thus exploiting the electric double layer coupled with pseudocapacitive and diffusion-controlled processes.

2.1. Electrochemical double-layer theory

The electrical double-layer model was initially proposed by Helmholtz and successively developed by Gouy, Chapman, Grahame and Stern. The Grahame-Stern model combines the previous one and describes in detail the electrical double layer occurring at the electrode-electrolyte interface. Grahame and Stern described the electrode-electrolyte system parting it in different layers outlined in figure 2.1.1. The Helmholtz layer comprises the electrode charges and the first array of ions with their solvation sphere radius. In order to describe the possible ions specific absorption at the surface, it is parted in the *inner Helmholtz plane* (IHP), which comprises the electrode charges and the first array of the electrolyte molecules and ions without the solvation sphere, and in the *outer Helmholtz plane* (OHP), which comprises the remaining part of the HL. In both these layers, the net charge ion concentration is high, and they are packed near the electrode surface and into the pores. Outer from the Helmholtz layer, begins the *diffuse layer* (DL), where the ions are more diffuse, thus there is a lower net charges ions concentration. Such layer, with thickness L_{diff}, is delimited by the HL and the bulk electrolyte, where both positive and negative ions are present in equal concentration.

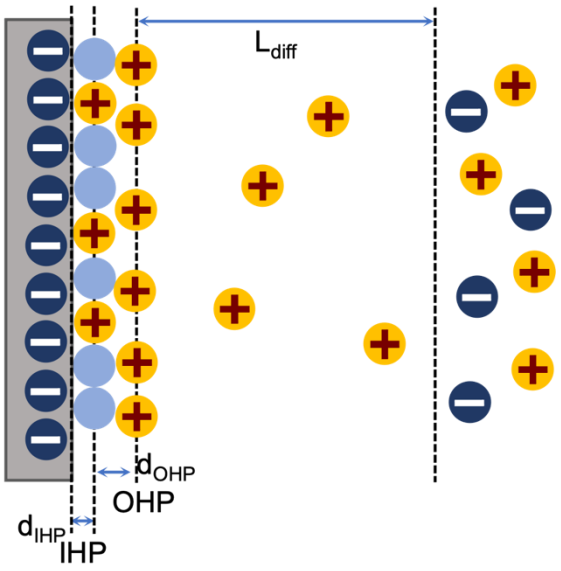

Figure 2.1.1: Graham-Stern model of the electrical double-layer. d_{IHP} and d_{OHP} are the thickness of the inner Helmholtz plane and outer Helmholtz plane, respectively. L_{diff} represents the thickness of the diffuse layer.

The potential drop across the electrical double-layer and, therefore, its capacitance, are dependent on the charge carried by the ions (z), on the dielectric constant ($\varepsilon_r\varepsilon_0$) and on the concentration of the electrolyte (C^0). More in detail, the total potential drop $\Delta\Psi$ across the electrical double-layer can be divided into the potential drop $\Delta\Psi_{HL}$ between the outer electrode surface and the end of the Helmholtz layer, and the potential cross across the diffuse layer $\Delta\Psi_{diff}$, following equation 2.1.

$$\Delta\Psi = \Delta\Psi_{HL} + \Delta\Psi_{diff} \qquad \textit{Eq. 2.1}$$

Therefore, the electrical double-layer can be seen as two series capacitors and its total theoretical differential capacitance (C_{dl}) is described by equation 2.2.

$$C_{dl} = \frac{C_{HL}C_{diff}}{C_{HL} + C_{diff}} \qquad \textit{Eq. 2.2}$$

In the approximation of no specific ion absorption at the electrode surface, i.e. without any chemical reaction, the thickness and the differential capacitance of the Helmholtz layer is constant as a function of the potential. On the other hand, the differential capacitance of the diffuse layer is strongly dependent on the potential drop as shown by equation 2.3. Both the differential capacitances (C_{HL},C_{diff}) are functions of the electrolyte concentration, of the dielectric constant and of the charges number carried by ions. The behavior of the capacitance

as a function of the potential drop across the diffuse layer and of the electrolyte concentration is outlined in Figure 2.1.2.[23]

$$C_{dl} = \frac{C_{HL}\frac{|z|F}{2RT}\sqrt{2\varepsilon_r\varepsilon_0 RTC^0}\left[exp\left(\frac{|z|F}{2RT}\Psi_{dl}\right) + exp\left(-\frac{|z|F}{2RT}\Psi_{dl}\right)\right]}{C_{HL} + \frac{|z|F}{2RT}\sqrt{2\varepsilon_r\varepsilon_0 RTC^0}\left[exp\left(\frac{|z|F}{2RT}\Psi_{dl}\right) + exp\left(-\frac{|z|F}{2RT}\Psi_{dl}\right)\right]} \qquad \textit{Eq. 2.3}$$

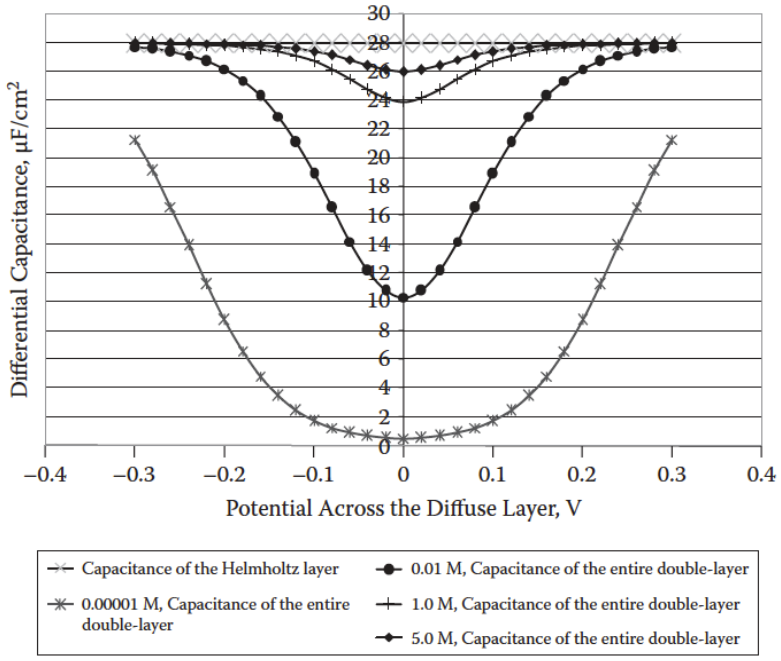

Figure 2.1.2: Differential capacitance as a function of the potential drop across the diffuse layer at four concentrations of the electrolyte according to the equation 2.3. It was assumed a Helmholtz layer differential capacitance of 28 μF/cm², a relative dielectric constant of 40, a charge number carried by ions of 1 and at temperature and pressure room conditions. [19]

In a very dilute electrolyte solution, the differential capacitance of the double-layer is much smaller than that of the Helmholtz layer and closer to the diffuse layer one. However, with a highly concentrated electrolyte the differential capacitance of the diffuse layer is much higher than that of the Helmholtz and, therefore, the entire double-layer capacitance is close to the Helmholtz layer one. In conclusion, higher concentration, dielectric constant, and ion charges carried drive to maximize the overall capacitance.

2.2. Supercapacitor equivalent circuit

Ideally, a SC is composed by two electrodes with a double-layer capacitance, then it can be rationalized as two capacitors in series. Since the electrode material and the electrolyte are not ideal, in the equivalent circuit of a real SC we must add a resistance in parallel with the capacitors and a resistance in series with them, as shown in figure 2.2.1.

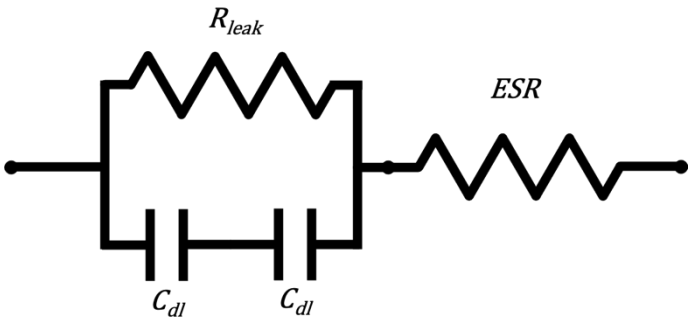

Figure 2.2.1: Equivalent circuit of a real supercapacitor.

The parallel resistance is named leakage resistance (R_{leak}), while the series resistance is named equivalence series resistance (*ESR*). A SC with electrodes with the same charge capability ($C_+ = C_-$) has a total capacitance (C_{dl}^T) equal to half of a single electrode capacitance ($C_\pm$), following equation 2.4, which describes the equivalent capacitance associated at the equivalent circuit in figure 2.2.1.

$$C_{dl}^T = \frac{C_+ C_-}{C_+ + C_-} = \frac{C_\pm^2}{2C_\pm} = \frac{C_\pm}{2} \qquad \textit{Eq. 2.4}$$

In an ideal SC, the charges are not crossing the double-layer interface when any chemical reactions occur. However, in a real electrochemical SC, there exists a leakage current density due to undesired reactions that occur at the interface electrode-electrolyte where charge exchange processes are involved. Since the leakage resistance is normally high implying low leakage current density and since the SCs are charged and discharged with high current density, the presence of a leakage does not affect their normal operation. However, during long storage time, the leakage current can lead the SC to self-discharge, and it is something to pay attention in the evaluation of the performances.

The *ESR* is a real series resistance due to many factors, such as the electrode material and the electrolyte. The *ESR* is also affected by the resistance of the collector contacts with the electrodes and of the external lead contacts with the collectors. The equivalent real

impedance (Z_{real}), i.e. the resistance, calculated for the equivalent circuit in figure 2.2.1 is described by the equation 2.5. For high frequency, the factors associated with the capacitance and with the leakage resistance go to zero and the real impedance goes to the value of the equivalence series resistance. The *ESR* is an important parameter for the evaluation of the performances of SCs and we will focus deeply on it and on its evaluation in the electrochemical impedance spectroscopy section of the methods chapter (see chapter 3).

$$Z_{real} = \sqrt{\left(R_{ESR} + \frac{R_{leak}}{1 + (2\pi f R_{leak} C_{dl}^{T})^2}\right)^2 + \left(\frac{2\pi f R_{leak}^2 C_{dl}^{T}}{1 + (2\pi f R_{leak} C_{dl}^{T})^2}\right)^2} \qquad \textit{Eq. 2.5}$$

2.3. Charging and discharging processes

$$V_{cell} = V_{sc}^{0} + \frac{Q}{C_{dl}^{T}} = V_{sc}^{0} + I_{cell}\frac{t}{C_{dl}^{T}} \qquad \textit{Eq. 2.6}$$

An ideal SC, with no series resistance, no losses, and no faradaic processes, operates following equation 2.6, where V_{sc}^{0} is the SC initial voltage, I_{cell} is the current, t is the time and C_{dl}^{T} is the total double-layer capacitance of the equivalent circuit in figure 2.2.1.

Therefore, with a constant current and an ideal capacitance, which does not depend on the potential difference, the voltage is growing linearly as a function of the time, resulting in a curve with a triangular shape as shown in figure 2.3.1 (a) in black. It is important to note that in a potential step experiment, the capacitive current is directly proportional to the charging-discharging voltage rate, namely the ratio between the voltage and the time.

A real device, which, as mentioned, has a non-zero series resistance and a finite leakage resistance, owes a charging-discharging *V-t* profile which approximate to the triangular shape only for very low R_{ESR} and for very high R_{leak}. The voltage-time relation is described in equations 2.7, which is reduced to the equation 9 for $R_{leak} \rightarrow \infty$ and for $R_{ESR} \rightarrow 0$.

$$V_{cell} = I_{cell}R_{ESR} - V_{sc}^{0} + (V_{sc}^{0} + I_{cell}R_{leak})\left[1 - exp\left(-\frac{t}{R_{leak}C_{dl}^{T}}\right)\right] \qquad \textit{Eq. 2.7}$$

In particular, for non-zero R_{ESR}, a voltage drop (ΔV_{drop}) is occurring at the beginning of each charging or discharging phase which correspond to the double of the cell current multiplied for the equivalent series resistance, as shown in the gray curve of figure 2.3 (a).

On the contrary, a finite leakage resistance is affecting the triangular shape of the charging-discharging curve as seen in figure 2.3 (b). In particular, the charging time increase, and so does the area under the charging curve, while the discharging time and the area enclosed into the discharging curve decrease. These are the footprints that the leakage is hindering the current during the accumulation and lowering the number of charges recovered during the discharging process, following the equation outlined in figure 2.3 (b).

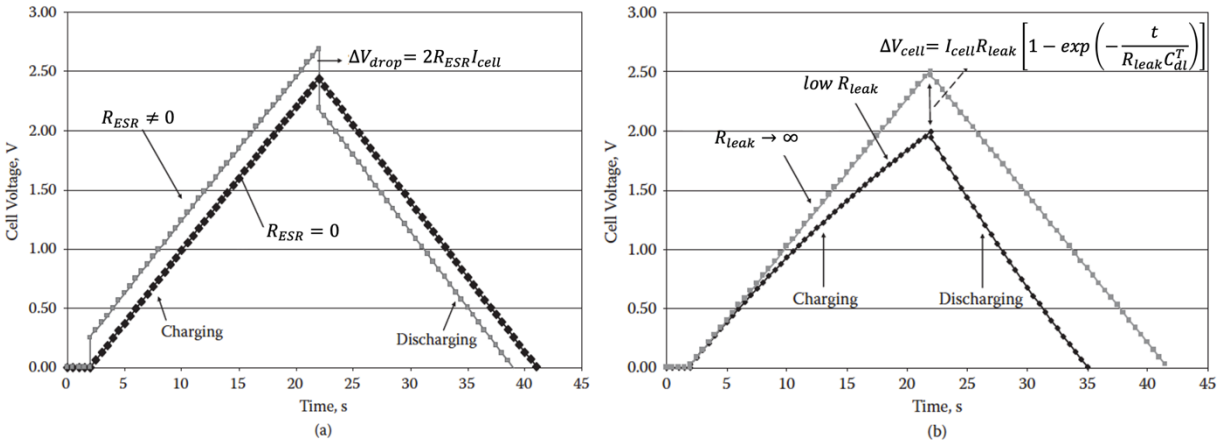

Figure 2.3: Charging-discharging curves of a simulated supercapacitor, following eq. 2.7. The curves outline the resistance-related footprints. Both the capacitance and the module of the current are maintained constant. The sign of the current is changed between the charging and the discharging processes. (a) Outlines the change produced by a non-zero R_{ESR} while the leakage resistance is maintained constant and extremely high. (b) Outlines the change produced by a low R_{leak} while the ESR is maintained constant and extremely low.[17]

2.4. Specific energy and specific power

The specific energy (Es) and the specific power (Ps) are important parameters for evaluating an electrochemical SC performance allowing the comparison with other energy storage devices. In an ideal SC, such as in a capacitor, the energy and the power are evaluated through the equations 1.3 of the Introduction chapter. Regarding a real electrochemical SC, equations

1.3 are no more suitable since the equivalent series resistance affects the specific power, slowing down the charging-discharging rates, and the leakage resistance affects the specific energy, through self-discharging processes, particularly when the storage time is long or when the charging-discharging rates are slow. In general, the equations 1.3 should be substituted by equations 2.5, where the energy is evaluated integrating the voltage, with a constant current, over the charging or discharging time. The relative power is calculated from the ratio between the energy and the time needed for charging or discharging. The maximum power available is limited by the equivalent series resistance following equation 2.8 (c).

$$\text{(a)} \qquad E_S = \frac{1}{M}\int_{t_0}^{t_f} (I\,V)\,dt = \frac{1}{M}C(\Delta V)^2$$

$$\text{(b)} \qquad P_S = \frac{1}{M}\frac{\int_{t_0}^{t_f}(I\,V)\,dt}{\Delta t} = \frac{E_S}{\Delta t} \qquad \textit{Eq. 2.8}$$

$$\text{(c)} \qquad P_{S\,max} = \frac{1}{2M}\frac{\Delta V^2}{R_{ESR}}$$

Hence, in order to increase the specific energy, two ways are available. The first one is to increase the capacitance of the electrochemical SC. Being the capacitance proportional to the available area of the electrodes, this can be obtained using materials with a large surface area, such as porous carbon-based materials, that we will focus on section 2.6. Furthermore, the capacitance can be enhanced introducing redox reactions, such as pseudocapacitive effects or battery-like processes. These types of mechanisms and their related features will be deeply treated in the following section. The second way to enhance the specific energy is to enlarge the working voltage window (*ΔV*) of the device. It depends on the type of the electrolyte, on the electrode materials and on the design of the SC. Section 2.7 and following will be focused on these strategies.

2.5. Pseudocapacitance and battery-like capacity

In the section 2.3, the relation between the voltage difference and the capacitive current was mentioned and it is recalled following in the equation 2.9. The ideal capacitive current is directly proportional to the voltage rate $\Delta V/\Delta t$ and grows linearly with it.

$$I_C = C_{dl}^T \frac{\Delta V_{cell}}{\Delta t} \qquad \textit{Eq. 2.9}$$

This behavior translates experimentally in the figure 2.5 (a) depicting the three-electrodes cyclic voltammetry EDLC curve, which has a quasi-rectangular shape, i.e the capacitive current is constant as a function of the potential. This important technique will be deeply explored in the chapter 3. As previously discussed, the double-layer capacitance is based only on the electrostatic effects that occur at the interface between the electrodes and the electrolyte, precisely between the electrode surface and the ions solvated in the electrolyte.

Beside electrostatic interactions, at the electrode-electrolyte interface, faradaic processes can occur. These reactions can be divided into pseudocapacitive effects and battery-like reactions. The first type consists in localized, superficial fast faradaic reactions that give rise to a pseudocapacitance, which behaves such as a traditional capacitance. The second type basically comprises the same reduction and oxidation (redox) reactions that occur in batteries. Although their nature is similar, battery-like reactions are potential dependent, while pseudocapacitive are not [24]. Normally, performing a three electrodes cyclic voltammetry experiment, redox reactions present at least an oxidation and a reduction peak such as the curve of figure 2.5 (c). That is the case of batteries reactions. Three electrode cyclic voltammetry curve of a pseudocapacitive material does not present any strictly localized peak as shown in figure 2.5 (b), and it is similar to the double-layer capacitive curve [25].

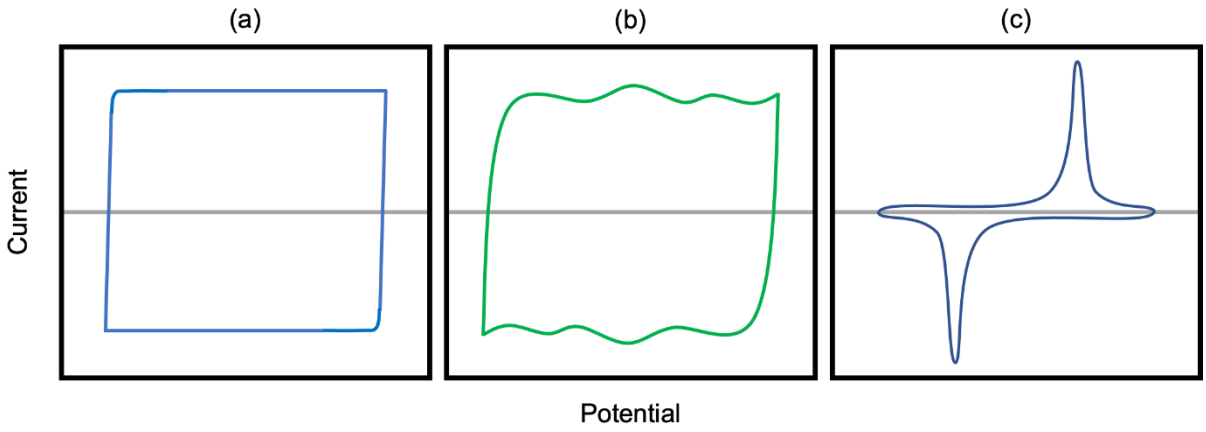

Figure 2.5: Examples of three-electrodes cyclic voltammetry curves related with different charge storage mechanisms. (a) Electrochemical double-layer capacitance. (b) Material with a pseudocapacitance. (c) Battery-like material with redox related peaks.

In other words, the charges stored in a pseudocapacitive material depend on the voltage difference between the electrodes as in common EDLCs, while battery-like materials store charge independently from the voltage difference, but at a precise potential [26]. This difference translates in a mathematical way as described by equations 2.10, which show the dependence of the current from the voltage rate ($\nu = \Delta V/\Delta t$) of battery-like reactions and of pseudocapacitive effects. As for the electrostatic current, the pseudocapacitive current directly depends on the voltage rate, depicted in equation 2.10 (a). On the contrary, the faradaic current as a function of the voltage rate is outlined in the equation 2.10 (b), which is derived from the Nernst equation. The *k* parameter depends on the system in exam including the electrolyte, the electrode and the way they interact [27].

(a) $$I_{pseudo} = C_{pseudo}\nu$$

(b) $$I_{redox} = k\sqrt{\nu}$$

Eq. 2.10

2.6. Electrode materials

Since the capacitance, following equation 1.2 of the previous chapter, is directly proportional to the electrode surface area accessible to the ions solvated in the electrolyte, an ideal electrode material should have the greatest possible ratio between the surface area and its weight. Moreover, the whole electrode surface area must be accessible by the ions with their solvation sphere; therefore, the material should have a porosity resulting in a mix of micro-pores, under 2 nm of diameter, and meso-pores, between 2 to 50 nm. Micro-pores are likely to match the dimension of solvated ions, whose size is usually under the nanometer [28,29]. On the contrary, meso-pores are needed for an efficient and fast propagation of solvated ions through the electrode material.

2.6.1. Activated carbons

The most used materials for SC electrodes are activated carbons, which are porous, high specific surface area and conductive carbon matrices. Usually, they are obtained through the pyrolysis of organic precursors. Removing organic molecules, only carbon atoms and non-volatile elements remain in a highly disordered structure with high specific surface area and a wide pore distribution, which depends mostly on the precursor. In order to obtain a more controlled pore distribution, this process is often followed by a chemical or a physical activation, which, fracturing the carbon matrix, produces a quasi-controlled pore size distribution. The role of the porosity is to create available pathways and sites for the diffusion and for storing electrolyte solvated ions. Mainly, the porous size should match the dimension of the ion solvation sphere (commonly below 2 nm diameter), but a minority part should be mesopores (between 2 nm to 50 nm), thus facilitating their diffusion in the carbon matrix [30].

2.6.2. Graphene

Besides activated carbons, graphene has a high potential as a SC electrode. Graphene, ideally, is a single layer of carbon atoms forming a honeycomb lattice, where every carbon is sp^2 hybridized (figure 2.6.1).

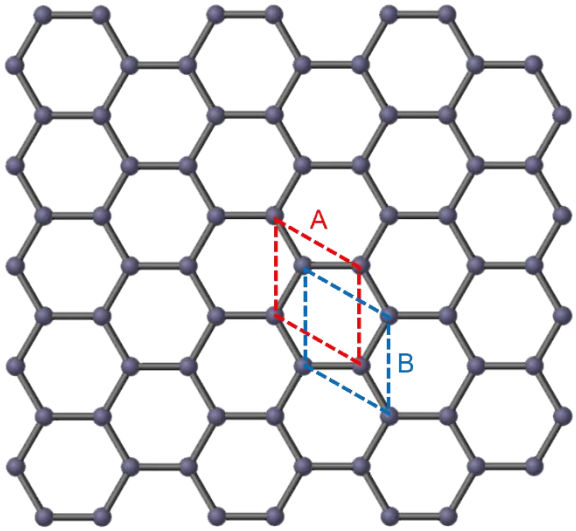

Figure 2.6.1: Theoretical graphene lattice. A and B sublattices are highlighted in red and blue, respectively.

The honeycomb structure, which is divided into two sublattices (A and B in figure 2.6.1) for symmetry reasons, is responsible of unusual electronic properties. In fact, ideal graphene behaves as a gap-less semiconductor where the charge carriers exhibit a linear dispersion relation, moving as they were massless relativistic particles. This is due to the overlapping of the band structures of the two sublattices A and B, which results in the conical energy spectrum at the Dirac points near the edges of the Brillouin zone [31], as shown in Figure 2.6.2. Therefore, thanks to the 2D structure and conjugated π bonds, graphene owes superior properties, such as high conductivity (2000 S/cm) and a theoretical specific surface area of 2630 m^2/g. Such properties give to graphene an extraordinary potential for the application in SC electrodes [32].

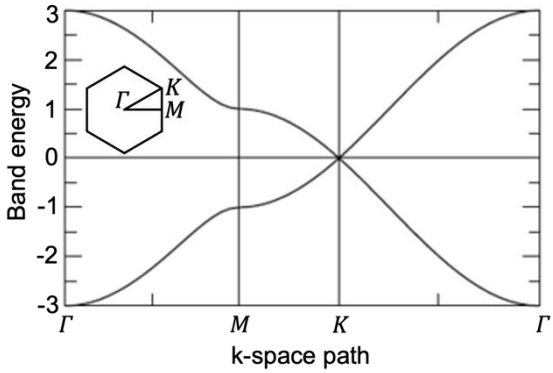

Figure 2.6.2: Band structure of graphene.

A nearly-ideal graphene can be obtained only through very expensive synthesis routes, such as chemical vapor deposition or mechanical exfoliation, which are unaffordable for mass production. However, there are many synthesis routes able to obtain a less-ideal cost-effective graphene-based material. These techniques, such as chemi-physical reduction and exfoliation of graphene/graphite oxide (figure 2.6.3), or laser conversion of polymers, described deeply in chapter 4, are able to produce a massive amount of few-layer graphene.

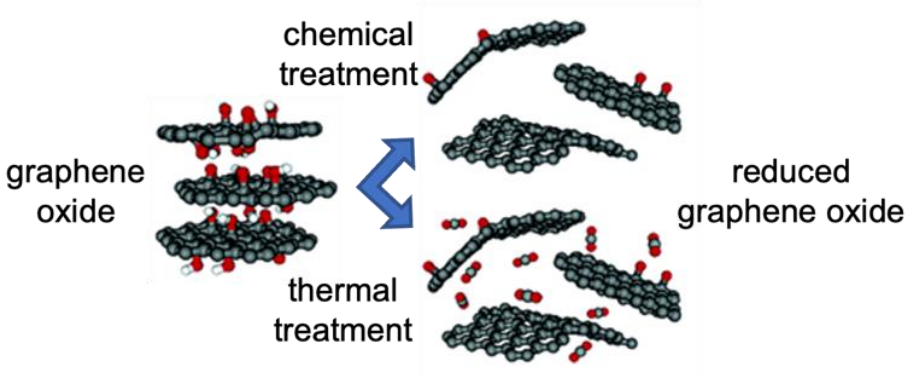

Figure 2.6.3: schematic synthesis of reduced graphene.

Few-layers graphene consists in a distribution of carbon single-layers and multilayers, commonly with a turbostratic arrangement, i.e. with a disorder in the layer stacking structure [33–37]. Few-layer graphenes usually have a high defect density, spacing from point defects, such as vacances or non-ideal aromatic rings, to edge defects and extrinsic impurities [38]. The defective and disordered structure grants a high specific surface area with many pathways for ions diffusion, i.e. a porous structure. Moreover, the presence of defects, such as dangling bonds, or distortion of the electronic structure, generates sites available for the decoration with hetero-atoms, such as oxygen and nitrogen, or with metal nanoparticles [39–43].

2.6.3. Hybrid materials

To enhance the specific energy stored in a SC, electrodes made of hybrid materials can be engineered, taking advantage of both faradaic and capacitive storing mechanisms. Therefore, they are obtained combining purely capacitive and redox-active materials in the same electrode. The first one provides electronic conductive paths to the redox sources, high surface area exposed to the electrolyte and available for electrochemical reactions, cushion of mechanical compression and heat conductive paths. All these aspects contribute to enhance the reaction kinetic and to improve the faradaic process efficiency [44]. Regarding the redox source material, two categories can be chosen. The first one is represented by pseudocapacitive materials, which display capacitive-like redox reaction, typically observed in peculiar metal oxides, such as MnO or RuO_2 [45]. The second one is represented by battery-like materials, such as $Ni(OH)_2$ and TiO_2, which exploit the high energy density Nernstian diffusion-controlled processes. The use of a highly defective and porous graphene as a carbon matrix enables to anchor and grow metal oxide nanoparticles of small size, typically around 10 nm [41,43,46], maximizing the surface area of the redox source exposed to the electrolyte and, therefore, the kinetics of faradaic reactions.

$Ni(OH)_2$ redox active material

Nickel (Ni) has long attracted the attention of the scientific community due to its chemical and physical properties, which make it a promising material for electrochemical applications. These properties include a remarkable chemical stability in alkaline media, a valuable reversibility in repetitive potential cycles, good catalytic activity. Therefore, Ni-based electrodes have been used in a wide range of electrochemical applications, such as batteries (e.g., nickel-cadmium, nickel-metal hydride, nickel-hydrogen), alkaline fuel cells, and alkaline water electrolysers. Recent advances in materials synthesis and characterization have led to an even greater variety of Ni-based hybrid micro-, meso-, and nano-materials proposed firstly as electrocatalysts [47]. The preparation of nanostructured Ni materials, such as flower-like or nano-rods [48,49], leads to improved surface area values. Such exceptional electrochemical properties and the improvement in high surface area led to Ni-based compounds application

also in hybrid SCs [46,50–53]. In fact, in alkaline aqueous media $Ni(OH)_2$ presents the reversible redox reaction described in eq. 2.11.

$$Ni(OH)_2 - e^- + OH^- \underset{reduction}{\overset{oxidation}{\rightleftarrows}} NiOOH + H_2O \qquad \text{Eq. 2.11}$$

However, the poor conductivity of $Ni(OH)_2$ [54] requires a conductive scaffold for an efficient electrochemical activity, such as porous graphene.

TiO_2 redox active material

Titanium dioxide (TiO_2), also called titania, is a wide band-gap semiconductor metal oxide. It has three main polymorphs: anatase, rutile and brookite. TiO_2 has been widely investigated for many applications thanks to its chemical stability, low cost, eco-compatibility and high abundance. Some of its main application fields are photocatalysis of organic pollutants, photovoltaic cells, sensors and energy storage [54–56].

Specifically, anatase is a meta-stable phase and converts into rutile at temperature exceeding 600 °C. On the other hand, rutile is the most thermodynamically stable phase. On the contrary, brookite is a meta-stable phase as well as anatase.

The titania many applications led to develop a wide range of synthesis routes, obtaining particles from the nano- to the micro-meter scale. For instance, the sol-gel and the solvothermal synthesis enable to synthesize nanoparticles under 20 nm diameter through the hydrolysis of titanium alkoxide in aqueous media [57].

From an electrochemical point of view, titania represents a valuable material both for batteries and SCs. In fact, titania can act as an anode material in batteries, intercalating lithium in a highly reversible way [58]. On the other hand, in aqueous-based SCs, titania can perform as a fast redox reaction source, reacting superficially with cations as described by equations 2.12 [59,60].

$$(TiO_2)_{surface} + H_3O^+ + e^+ \underset{reduction}{\overset{oxidation}{\rightleftarrows}} (TiO_2^- H_3O^+)_{surface} \qquad \text{Eq. 2.12}$$

Specifically, titania polymorphs present a different electrochemical activity, with anatase granting large capacitance, while rutile high reversibility [59,61].
Similarly to $Ni(OH)_2$, TiO_2 is poorly conductive, thus, it strongly benefits from a supporting conductive matrix to work, such as porous graphene or activated carbons [62].

2.7. Electrolytes

The electrolyte is one of the most important parts of an electrochemical energy storage device since, in combination with the electrodes, it defines the operating voltage, the speed of charge and discharge and the device time life. In particular, the SC stored energy depends on the working voltage window of the device relying mostly on the electrochemical stability of the electrolyte used. The second most important electrolyte parameter is the ionic conductivity, since it is affecting the power achievable from the SC, therefore the charging and discharging rate. The electrolytes can be divided into three categories: aqueous, organic, or ionic liquids. Aqueous electrolytes own the highest ionic conductivity (10^2 mS/cm magnitude order), but their electrochemical stability window is limited to that of the water, therefore it is around 1 V. Meanwhile, organic electrolytes assure a wider operating voltage, falling between 2.5 V and 3 V, but they display an ion conductivity which is 1 to 2 magnitude order lower than the aqueous electrolytes. Ionic liquids, relying on room temperature liquid salts, which are very viscous, have the lowest ionic conductivity, but the widest stability voltage window, reaching up to 4 V. Organic electrolytes and ionic liquids are beneficial because of the wider electrochemical stability voltage window, but their weak points are represented by high costs and safety problems, since they are air sensitive and flammable in a device short circuit scenario. On the other hand, aqueous electrolytes are safer, easier to handle, cheaper and more environment friendly, but the available voltage window is narrow and, therefore, the stored energy is low. The table 2.1 summarizes the main characteristics of common electrolytes based on each typology. Some of them, such as aqueous KOH and organic $LiClO_4$ in ethylene carbonate and dimethyl carbonate (EC:DMC), are used in this thesis.

Table 2.1. Conductivity and operating voltages of common electrolytes.

Electrolyte solution	***Concentration (mol/l)***	***Conductivity (mS cm^{-1})***	***ΔV (V)***
Aqueous, KOH	3.5	540 [63]	1
Aqueous, Na_2SO_4	2	125 [64]	1
Aqueous, H_2SO_4	1	800 [28]	1
Organic, $LiClO_4$/EC:DMC	1	~ 20	2.5 – 3
Organic, $TEABF_4$/ACN	1	59.9 [28]	2.5 – 3
Ionic Liquid, $[EMIM]^+[BF_4]^-$	-	14 [28]	4

SC performances, such as the energy and the power, depends also on the compatibility between the electrodes and the electrolyte, i.e. the size of the pores and the dimension of solvated ions. Mesopores are needed for maximizing the ions diffusion speed in the electrodes, already limited by the ionic conductivity of the electrolyte. Micropores are needed for increasing the electrodes active surface and, therefore, its specific capacitance and specific energy. Usually, positive and negative ions have different sizes, hence the porosity matching with the ions sizes should be done independently for both the positive and the negative electrodes. In particular, the ions solvation sphere depends on the solvent used. For instance, organic electrolytes, being their solvents composed typically by larger molecules than water, have usually wider solvation spheres than an aqueous medium. A brief overview of ions size and of their solvation spheres in different solvents are outlined in the following table.

Table 2.2. Ion size with and without the solvation sphere in aqueous and in organic electrolytes [28,29].

Ion	***Bare size (Å)***	***Hydration sphere (Å)***	***Organic solvation sphere (Å)***
K^+	1.33	3.31	-
OH^-	1.76	3.00	-
Li^+	0.60	3.82	~ 4
ClO_4^-	2.92	3.38	~ 5
H^+	1.15	2.80	-
SO_4^{2-}	2.90	3.79	-

Beside the compatibility between ions and pores sizes, two electrodes with a fixed surface area store less wider ions than smaller ones, therefore, directly influencing the capacitance. Hence, smaller ions should be desirable in order to maximize the energy density.

The electrochemical stability voltage window depends on the peculiar electrolyte-electrode system. The voltage window maximum value is fixed by the employed solvents, following the Table 2.1, but it is eventually tight if the electrode facilitates the solvent decomposition. For example, in aqueous alkaline electrolytes, the presence of nickel hydroxide promotes the irreversible hydrogen reduction, which, occurring at 0.55 V – 0.6 V with respect Ag/AgCl reference electrode, shrinks the electrochemical stability window. On the contrary, in the same electrolyte, a purely capacitive carbon material is stable up to 0.8-0.9 V.

2.8. Designs

Designing a SC consists in the engineering of the electrode-electrolyte-electrode system, in order to tune the properties to achieve the best possible performance, for example increasing the specific energy, while maintaining a good specific power.

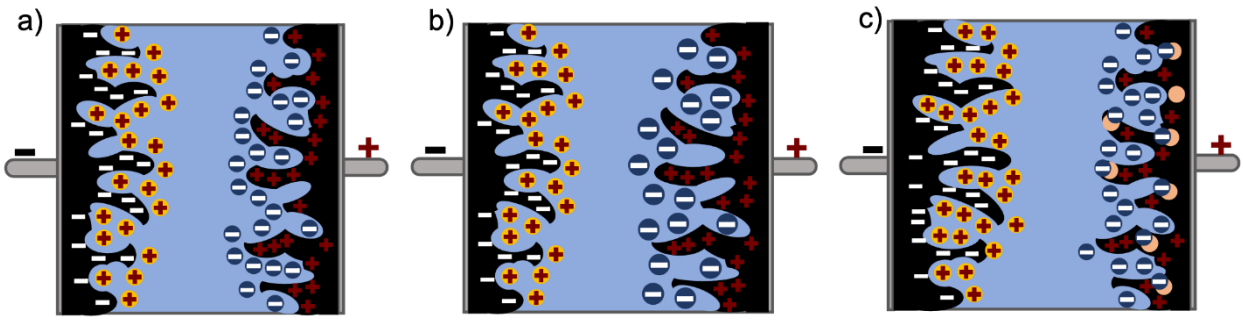

Figure 2.8.1: Supercapacitor and hybrid supercapacitors designs. a) symmetric supercapacitor design: both electrodes have the same mass and are made by the same material; b) asymmetric purely capacitive supercapacitor design: the electrodes are made with different carbon materials and/or with different mass amounts; c) design of hybrid asymmetric supercapacitor: one electrode is purely capacitive while the other is a hybrid material, i.e. with a predominantly pseudocapacitive or battery-like behavior.

The basic design is the symmetric one, hence with the same electrode as a positive and as a negative (fig. 2.8.1 a). Another possible design is the asymmetric one, which consists of coupling two different electrodes. The asymmetric design can be further divided into two categories. Firstly, there are asymmetric SCs which relies on the use of two capacitive

electrodes, e.g. an activated carbon coupled with a graphene-based electrode (fig. 2.8.1 b), or a capacitive electrode coupled with a pseudocapacitive one (fig. 2.8.1 c). Secondly, there are hybrid SC, recently named supercapatteries, which are based on a capacitive electrode coupled with a battery-like one, therefore, placing itself halfway between the behavior of a battery and that of a SC (fig. 2.8.1 c).

2.8.1. Symmetric supercapacitors

A symmetric SC is composed by two identical electrodes soaked by the electrolyte. Thus, the electrodes are made of the same material with the same mass, porosity, composition, and surface area, as shown in figure 2.8.1a. The symmetric design is valuable when negative and positive electrolyte solvated ions have approximately an equal size, which translates in the same specific capacitance for both electrodes, thus maximizing the total capacitance, following equation 2.4. In this configuration, the operating voltage window of the device matches with the electrolyte-electrode electrochemical stability window. The total specific capacitance of the SC, being composed by two series double-layer capacitances, is equal to a quarter of the electrode specific capacitance, following equation 2.11, where $C_{\pm}$ and $m_{\pm}$ are respectively the electrodes capacitances and the masses.

$$C_s = \frac{C}{M_{tot}} = \frac{{C_{\pm}}^2}{2C_{\pm}} \frac{1}{2m_{\pm}} = \frac{C_{S\pm}}{4} \qquad \textit{Eq. 2.11}$$

2.8.2. Asymmetric design

An asymmetric configuration differs from a symmetric one since it is composed by two different electrodes. They can differ in terms of material and/or in terms of mass amount. Their electrodes are made of carbon-based and/or of hybrid materials, i.e. materials which

show redox reactions, due to a pseudocapacitance, or to a battery-like capacity. In particular, the asymmetric SC design, i.e. with purely capacitive electrodes, is valuable when the solvated anions and cations have different sizes and two electrode of different materials, or with different mass amount, are needed for matching their porosity with the solvated ions and achieving an equal electrodes capacitance. In the example of figure 2.8.1 b), the electrode porosity fits better with cations and, since the capacitance depends on the number of charges stored in pores, i.e. on the reachable surface, the negative electrode has a higher specific capacitance than the positive one, defined as C_s^- and C_s^+, respectively. In order to have the same capacitance, it is mandatory to balance the electrodes masses (m_+, m_-) following equation 2.12.

$$m^+{C_s}^+ = m^-{C_s}^- \qquad \textit{Eq. 2.12}$$

Equation 2.14 describes the masses balance in the case of an equal electrochemical stability voltage window and enables to use the maximum capacitance and voltage window available. If the electrochemical stability voltage window of the electrodes materials is not equal, which typically happens when hybrid materials are used, it must be used equation 2.13, which is precisely the charge balancing equation and reduces to equation 2.12 in the case of an equal stability potential difference *ΔV*.

$$Q^- = Q^+ \rightarrow m^+ \Delta V^+ C_s^+ = m^- \Delta V^- C_s^- \qquad \textit{Eq. 2.13}$$

In order to enhance the specific energy of a SC, a redox source can be introduced in a carbon-based electrode, giving rise to a pseudocapacitance or to a battery-like capacity. In both cases, the electrode ability to store charge increases with beneficials for the specific energy. Coupling the hybrid material with a capacitive one in the asymmetric configuration enables to increase the stored energy, lowering the side effects coming from the use of a battery-like material. Moreover, since usually the negative and the positive electrodes have different electrochemical stability windows, the total voltage difference available results extended as a combination of the two, and it is maximized when the stored charges are balanced following equation 2.13. Such asymmetric device is commonly named hybrid SC and, recently, is divided into asymmetric pseudocapacitor and supercapattery, as the redox source is pseudocapacitive or battery-like, respectively. Specifically, the hybrid SC which relies on lithium-based organic electrolytes and on a battery-like electrode is named Li-Ion Capacitor (LIC).

3. EXPERIMENTAL TECHNIQUES

This chapter will be dedicated to present the experimental techniques employed in this thesis. Electrochemical, chemi-physical and combined techniques will be discussed. Specifically, two and three electrodes cyclic voltammetry, galvanostatic charge-discharge cycles, electrochemical impedance spectroscopy, Raman spectroscopy, scanning and transmission electron microscopy, powder X-ray diffraction and Raman spectroscopy combined with three electrode cyclic voltammetry are presented.

3.1. Cyclic voltammetry

Cyclic voltammetry (CV) is a powerful technique able to deeply characterize the electrochemical behavior of an electrochemical cell. It consists in the application of a controlled potential sweep to an electrode in an electrochemical cell and the measurement of the current as a function of the potential. The three-electrodes configuration allows to investigate the electrode-electrolyte system, characterizing the electrochemical behavior of the electrode material and it is a preliminary measurement useful to build the final device. It enables to investigate the possible presence of electrochemical reactions, their nature, their reversibility, the system stability, the kinetics and the electrode capacitance. It consists of three different electrodes, the working electrode (WE), the counter electrode (CE) and the reference electrode (RE) immersed in the electrolyte as shown in figure 3.1.1. The WE coincides with the electrode material under investigation, the CE, usually platinum, is an electrode which, ideally not participating in any reaction, is not monitored during the experiment. Besides the WE, the RE is the most important and delicate part of the cell. It consists in the probe through the potential of the WE is investigated and referred. The second design, i.e. the two-electrode cell, is usually used for the final device testing performances and it is made out of two electrodes divided by a separator soaked into the electrolyte. Specifically, it enables to characterize the full electrode-electrolyte-electrode system, investigating its stability voltage window, the electrochemical behavior, and kinetics. In this case the RE is

missing and the current flowing across the entire cell is evaluated with respect to the applied voltage difference.

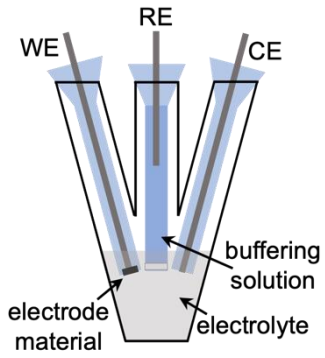

Figure 3.1.1. Three-electrode cell typical setup. It is composed by working electrode (WE), by the reference electrode (RE) and by the counter electrode (CE) immersed into the electrolyte. The RE is not directly in contact with the electrolyte but is buffered with a solution separated from the electrolyte by a frit.

The RE is a material which has a stable potential and, usually, is composed by a highly reversible redox couple immersed in a buffering, separated from the electrolyte by a frit. During the experiment, the RE maintains stable its potential being in electrochemical equilibrium with its buffering solution and not participating actively to the experiment. RE potentials are referred to the potential of the standard hydrogen electrode, based on the hydrogen reduction reaction. Other common REs are the couple Ag/AgCl, namely a silver wire covered by a silver chloride film immersed in a KCl saturated aqueous solution, or the couple Li/Li+, namely a metallic Li wire immersed in lithium-based organic electrolytes.

The curves collected through CV, named voltammograms, can be ideally of three typologies, i.e. rectangular, pseudo-rectangular or with current peaks, as described in the 2nd chapter and recalled in the following figure. In practical terms, the experimental curves might deviate from the ideality since the resistances are not ideal, showing not rectangular and/or symmetric shapes with respect to the zero current value. Furthermore, being the electrodes complex systems, the curve can result as a combination of different behaviors, showing both capacitive and faradaic effects.

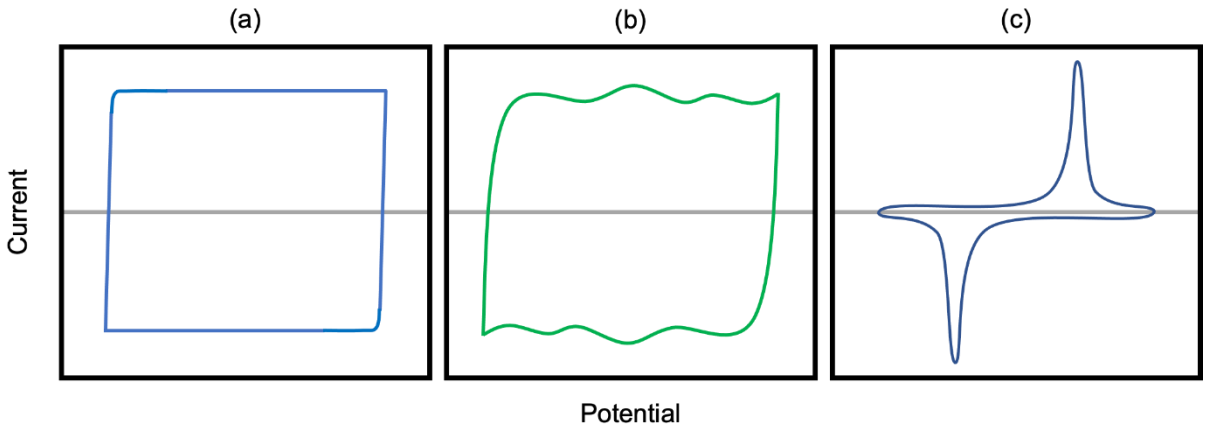

Figure 3.1.2: Examples of three-electrodes cyclic voltammetry curves related with different charge storage mechanisms. (a) Electrochemical double-layer capacitance. (b) Material with a pseudocapacitance. (c) Battery-like material with redox related peaks.

As a first information, with a single rate measurement, it is possible to determine the stability voltage window of the electrode material coupled with the electrolyte. The voltage window is tightened by the decomposition of the electrolyte which must be avoided, as it irreparably prejudices the reversibility of the system. Since the current of such decomposition reactions increases exponentially as a function of the voltage applied [65], it is possible to recognize in the CV at which potential the electrolyte decomposition starts and, therefore, which is the maximum voltage difference reachable with the electrode-electrolyte analyzed system. As an example, two CV curves are represented in figure 3.1.3 showing the irreversible decomposition of the electrolyte.

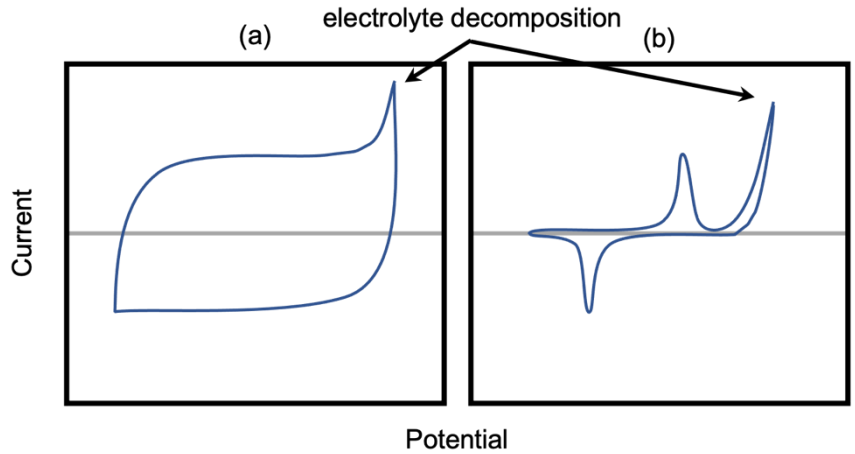

Figure 3.1.3: Examples of the electrochemical stability voltage window evaluation. a) cyclic voltammogram of capacitive material; b) cyclic voltammogram of a battery-like material. The hypothetic material is stable until the potential of the electrolyte decomposition marked by an exponential increase behaving of the current.

Once that the stability voltage window is determined, it is possible, independently from the presence of redox contributes and if the active material mass is known, to evaluate its specific capacitance from the CV curve through equation 3.1.1.

$$C_S = \frac{1}{m}\frac{\oint I dV}{2\upsilon \Delta V} \qquad \textit{Eq. 3.1.1}$$

Precisely, the stored charge is proportional to the half of the area enclosed into the curve, thus, the specific capacitance is calculated as the integration of the current *I* over the voltage *V*, divided by 2, by the voltage rate ν, by the material mass and by the voltage window investigated.

CV allows also to investigate the charge storage kinetics, through successive measurements performed at different voltage rates. First of all, it enables to establish the capacitance dependency on the voltage rate, which is strictly related with the ions storage mechanisms and with their diffusion into the electrolyte-electrode system. For an ideal capacitor with high ionic conductive electrolyte, the capacitance should not depend on the voltage rate. However, the presence of diffusion-controlled processes, namely redox reactions, determines a non-linear dependence of the current from the voltage rate and then, a variation of the capacitance with the increasing of the voltage scan rate [27].

Subsequently, through a method firstly applied from Trasatti [66,67], it is possible to differentiate the capacitive contribution from the diffusion controlled one, i.e. related to redox reactions. It relies on the equations 12 and 13, shown in the second chapter of this thesis and combined in equation 3.1.2, which state the voltage scan rate-current relation for different typologies of charge storage mechanisms.

$$I_T = I_{c-pseudo} + I_{redox} = a\,\upsilon + b\,\upsilon^{1/2} \qquad \textit{Eq. 3.1.2}$$

Thus, replacing *I* in equation 3.1.1 with equation 3.1.2, the capacitance can be rewritten as a linear function of $\nu^{-1/2}$, where the constant represents the capacitance contribution rising from capacitive behaving processes and the $\nu^{-1/2}$ coefficient derives from battery-like reactions.

$$C = \frac{1}{m}\frac{\oint \left(a\,\upsilon + b\,\upsilon^{1/2}\right) dV}{2\upsilon\Delta V} = \frac{1}{m}\frac{\oint a dV}{2\Delta V} + \frac{1}{m}\frac{\oint b dV}{2\Delta V}\upsilon^{-1/2} = C_{c-pseudo} + \beta\,\upsilon^{-1/2} \qquad \textit{Eq. 3.1.3}$$

Moreover, equation 3.1.3, expressed as the inverse of the capacitance as a function of the scan rate square root, results in the evaluation of the electrode theoretical maximum capacitance, as described by equation 3.1.4 when ν goes to zero [67].

$$\frac{1}{C} = \frac{1}{C_T} + \gamma\, \upsilon^{1/2} \qquad \textit{Eq. 3.1.4}$$

Equations 3.1.3 and 3.1.4 translate graphically in figure 3.1.4 a) and b), where the capacitance is plotted as a function of $\nu^{-1/2}$ *and* $\nu^{1/2}$, respectively. The intercept of the linear regression with the capacitance axes coincides with $C_{c\text{-}pseudo}$ and with C_T. In the case of Figure 3.1.4 a), the line slope represents the redox reactions weight.

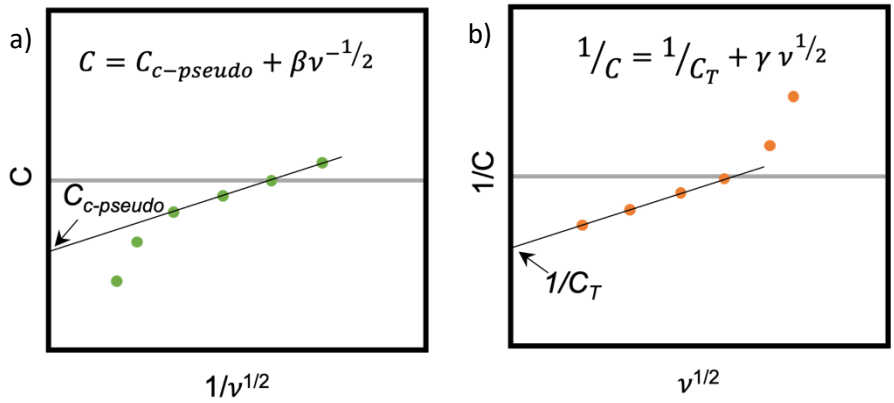

Figure 3.1.4: Linear regression example of the capacitance (a) and of the inverse of the capacitance (b) (vertical axis) as a function of the voltage scan rate (horizontal axis) following equation 3.1.3 and 3.1.4, respectively. The intercepts with the C and with the 1/C axes correspond, respectively, to the surface storage mechanisms related capacitance, and to the inverse of the total capacitance.

A single CV curve is not enough for the analysis early described. However, a multiple voltage scan rate experiment, which consists in the acquisition of cyclic voltammograms with several different scan rates, enables to disentangle the contributions. In a real experiment, since the system intrinsic resistance is causing an ohmic drop that affects the diffusion kinetics, the capacitance behavior is non-linear as a function of the scan rate square root ($\nu^{1/2}$) for very high ν values [67].

Furthermore, Dunn developed another method [67,68], schematically described in figure 1.3.5, which, relying still on the different kinetics of surface-related and of bulk diffusion-controlled charge storage mechanisms, allows to carefully separate, quantitatively and graphically, the two contributions. This method, instead of the capacitance evaluation for each

rate, relies on the coefficients assessment, i.e. *a* and *b* of equation 3.1.2, for several fixed values of the voltage, scanning all the potential window investigated. Operatively, fixed the voltage value, the current is evaluated for each voltage scan rate, as shown in figure 3.1.5 a). The coefficients are extrapolated through a linear regression fit of $I/\nu^{1/2}$ as a function of $\nu^{1/2}$ (figure 3.1.5 b). The coefficients extrapolation, carried out at least for 100 voltage values and for both the oxidation and the reduction curve, allows to separate each cyclic voltammogram curve into two parts, associated to the surface-related (filled curve in figure 1.3.5 c) and to the diffusion-controlled charge storage mechanisms.

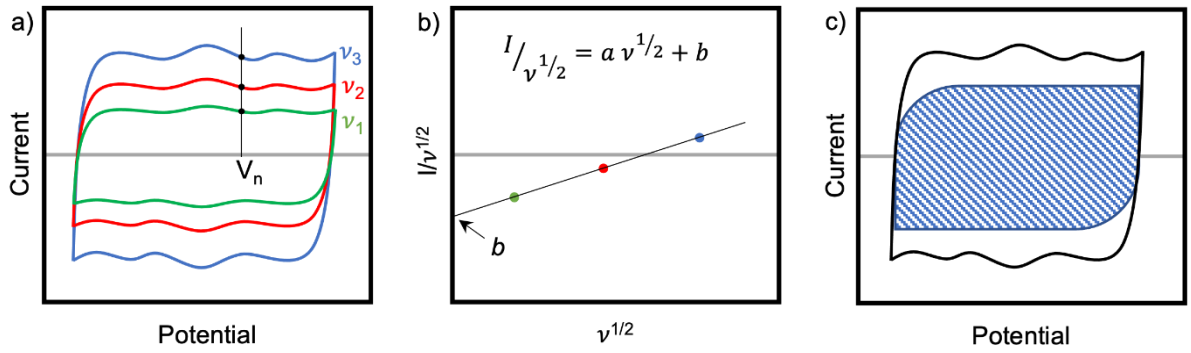

Figure 3.1.5: Dunn method scheme for the visual separation of the capacitive contribution from the diffusion controlled one. a) fixed the voltage value V_n, the current is evaluated for each scan rate. This evaluation must be carried out for as much as possible number of voltage values; b) the linear regression of the current values as a function of the voltage scan rate must be performed for each voltage selected. Inset: equation to be used for the fit; c) visual separation of the contributions, the curve filled with the blue lines corresponds to the surface-related mechanisms.

Both the Trasatti and the Dunn methods are very useful for evaluating the weight and the presence of different charge storage mechanisms. However, the results might be evaluated carefully and compared with those of other techniques in order to deeply understand the physics and electrochemistry of the analyzed system [69,70].

As far as the CV setup is concerned, a swagelok-type cell is used, which is shown in figure 3.1.6. It consists of a three-arms PTFE cell, each one used for a different electrode. The horizontal arms are used for the CE and the WE, which are divided by a separator, soaked with the cell electrolyte. The RE is inserted in the vertical arm and is separated from the cell electrolyte by a porous frit. For aqueous electrolytes, a platinum disk is used as a CE and, Ag/AgCl immersed in KCl 3.5M aqueous solution is used as a RE. For organic lithium-based electrolytes, metallic lithium is used as both the CE and the RE.

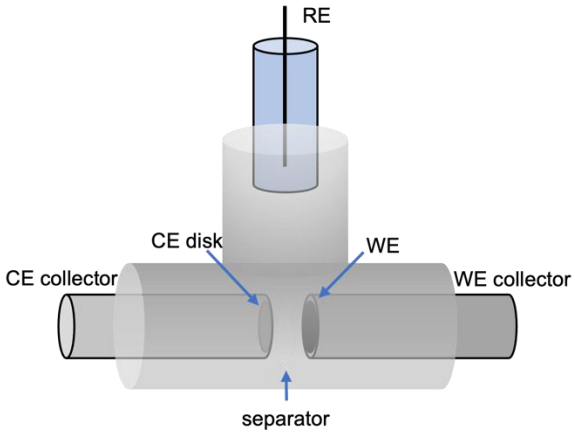

Figure 3.1.6. Three-electrodes Swagelok setup.

The two-electrodes cyclic voltammetry, instead, can be performed on final devices, in our case stainless steel coin cells (standard CR2032). The instruments used in this work were a Keithley Sourcemeter 2400C and a Gamry Interface 1010 potentiostat/galvanostat.

3.2. Galvanostatic charge-discharge technique

Galvanostatic charge-discharge technique is a valuable probe for the performance evaluation of charge storage final devices, such as SCs, batteries or hybrid systems, simulating the energy storage device real-life use. It consists in applying a constant current, while the voltage is measured as a function of the time. Since both the voltage and the time are accurately measured, it provides the exact values of capacitance/capacity, the specific energy for each current rate and the relative specific power, following equations 3.2.1 [71].

a) $$C_S = \frac{1}{m}\frac{I\,\Delta t}{(\Delta V - \Delta V_{drop})}$$

b) $$E_S = \frac{1}{2}\,C_S\,(\Delta V - \Delta V_{drop})^2$$ *Eq. 3.2.1*

c) $$P_S = \frac{1}{2}\,C_S\frac{(\Delta V - \Delta V_{drop})^2}{\Delta t}$$

Galvanostatic charge-discharge cycles of a SC and of a battery own peculiar signature and differ in the curves shape. As seen in the second chapter, a SC owns a triangular charge-discharge cycle, where the potential is directly proportional to the charge, and, therefore, to

the time being the current constant. On the contrary, applying a constant current, the battery potential is not directly proportional to the time and presents a charge/discharge plateau in correspondence of the potential where redox reactions occur. A hybrid system, with both capacitive-like effects and diffusion-controlled processes, which are mainly due to Nernstian redox reactions, has a charge-discharge cycle behavior in the middle of the formers, with a deviation from the triangular shape. The three behaviors are presented below in figure 3.2.1.

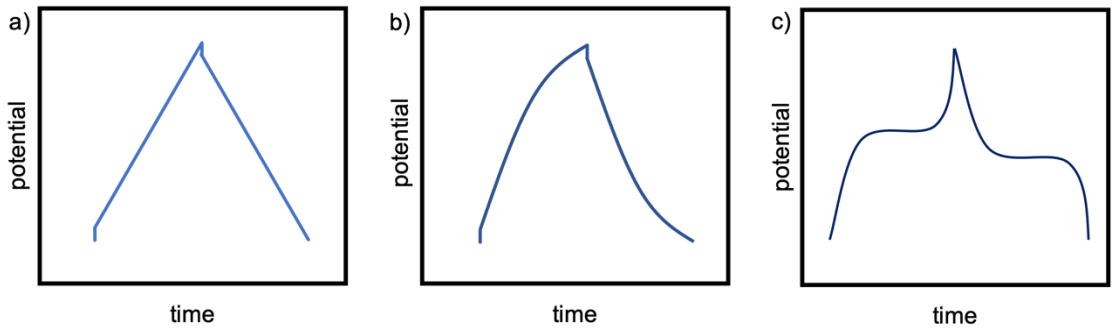

Figure 3.2.1: Galvanostatic charge-discharge cycles example behaviors of a supercapacitor (a), a hybrid system (b) and a battery (c).

Another factor responsible for the deviation from the triangular shape, as seen in the section 2.3 of the second chapter, is the possible presence of a leakage current, which can be evaluated through the collection of the cell voltage as a function of time with a zero current applied. Moreover, performing charge-discharge cycles, the coulombic efficiency $C_{\%}$ and the energy retention $E_{\%}$ carried out over thousands of cycles can be evaluated as described by equations 3.2.2.

a) $$C_{\%} = \frac{C}{C_0}$$

b) $$E_{\%} = \frac{E}{E_0}$$ *Eq. 3.2.2*

Another important parameter provided by galvanostatic charge-discharge cycles is the ESR, described in the 2nd chapter, which equals to the half of the voltage drop occurring at the beginning of each charge-discharge curve, divided by the current, following equation 3.2.3.

$$ESR = \frac{\Delta V_{drop}}{2I}$$ *Eq. 3.2.3*

Galvanostatic charge-discharge cycles are performed on final devices, thus using stainless steel coin cell (standard CR2032). The instruments used in this work are a Landt CT2001 A and a Neware CT-4008T Battery testing systems.

3.3. Electrochemical impedance spectroscopy

Electrochemical impedance spectroscopy (EIS) is a powerful technique able to characterize the electrochemical cell dynamics [72]. In particular, in SCs, it allows to accurately evaluate the final device equivalent series resistance. Operatively, the experiment is performed applying a sine wave voltage *V* as a function of the time and of the frequency $f=\omega/2\pi$, going from low (1 Hz) to very high (10^6 Hz) frequencies, and measuring the resultant current *I*, which is phased with respect *V* of θ. From the current response and the voltage applied, the impedance is evaluated and separated in its real and imaginary parts, following equations 3.3.1.

a) $V(t) = V_{max}\sin(\omega t)$ b) $I(t) = I_{max}\sin(\omega t + \vartheta)$

Eq. 3.3.1

c) $$Z(\omega) = \frac{V(\omega)}{I(\omega)} = Re(Z) + j\, Im(Z)$$

EIS experiment enables the evaluation of the ESR, which can be extrapolated from the Nyquist plot, that is one of the most used charts for representing EIS data. A porous carbon-based electrode, coupled with an electrolyte, can be schematized as a circuit through two vertical RC ladder networks in series with a RC parallel network as shown in figure 3.3.1. If a symmetric SC is analyzed, only one vertical RC ladder network must be considered. The vertical RC ladder network is necessary for describing a porous electrode with a wide distribution of pores, going from micro-pores to meso-pores. Since each pore has its own resistance and capacitance, a simple equivalent circuit, such as that shown in the second chapter, might be not able to describe the open circuit voltage decay and the behavior of carbon-based SCs, particularly at high frequencies [73]. The RC parallel network in series describe the electrolyte, for instance, *R* corresponds to the bulk solution resistance and *C* to its capacitance, i.e. the dielectric polarization.

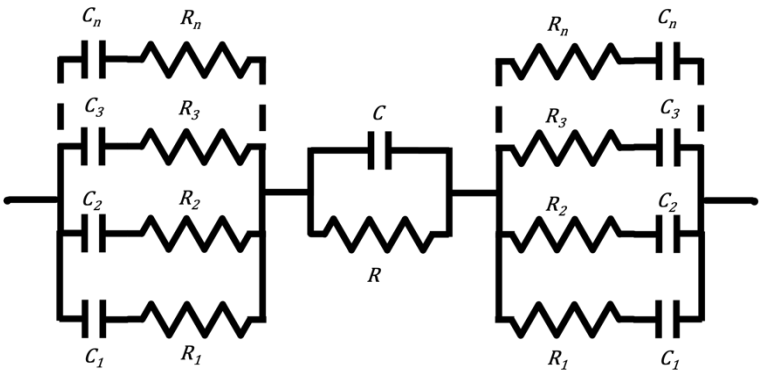

Figure 3.3.1: Equivalent circuit of an asymmetric carbon-based supercapacitor. The vertical ladders describe the porous carbon-based electrodes. The RC parallel network describe the electrolyte.

The RC parallel network in the center dominates the impedance response for low frequencies, on the contrary, the vertical RC ladder networks dominates at high frequencies, as described by equations 3.3.2.

a) $$Z_{RC} = \frac{R}{1+(\omega CR)^2} - j\frac{\omega CR^2}{1+(\omega CR)^2} \xrightarrow[\omega \to 0]{} R \equiv R_{electrolyte}$$

Eq. 3.3.2

b) $$Z_{RC\ ladder} = \left(\sum_{i=1}^{n} \frac{j\omega C_i}{j\omega C_i R_i + 1}\right)^{-1} \xrightarrow[\omega \to \infty]{} \frac{\prod_1^n R_i}{\sum_1^n R_i} \equiv ESR$$

The combination of these components gives, ideally, a response appearing in the Nyquist plot as that shown in figure 3.3.2. Thus, at very high frequencies, the SC equivalent series resistance (ESR), which ideally as shown in Figure 3.3.2 should be very small, is evaluable as the imaginary impedance goes to zero.

The semi-circle at middle frequencies, displayed in figure 3.3.2, is related to the parallel resistance *R*. In liquid electrolyte-based SC analysis, the semicircle emerges when charge-transfer processes occur at the interface electrode-electrolyte, generating, consequently, a resistance. In fact, the lower frequency intercept of the semicircle with the real impedance axis corresponds to such resistance, which might be related to faradaic processes or to charge leaks. Otherwise, the semicircle should not be present. The straight line at low frequencies is related to the finite ladder networks but, in that frequency range, it is approximate as an infinite ladder network or, operatively, as a constant phase element (CPE), which is described by equation 3.3.3.

$$Z_{CPE} = \frac{1}{a(j\omega)^b} \qquad \textit{Eq. 3.3.3}$$

A CPE consists in a capacitance in parallel with a resistance, thus with a leakage resistance, whose intensities are dependent upon the frequency (ω) and the a and b coefficients. Specifically, while the coefficient a can have any real number, b has a real value between 0 to 1. If it is equal to 1, the CPE is equivalent to an ideal capacitance with no leakage resistance. On the contrary, if it is equal to 0, the CPE corresponds to an ideal resistance. In all the other situations (b values), the CPE is behaving as a capacitance with a parallel resistance.
Going back to the Niquist plot, the angle between the straight line and the real impedance axis indicates that the ladder network capacitances are charging at different rates. At very long times, i.e. low frequencies, the line angle should reach 90° with respect to the horizontal axis, behaving as a single capacitance in series with the RC-parallel, equal to the maximum capacitance of the SC [73].
EIS experiments are performed on final devices, thus, using stainless steel coin cells (standard CR2032). The instruments used are a Gamry Interface 1010 potentiostat/galvanostat and a HP 4192A Impedance analyser.

3.4. Scanning and Transmission electron microscopy

The scanning (SEM) and the transmission (TEM) electron microscopy are techniques for characterizing the materials morphology, composition, and structure, relying on similar principles, both based on an electron beam scattered by a sample, but using different detection techniques, different energies and, therefore, investigating different length scale. While SEM is able to successfully characterize the micro-meter scale with high resolution, TEM allows to study the materials with high resolution at the nano-meter scale. The advantage of using electrons instead of visible light is that the shorter electrons wavelength interacts with the matter at the nano and micro scale, therefore giving better image resolution than optical microscopes. The electron beam, accelerated through a voltage difference, is focused on the

sample through a set of electromagnetic lenses. Then, many types of radiations scattered are collected and analyzed, providing a wide range of information, ranging from morphological to compositional and structural. A scheme of the two instruments is depicted below in figure 3.4.1.

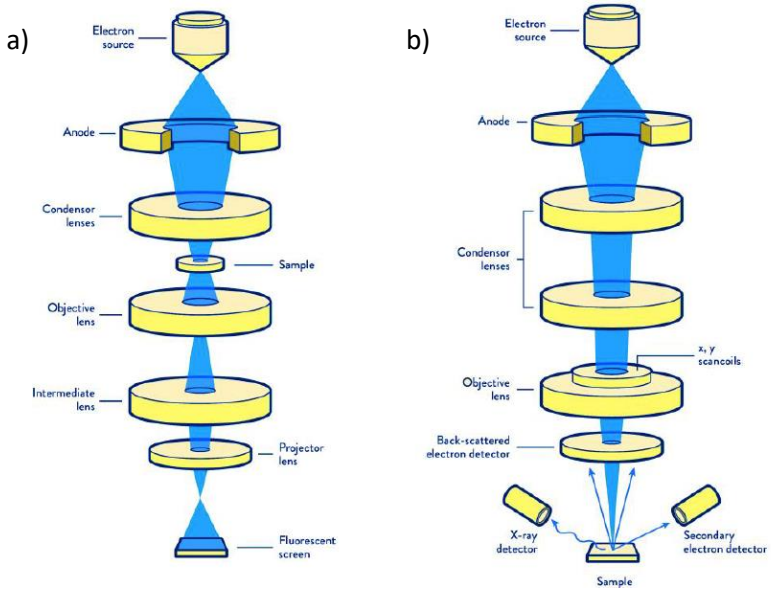

Figure 3.4.1: Schematic representation of the design, optics and detection system of TEM (a) and SEM (b). The light blue beam represents the electrons sourced by the electron gun and interacting with the sample.

In the case of SEM, the collected radiations are mainly secondary electrons and characteristics X-ray. The formers consist in the electrons extracted through the ionization of the sample atoms and provide information related to the morphology, allowing to produce a detailed image of the material from the micro to the nano-meter scale. The latters, produced by the electrons of the outer shells falling to inner shells, i.e. to core holes, provide information related to the atoms energy levels and, therefore, to the material composition enabling the chemical micro-analysis. SEM characterization involves the material surface, and in the case of a conductive sample, it does not need any particular preparation. Instead, TEM works mainly in transmission, collecting the radiation below the sample, which must be very thin; usually, a small amount of the material is deposited onto a conductive grid. Beyond the secondary electrons and the characteristic X-rays, TEM detects the elastically and inelastically scattered electrons which provide diffraction patterns and images with a very high resolution, up to the atomic scale. Moreover, TEM can operate even in scanning mode (STEM), thus rastering over the sample with a very focused electron beam. Thus, STEM is suitable for

analytical techniques, such as high-angle annular dark-field imaging (HAADF), energy dispersive X-ray spectroscopy (EDX) and electron energy loss spectroscopy (EELS).

3.5. Powder X-ray diffraction

Powder X-ray diffraction (PXRD) is a structural characterization technique for crystalline powders based on the elastic scattering of the X-rays with matter. Since X-ray photons have a wavelength comparable with atomic distances, they can interact elastically with the atomic lattice. Thus, a XRD experiment relies on the fact that, if a sample has spatially ordered atoms, as for crystals, scattered photons give interference patterns, related to the periodicity of atom positions, typical of crystalline materials.

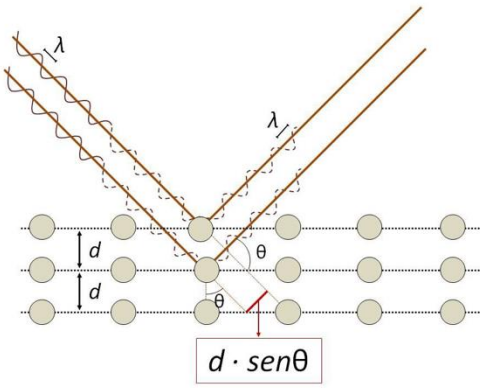

Figure 3.5.1: Bragg law scheme. Crystal lattice family planes reflect the radiation giving constructive interference when Bragg law is satisfied.

In particular, photons scatter coherently and elastically giving constructive interference and producing a well-defined pattern when they satisfy the Bragg law (equation 3.5.1).

$$n\lambda = 2d\ sin\vartheta \qquad \textit{Eq. 3.5.1}$$

Bragg's law considers crystalline planes (indexed by Miller indices h, k and l), placed at a distance of d_{hkl} from each other. Adjacent planes scatter photons at angles θ, giving constructive interference once that member on the right is an integer (n) multiple of the X-rays wavelength λ, which is about 1.54 Å for a laboratory X-ray Cu source. The resulting image, typically collected by a CCD detector, results as a series of arches, whose integrated intensities as a function of arches-center distance, translates into diffractograms peaks as a function of

the angle 2θ. Their position, intensity and shape are related to the crystal symmetry, to the atomic position in the unit cell and to the crystal size, respectively. In this thesis work the measurements were performed with a D8 Advance Bruker diffractometer (figure 3.5.2), in a Debye Scherrer geometry, equipped with a Cu anode, and a MARCCD MX225 2D detector. Powder samples were sealed in 0.5 mm diameter glass capillaries at room atmosphere conditions. Concerning the data analysis, Fit2D software is used for the image intensities integration, Crystal impact Match software for the crystal structure identification. The Rietveld refinements, through GSASII suite, is used for the structural model refinement and for the particle size evaluation.

Figure 3.5.2: D8 Advance Bruker diffractometer in a Debye-Scherrer geometry. On the left: 2D detector MARCCD.

3.6. Raman spectroscopy and spectro-electrochemistry

3.6.1. Raman spectroscopy

Raman spectroscopy is a powerful technique which, through a laser, is able to investigate the vibrational modes of a material. It relies on the use of a monocromatic radiation (laser) with

a visible wavelength, or in the near infrared, which is focused on the sample. Photons interact mainly elastically with the sample (Rayleight scattering), although, a minor number of photons scatter inelastically, exchanging energy with it. The quantized exchanged energy is strictly related with the vibrational modes of the material. More in detail, the electrons of the material, once excited by photons to a virtual energy state, can decay to a ground state different by the initial one, due to the creation or to the annihilation of a lattice phonon. Hence, the emitted photon will have an energy hν equal to the difference between the energy levels. Such scattering mechanisms are depicted in figure 3.6.1.

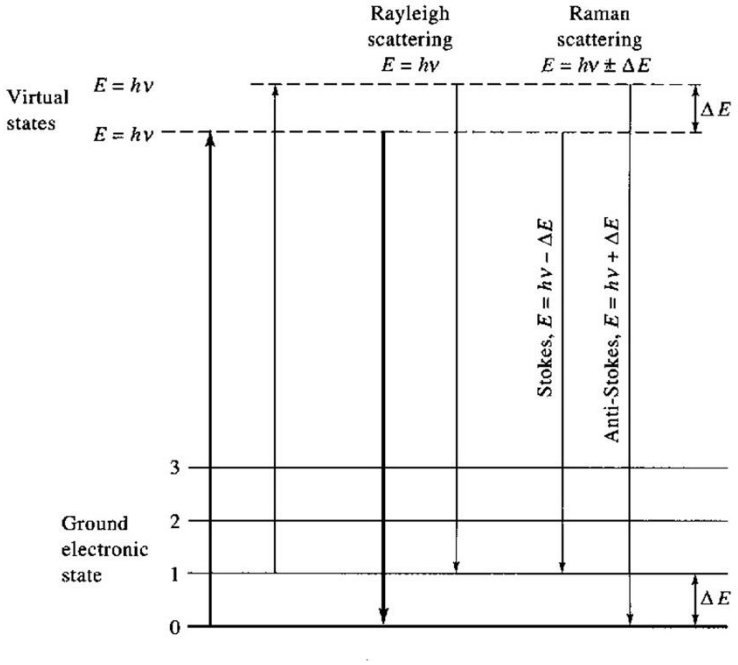

Figure 3.6.1: Scattering scheme for a laser source. Both Rayleigh scattering and Raman scattering are drawn.

The frequencies ν_{abs}, related to the energies absorbed by the sample, i.e. the $\nu_{abs}=(E_i-E_f)/h$, coincide with the bonding vibrational modes, which, as a consequence, are activated or deactivated. These vibrational modes enable to determine the vibrational spectrum which is peculiar of each material. Such inelastic scattering is named Raman scattering and the consequential modes are of Stokes or Anti-Stokes, corresponding to the activation and deactivation of phonon modes, respectively. Raman scattering data are plotted in a spectrum as the relative radiation intensity I/I_0, i.e. the number of absorbed photons normalized on its maximum, with respect to the Raman shift frequency, calculated with respect to the Rayleigh scattering frequency. An ideal spectrum of a Raman scattering is shown in figure 3.6.2. Since

the Raman Anti-Stokes intensity is usually lower than Raman Stokes one, it is worth to focus on the latter in an experiment.

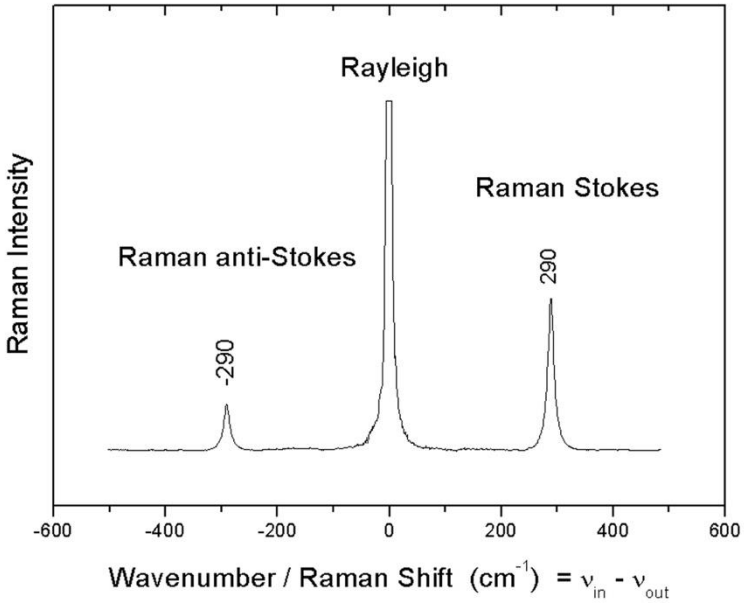

Figure 3.6.2: Ideal Raman scattering spectrum with a single Stokes and Anti-Stokes frequency couple is showed.

The instrument used for Raman spectroscopy is a Horiba Jobin Yvon LabRam (HORIBA Scientific, Kyoto, Japan) confocal micro-spectrometer (300 mm focal length), equipped with an Olympus BX40 microscope (Olympus, Tokyo, Japan), using a 50x ULWD objective, an 1800 groves/mm grating, a XY motorized stage and a Peltier cooled silicon CCD. The 473.1 nm line of a doubled Nd:YAG laser was used as excitation.

3.6.2. Raman spectro-electrochemistry

Raman spectro-electrochemistry consists in a combination of the Raman spectroscopy and electrochemical analytical techniques in operando state. For instance, in this thesis, Raman spectroscopy is performed during a three-electrodes CV experiment. The purpose of this analysis is to clarify the electrode material processes ongoing during the oxidation and reduction curves [74,75]. Such experiment takes advantage by the fact that glass and aqueous electrolyte are transparent to the visible radiation, thus, the laser photons are not absorbed or scattered until they reach the electrode surface, enabling the Raman spectroscopy during an electrochemical experiment [27]. The set-up used is shown in figure 3.6.3 and consists in a

three-electrodes cell with a horizontal glass window on the working electrode. The active material is made out of a slurry, or it is directly deposited on a Pt spot on the top of the WE glass tube, as displayed on the figure. Silver is used as a quasi-reference electrode (Q-RE) in direct contact with the electrolyte and a platinum wire is used as a counter electrode.

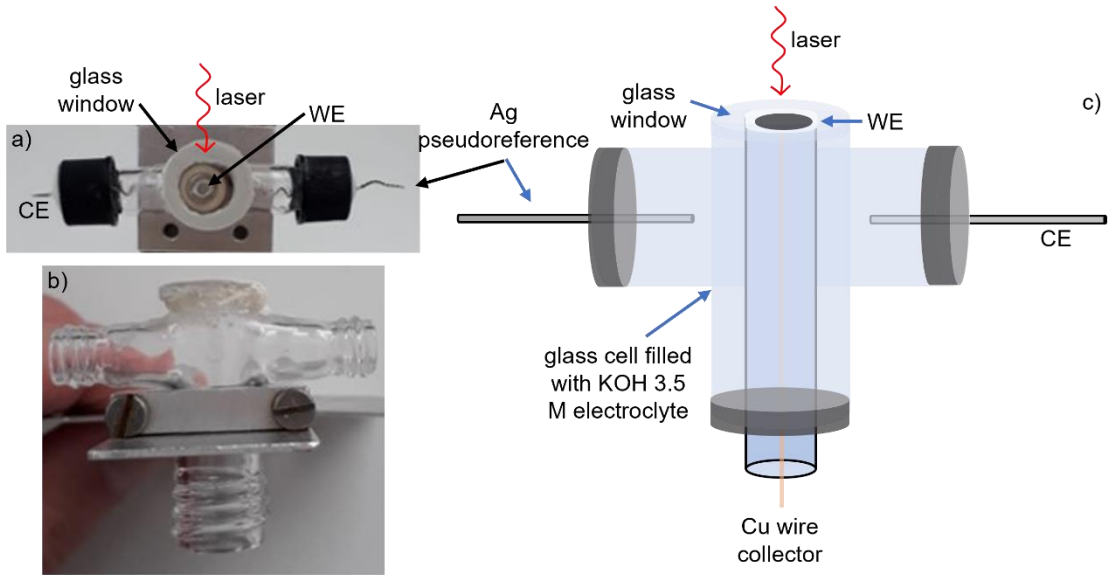

Figure 3.6.3: Three-electrode cell used for Raman spectro-electrochemical experiments; a) upper cell view. The WE is on the top of a glass covered electrode. The Raman spectroscopy is performed in reflection through the upper glass window. b) Front cell view without the electrode insertion. c) Three-electrode cell scheme for spectro-electrochemistry measurements.

Operatively, the experiment is carried out applying a voltage scan rate between the counter and the working electrodes, such as in a normal CV experiment, and collecting a Raman spectrum at each voltage step, for both the oxidation and the reduction curves.

The instruments used for Raman spectroscopy combined with cyclic voltammetry are a Horiba LabRam HR evolution and a Metrohm Autolab apparatus. The Raman apparatus is equipped with a 633 nm laser source and a 1800 l/mm grating and the Raman shift calibration is carried out with the 520.70 cm^{-1} Raman line of Si. The softwires used for the Raman spectra analysis were LabSpec 6 and Mathworks Matlab.

4. MATERIALS

This chapter is dedicated to the synthesis and to the physical characterization of the electrode materials. All the considered electrodes are made of graphene-based materials and graphene is the main component. Specifically, two graphene typologies are synthesized and investigated, such as thermally exfoliated graphene oxide (TEGO) and laser induced graphene (LIG). Both have a wide porosity distribution, large specific surface area, high defect density and are industrially scalable. Moreover, the defectiveness of such graphene materials enables a facile route for decoration with metallic and metal oxide nanoparticles. The decoration with nanoparticles is valuable from an electrochemical point of view, since it enables to introduce redox active sites, enhancing the material specific capacitance, and to build asymmetric devices with a wide electrochemical voltage window. Many techniques were used for their physical characterization, such as the methylene blue technique for surface area evaluation, SEM, TEM, powder XRD and Raman spectroscopy. Moreover, these materials were deeply characterized in past research works [35,39,76,77]. Regarding graphene-based materials, the aim of this thesis is to investigate their charge storage mechanisms with different electrolytes, both aqueous and organic Li-based electrolytes, as well as realizing and characterizing hybrid and asymmetric devices, in order to exploit the strengths of both SCs and batteries.

4.1. Thermally Exfoliated Graphite Oxide (TEGO)

Thermally exfoliated graphite oxide (TEGO) is obtained through high temperature graphite oxide thermal exfoliation. The graphite oxidation is obtained by the Brodie method [78]. The subsequent thermal exfoliation is carried out through a thermal shock at a temperature higher than 1000°C under dynamic vacuum, following a synthesis route earlier developed [35]. TEGO is chosen thanks to its good physical properties, its potential industrial scalability, and since this synthesis method enables to obtain a material without any contaminants with respect to other exfoliation methods [79]. TEGO is characterized by domains of few-layer graphene, with an average layers number of three, surrounded by amorphous carbon domains (Figure 4.1.1)

[43], resulting in a highly disordered material. TEGO displays high defect density (graphene platelets have a typical average lateral size of 12 nm) [43], good conductivity (9.4 S/cm [80]), large specific surface area of 650 m^2/g [80] and hierarchical porosity. More in detail, BET analysis shows that TEGO mainly possesses a micro- and meso-porosity arising from slit-shaped pores, as expected from aggregates of plate-like particles. Such features make TEGO an extremely encouraging material for electrode applications. Indeed, it is already demonstrated that such material behaves as a good negative electrode in LIBs [77,80,81].

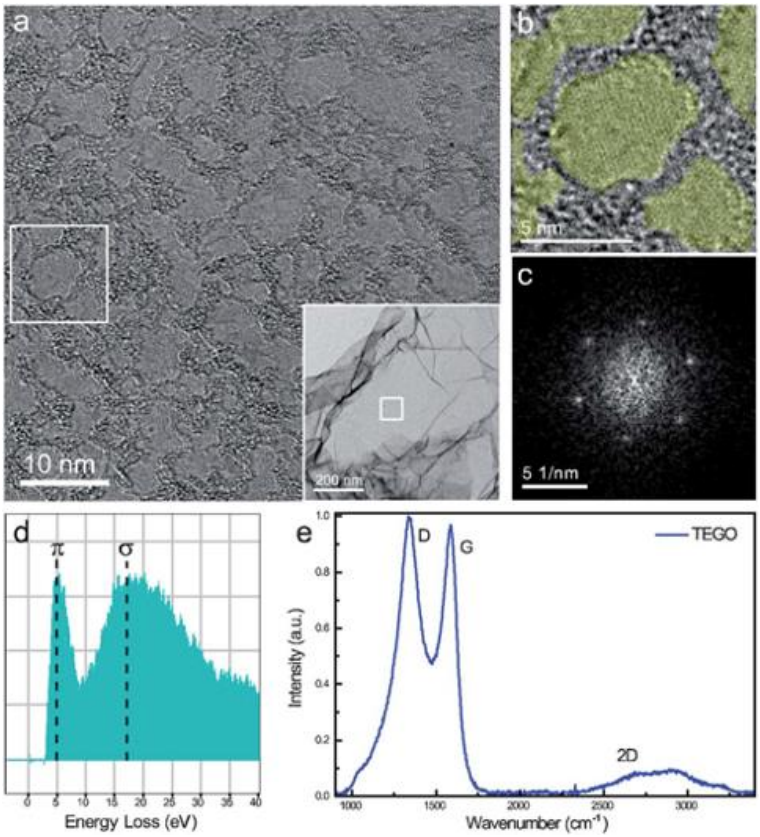

Figure 4.1.1: High-resolution TEM image of TEGO (magnification of the inset flat region). In the image are shown graphene domains surrounded by amorphous carbon regions. (b) Magnification of a graphene domain, which results made mostly by single layers highlighted in green. (c) Graphene domain Fast Fourier Transform, which proves the typical hexagonal graphene pattern. (e) Raman spectrum with the characteristic D, G and 2D bands of highly disordered few-layers graphene. [6]

Two different routes are followed for making the electrodes. In the case of aqueous electrolyte based SCs, graphene, dispersed in a solution of MilliQ® water and ethanol, 1:1 in volume, is deposited on a nickel foam disk, successively pressed for maximizing the contact between the nickel foam and the TEGO. Instead, for organic Li-based electrolyte, the TEGO is mixed with polyacrylic acid (PAA), 2:8 in weight, and n-methyl-2-pyrrolidone (NMP) in order

to obtain a slurry, subsequently deposited on a copper foil and dried at 70°C in dynamic vacuum.

4.1.1. Nickel decorated TEGO

With the aim to obtain a positive redox active electrode, TEGO is decorated with metallic nickel nanoparticles, successively electrochemically oxidized to nickel oxide-hydroxide through cyclic voltammetry in potassium hydroxide aqueous solution. The decoration undergoes via a well-established organo-metallic synthesis route and a subsequent thermal decomposition [43]. Precisely, the nickel acetyl acetonate ($Ni(acac)_2$), dissolved into a THF anhydrous solution, is mixed with a solution of THF and TEGO. The solution obtained is left under magnetic stirring overnight in an oil bath at 60°C, obtaining a homogeneous dispersion of the Ni precursor into the TEGO. All the procedure is made under an inert argon atmosphere. Then, the THF is removed via evaporation and using a nitrogen trap. The obtained solid solution, sealed in a two-exit vial, is placed in an oven at 300°C under dynamic vacuum for 15 min, removing the precursor solvent. The molar ratio between the nickel and the TEGO is 1:10. The material is, subsequently, physically characterized by high resolution and scanning transmission electron microscopy and by powder X-ray diffraction.

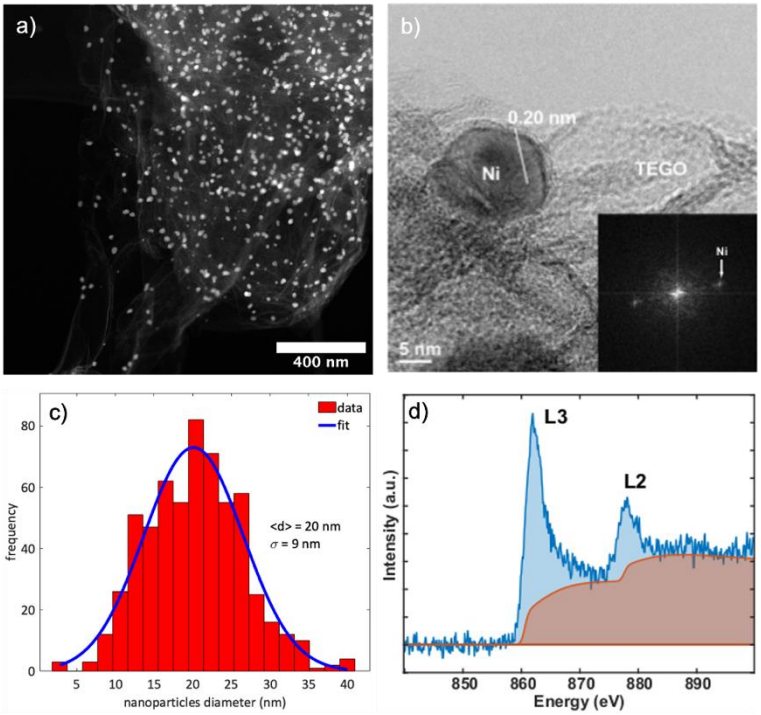

Figure 4.1.2: STEM, HRTEM, EELS and relative analysis of Ni-TEGO. a) STEM image of a Ni-TEGO sample. The Ni-NPs are visible as white dots well dispersed on TEGO; b) HRTEM image of a Ni-NP; c) diameter distribution of Ni-NPs obtained from the STEM image; d) EELS spectrum of Ni-TEGO.

The STEM image (Figure 4.1.2 a) reveals the effective decoration of the TEGO with nickel nanoparticles (Ni-NPs) with an average diameter of 20(9) nm, according with previous literature [43]. The Ni-NPs diameter distribution (Figure 4.1.2 c) is obtained analyzing the over 500 nanoparticles visible in the STEM image. The HRTEM image in Fig. 4.1.2 b) of a NP on a TEGO sheet presents fringes with a 0.20 nm distance relative to (101) reflection planes family of the hexagonal close-packed (hcp) metallic nickel structure. The diffractogram image is shown in in the inset. The EELS spectrum (Fig. 4.1.2 d) allows to determine the valence number of the nickel, which results in +0.6(0.2). The Ni partial oxidation is attributable to the sample air exposition occurred during the microscope analysis preparation.

The powder X-ray diffractogram (Figure 4.1.3) confirms the precursor total decomposition into metallic nickel presenting three wide peaks at 39.3°, 42.6° and 44.5° of 2θ, which correspond respectively to the (100), (002) and (101) plane reflections of hexagonal $P6_3/mmc$ metallic nickel structure, refined with Rietveld refinement method. It is worth to say that the 45° peak calculated intensity does not match with the experimental data. It suggests that a minority Ni cubic phase (fcc), which has its main peak at 44.6°, should be also present. Furthermore, it

justifies the observed asymmetric peak broadening since it could be related to phase transition stacking fault and strain defects between the two structures. Moreover, the Scherrer analysis of Ni peaks broadening allows to determine 14(5) nm Ni-NP crystal average diameter, which agrees with the STEM analysis. Lastly, around 24° of 2θ is present a wide band associated with the (002) reflections of few-layers graphene nanocrystals, according with previous literature [82].

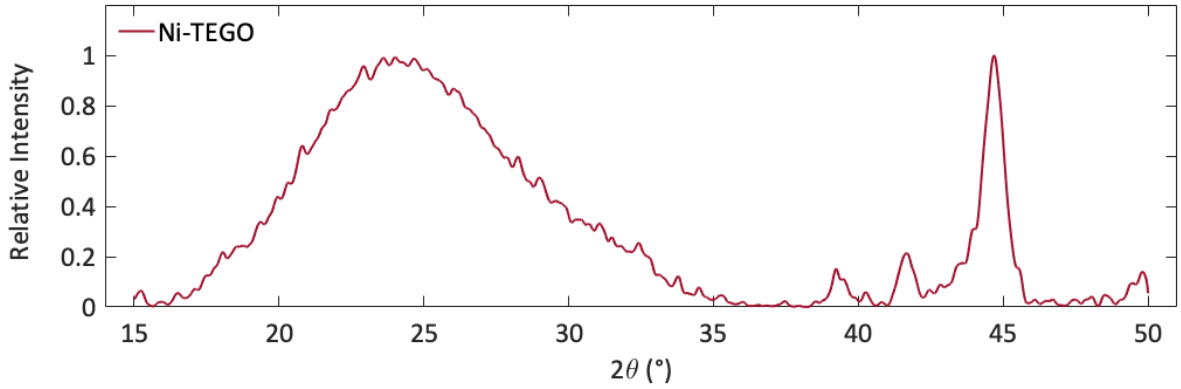

Figure 4.2.3: powder X-ray diffraction pattern of Ni-TEGO.

Since the TEGO is decorated with nickel for obtaining a positive electrode for aqueous electrolyte SCs, the Ni-TEGO is deposited on a nickel metallic foam, following the same procedure of TEGO.

4.2. Laser Induced Graphene (LIG)

Laser induced graphene is obtained through photo-thermal conversion of polymeric precursor rich of aromatic carbon cycles. Specifically, the precursor used is Kapton®, which is a commercial polyimide film with three aromatic rings in a single monomer (Figure 4.2.1). The graphene presence in the final materials is mostly dependent on the number of aromatic rings, i.e. the number of sp^2 bonds maintained after the synthesis treatment, which give to the material a graphene-like dress and behavior. The synthesis of LIG consists in the exposition of the polymeric film to high power CO_2 laser [36,83]. The synthesis route is very simple and, therefore, industrially interesting since it is highly scalable.

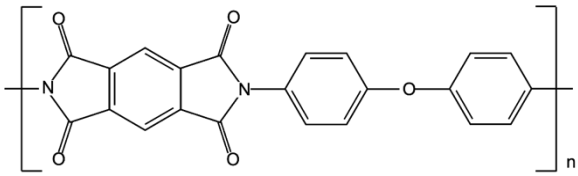

Figure 4.2.1: Kapton® monomer. In its structure are present three carbon hexagons, typical of an ideal graphene pattern, and two pentagons.

During the conversion, nitrogen and oxygen atoms detach from the polymeric chain, leaving a defective porous structure made of carbon atoms only, mainly arranged in hexagons, pentagons and amorphous carbon [36].

For the polyimide conversion, it is initially used an industrial laser cut machine t for high power applications, i.e. a RM-Lasermark 1613 with a 100 W nominal maximum power, at the Parma FabLab, an incubation facility for innovation projects. Since polyimide photo-thermal conversion occurs at lower laser power, the machine is used between a maximum power of 22 W (the 22% of its nominal value) and a minimum value of 11W (11% of P_{max}). It is worth to say that below that power value the laser is unstable and the machine is unable to work. This research brought a collaboration with the Start-up ESANanotech® and to the development of dedicated machine for the conversion of polyimide in graphene.

The material synthetized this way has promising characteristics for micro-electronic applications since it is attached to an insulator substrate (polyimide), which is flexible, and has a thickness of few micrometers, tunable as a function of the substrate thickness and of the conversion deepness. The design chosen for the material is a two electrodes interdigitated geometry, displayed in Figure 4.2.2, with a fingers thickness of 2 mm separated by a 0.4 mm of unconverted polymer, which is the minimum distance for avoiding the undesired connection between the electrodes. The geometry is chosen in order to obtain prototypes for SC application.

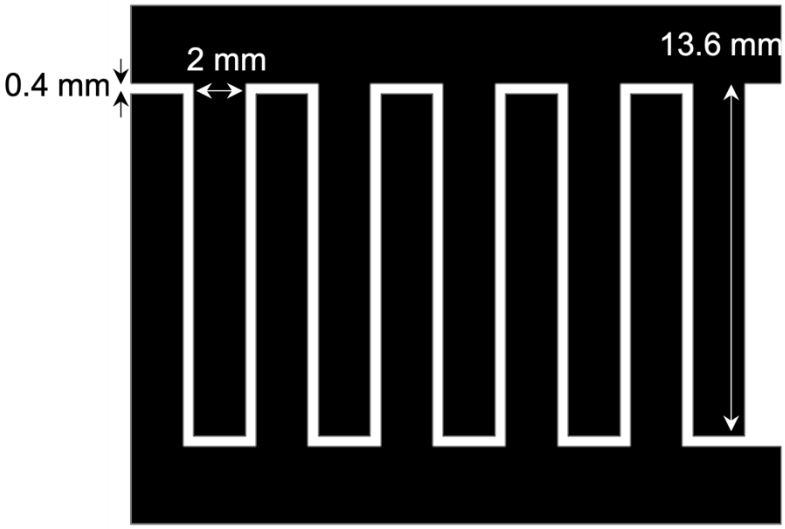

Figure 4.2.2: Laser induced graphene interdigitated design image. The black and white areas correspond, respectively, to the sectors for the conversion and leave unconverted.

The laser cut machine has four tunable parameters which determine the type of conversion of the polymer in graphene-based material. Specifically, since the work time at the facility was limited, it was chosen initially to fix the height of the laser head, keeping the film at the laser spot focus, and to tune the laser scanning speed, the overlapping of successive conversions, which is identified by the distance of two converted line, and the laser power. The sample production parameters were chosen in order to obtain the most possible uniform and mechanically stable material, avoiding its ablation during the synthesis process. In Figure 4.2.4 are shown some examples of optical microscope images of sample, together with their synthesis parameter. It is worth noting that a power increment over 16 W allows to obtain a more porous carbon material, but mechanically instable, which tends to detach from the substrate. The sample chosen for further analysis is the LIG-12-200-50, i.e. produced with a 12W power, a 200 mm/s scanning speed and an overlap of 50 µm.

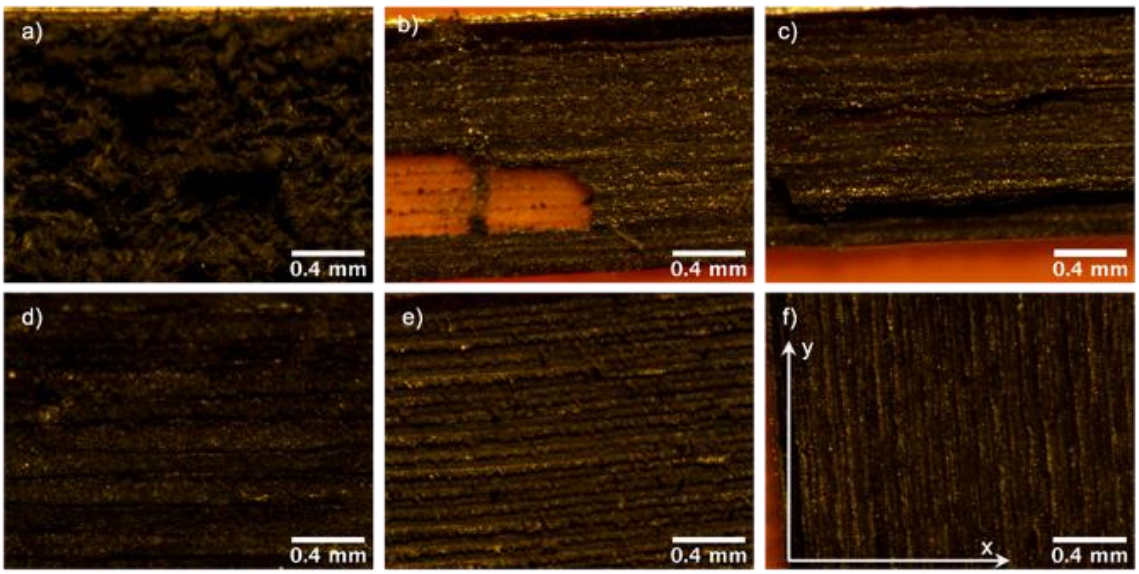

Figure 4.2.4: Optical images of LIG examples. The synthesis parameters, nominally power, scanning speed and overlap, for each sample are: a) 20 W, 400 mm/s, 0.1 mm; b) 18 W, 300 mm/s, 50 µm; c) 16 W, 300 mm/s, 50 µm; d) 15 W, 400 mm/s, 50 µm; e) 14W, 250 mm/s, 50 µm; f) 12W, 200 mm/s, 50 µm; The sample f) was chosen for further characterizations.

The sample LIG-12-200-50, displayed in Figure 4.2.4 f) and in Figure 4.2.5, even if optimized, still presents a non-uniform conversion. This is due to a non-equally distributed power on the laser converted zones. Precisely, it is observed a conversion difference between the edges and the center of the irradiated sections.

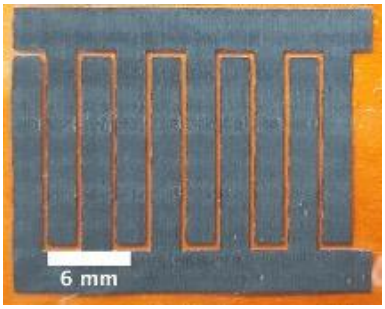

Figure 4.2.5: Optical images of LIG sample with the interdigitated design. The conversion is occurred with a 12W power, 200 mm/s scanning speed and 50 µm of overlap parameter.

In fact, the conductivity along the y axis (49.4 ± 0.5 S/cm) is 3 times higher than the x axis (14.0 ± 0.3 S/cm) of figure 4.2.4 f), confirming the non-uniform conversion. However, it owns a good ohmic behavior in both the x and y directions, which is displayed in Figure 4.2.6 a) and b). Precisely, the conductivity is higher along the laser movement direction and lower along the

orthogonal one. The conductivity is evaluated by a four-probe conductivity experiment, applying the Van Der Pauw method and, specifically, equation 4.2.1, which is valid for thin film samples, i.e. with *W* (the thickness) << *d* (contact distance). The sample thickness, 15(5) µm, is evaluated analyzing a cross-sectional microscope optical image.

$$\sigma = \frac{\ln 2}{\pi W} \frac{I}{V} \qquad \textit{Eq. 4.2.1}$$

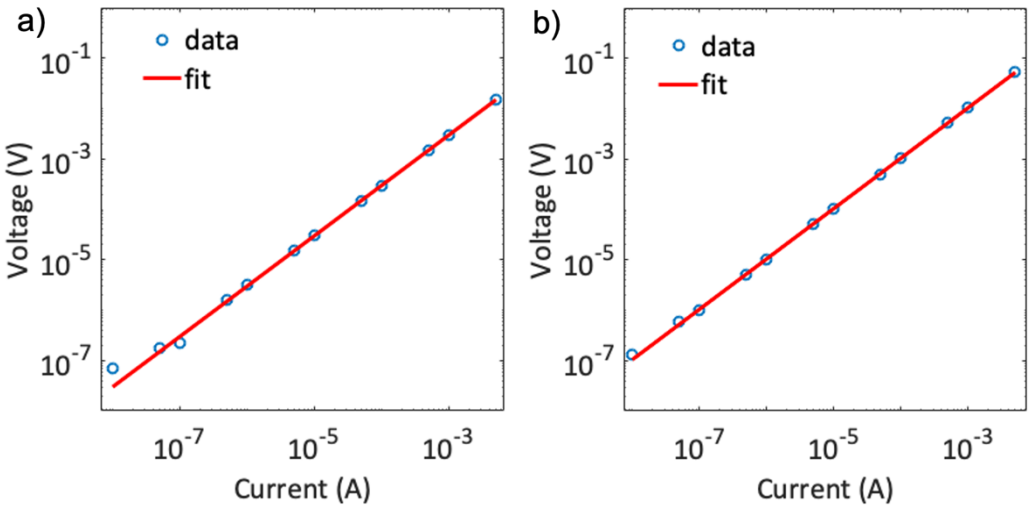

Figure 4.2.6: Ohmic behavior of LIG along the y (a) and x (b) axis directions of Figure 4.2.5.

The chosen sample is successively characterized with SEM, with methylene blue technique (explained below) and with Raman spectroscopy. The SEM images, displayed in Figure 4.2.7, confirm the difference of conversion already explained, and outline the wide range porosity of the material at the micro-scale. In the left image, the conversion lines are recognizable from the macro-pores obtained mainly along the edges, which are magnified on the right image.

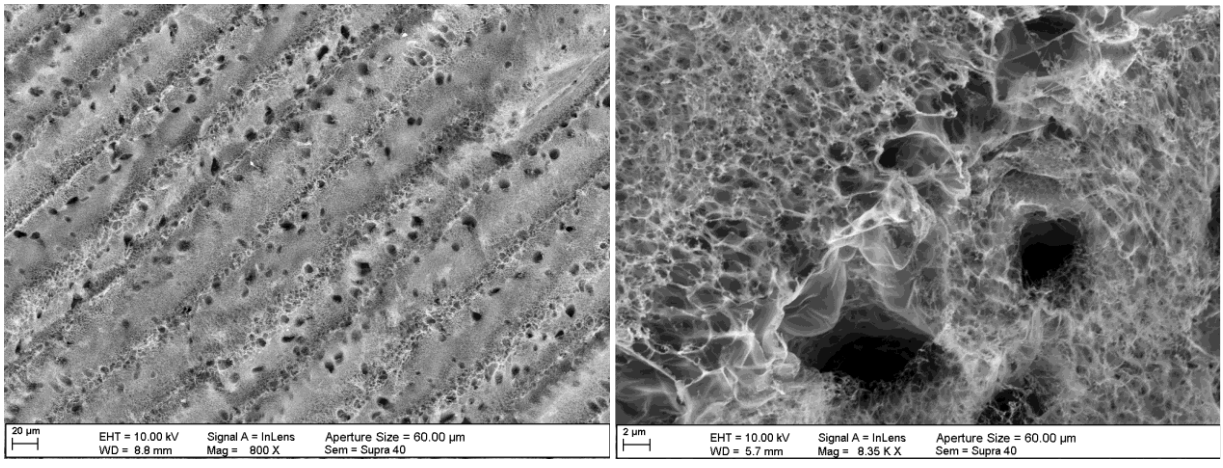

Figure 4.2.7: SEM images of sample 12-200-50.

The methylene blue technique is a useful method for the specific surface area evaluation when a small material mass amount is available [84,85]. It determines indirectly the surface area evaluating the concentration variation of a methylene blue solution by an UV-VIS absorbance spectroscopy experiment. The methylene blue molecule has a dimension between 10.2 nm to 10.8 nm [85] and, since it is absorbed by porous materials and covers uniformly the surface areas, the number of absorbed molecules gives indirectly the surface area value. The specific surface area, evaluated by this method, resulted of 200(10) m^2/g, which is comparable with the specific surface area of other graphene-related materials obtained with similar methods [41,77,86,87].

Finally, Raman spectroscopy is performed on LIG samples collecting the spectra on the edge and on the center of the converted area. The spectra collected (Figure 4.2.8) in both cases exhibit the characteristic peaks (D, G and 2D) of a defective graphene-like material.

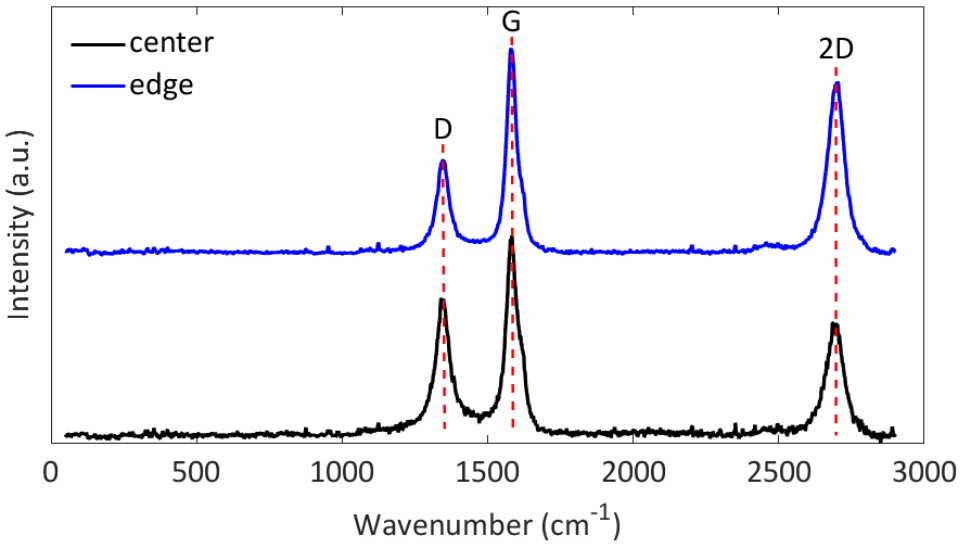

Figure 4.2.8: Raman spectroscopy spectra of LIG 12-200-50 collected at the center (black) and at the edge (blue) of the laser converted region. The blue spectrum shows a higher G-D and 2D-G peak ratios.

In fact, while the G peak is associated with the first order phonon modes at the center of the Brillouin zone (E_{2g} symmetry), and is always present in sp^2 carbon materials, the D peak, being a second order modes related to breathing sp^2, is activated from the presence of defects [88]. From the comparison of D and G peaks intensity, I_D and I_G respectively, it is possible to evaluate the graphene flakes lateral size and the defect density following equations 4.2.2 a) and b), where λ_L is the laser wavelength (532.1 nm).

a) $$L_D(nm) = \left(1.8 \times 10^{-9} \frac{I_G}{I_D}\right)^{1/2} \lambda_L^2$$

b) $$n_D(cm^{-2}) = \frac{1.8 \times 10^{22}}{\lambda_L^4}\left(\frac{I_D}{I_G}\right)$$

Eq. 4.2.2

The two spectra differ in the relative intensity of the D peak and, as a consequence, in the amount of defects and in the width of graphene flakes. In fact, the lateral size results higher at the edge of the converted area (18(5) nm) than at the center (14(4) nm). Regarding the defect density, the trend is obviously inverted, with the center of the conversion regions resulting more defective (1.6(4) × 10^{11} defects/cm^2) than the edge (1.0(3) × 10^{11} defects/cm^2). Such difference might be related with the conversion features observed in the SEM images of figure 4.2.7, i.e. with the pore size difference between the conversion edges and centers. In fact, the smallest pores are seen at the center of the converted areas, which are interested by a higher laser power density, generating more defects and tightening the size of graphene flakes. On the other hand, larger pores are found in the regions affected by a minor laser power density of conversion, achieved at the edge of the laser spot, translating in flakes with a higher lateral size and a minor defectivity [89]. The last peak, nominally the 2D band, is related to second order vibrational modes of the D peak, and it is associated with the number of layers. Precisely, single layer graphene has a single peak which splits into a 4-bands in few-layer graphene and molds into an asymmetric peak in graphite [88]. Thus, being the 2D band a single peak, it is plausible that a certain amount of single layer is present [90]. Moreover, the peaks broadening might be due to the disordering and inhomogeneous nature of the graphene [91].

4.2.1. TiO_2 decorated LIG

In order to enhance the LIG specific capacitance, the decoration of the material with titanium dioxide is investigated [41]. The TiO_2 choice was made paying attention to the eco-compatibility of the final electrodes, its high chemical stability and to our previous results, as previously described in the 3rd chapter. The decoration was obtained by simultaneously

converting under the laser influence both the polymer and a TiO_2 precursor, respectively into graphene and TiO_2. As a precursor for TiO_2, it was identified a titanium tetra-isopropoxide (TTIP) sol-gel solution with ethanol and water. During the sol-gel process, the TTIP undergoes to a hydrolysis reaction, releasing ethanol. Thus, an amorphous phase of titanium dioxide was formed. Then, the sol-gel was deposited with a home-made spin-coater onto the polyimide film in order to obtain a uniform covering. Subsequently, the sample was treated with the laser cut machine using a 14 W power, slightly higher with respect to the required power for the conversion of bare polyimide, a scanning speed of 200 mm/s and an overlap of 50 µm. In figure 4.2.9 a) it is shown an optical microscope image of the polyimide covered with TiO_2 film, after the laser treatment. At the optical microscope it appears almost unchanged with respect to the sample LIG12-200-50 but, as shown in SEM images in Figure 4.2.9 b) and c), the morphology is slightly different, with a higher number of macro-pores (bigger than 50 nm). Moreover, the graphene results to be successfully decorated with titanium dioxide particles of a micro-meter size, appearing brighter in the SEM images of figure 4.2.9.

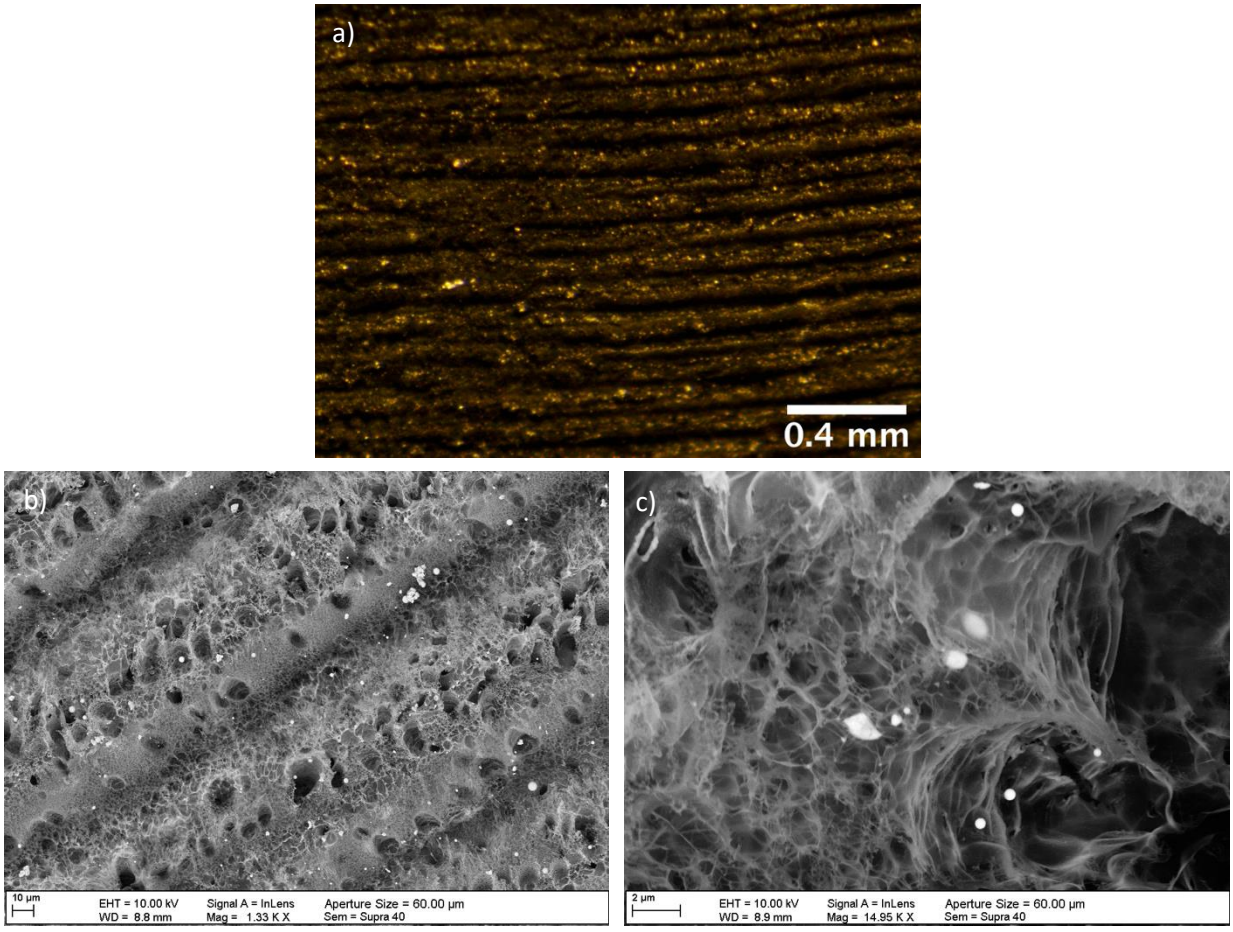

Figure 4.2.9: Optical (a) and scanning electron (b,c) microscope images of TiO_2 decorated LIG.

The effective recrystallization of TiO_2, although partial and non-uniform, is proved by Raman

spectroscopy (Figure 4.2.10). In fact, either rutile, anatase and amorphous titanium dioxide are found in the sample [92–94]. Noteworthy, the treated TiO_2 was mainly a multi-phase structure, presenting a main phase and, at least, a secondary phase. Specifically, anatase spectrum (blue line) has a minor contribute from rutile, rutile (green line) from anatase, amorphous (gray and black lines) from both rutile and anatase. It suggests that the laser irradiated power, as previously stated, is non-equally distributed over the laser spot area, thus causing a non-uniform conversion of polyimide and a partial recrystallization of the TiO_2. The black line identifies the unreacted amorphous titanium dioxide.

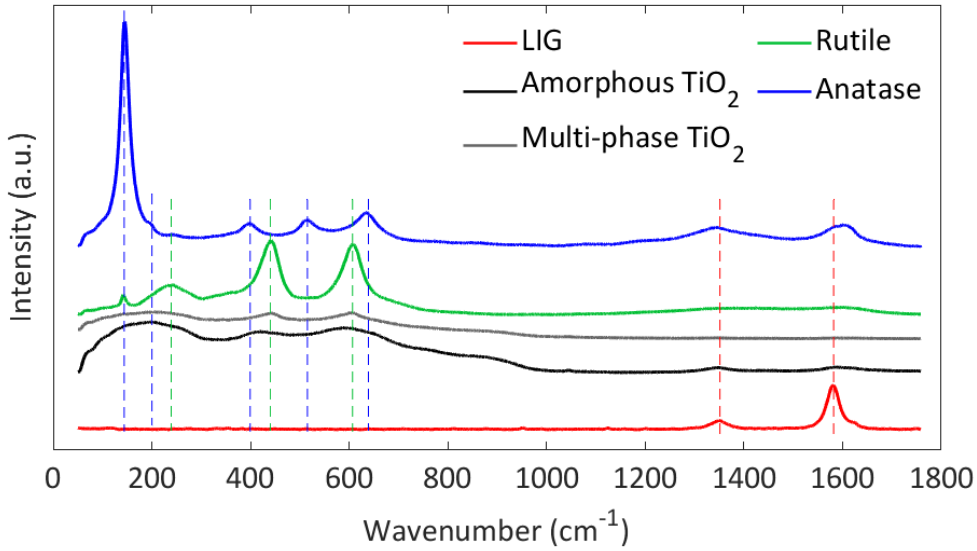

Figure 4.2.10: Raman spectra of four different TiO2 grains. Each grain presents a main phase (curve color) and at least a minor phase highlighted by the dashed lines of the same color. The red spectrum is collected on an area of the sample without the TiO_2 decoration and corresponds to the spectrum of laser induced graphene. The red dashed lines indicate the graphene D, G bands.

5. TEGO-BASED AQUEOUS ASYMMETRIC HYBRID SUPERCAPACITOR

In order to extend the stability voltage window over the water evolution limit, enhancing the SC specific energy, a hybrid SC with an asymmetric configuration is explored. Nickel decorated TEGO (Ni-TEGO) is used as a positive electrode and TEGO is exploited as a negative electrode. The SC is working with a KOH 3.5M aqueous electrolyte. The aim to couple the Ni-TEGO with TEGO is to build an asymmetric device, where the positive electrode is built in-situ during cycling. In fact, in the first cell cycle Ni nanoparticles anchored to TEGO sheets easily react with OH- and undergo an irreversible reaction to NiOOH, which has a Nernstian quasi-reversible process to $Ni(OH)_2$ in the voltage window 0-0.6V. As described in the Chapter 2, coupling a battery-like electrode with a capacitive one enables to enlarge the operative voltage window. This chapter is dedicated to the study of an asymmetric hybrid SC based on TEGO, and to its performance evaluation, investigating different mass ratios between the positive and the negative electrode. This work has been also published in a peer-reviewed journal [46].

5.1. Nickel oxidation to nickel oxide-hydroxide

5.1.1. Three-electrodes cyclic voltammetry

The positive electrode formation is investigated by a three-electrode CV experiment, performed on the Ni-TEGO electrode, shown in Figure 5.1.1. The first and the second cycle are compared, observing the differences. In the very first oxidation, CV curve presents a peak at 0.58 V with respect to the Ag/AgCl RE. Such high peak disappears in the second cycle, lowering its height and shifting to lower potential, suggesting the irreversible nature of the first process, which corresponds to the oxidation of Ni to $Ni(OH)_2$ and to NiOOH. This process has been clearly confirmed by extensive analysis discussed below [46], such as spectro-electrochemical characterization, p-XRD, HR-TEM. On the other hand, the second cycle peak (at 0.5 V vs RE)

corresponds to the oxidation of $Ni(OH)_2$ to NiOOH. During the reduction curve, both the first and the second cycles exhibit a reduction peak at 0.3 V with respect to the RE, associated to the reduction of NiOOH to $Ni(OH)_2$ [46,53].

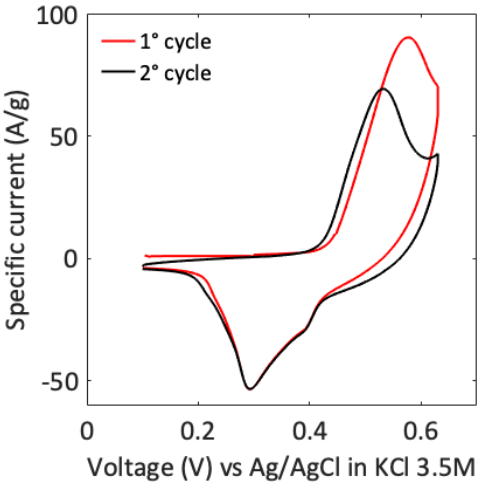

Figure 5.1.1. Oxidation of TEGO Ni-NPs into NiOOH monitored by three-electrodes CV.

5.1.2. TEM characterization

The morphology changes of Ni-TEGO structure, due to the oxidation of Ni-NPs, are observed by means of TEM measurements on cycled electrodes. Such images, with the relative analysis, are displayed in Figure 5.1.2 and 5.1.3. The Ni nanoparticles (Ni-NPs) fall apart into a complexed coverage on TEGO sheets, with a rough structure, shown in STEM and HRTEM images of Figure 5.1.2 a) and b). As a comparison, Ni-NPs on a TEGO sheet of the non-oxidized sample are shown in Figure 5.1.2 d). The inset diffractogram pattern of Figure 5.1.2 b) shows a broad ring related to the $Ni(OH)_2$ structure plane reflections (001). The NiO presence, highlighted in the diffraction pattern of Figure 5.1.2 b) derives from the dehydration of the $Ni(OH)_2$ exposed to the 200 keV electron beam. The EELS line edges, shown in Figure 5.1.2 c), present a very different shape from that of the metallic nickel, shown in the 1st section of the 4th chapter. In fact, the valence number, which is evaluated from the L2 and L3 ratio following literature route [95], results of +1.8(0.2), accordingly to the oxidation number expected for $Ni(OH)_2$.

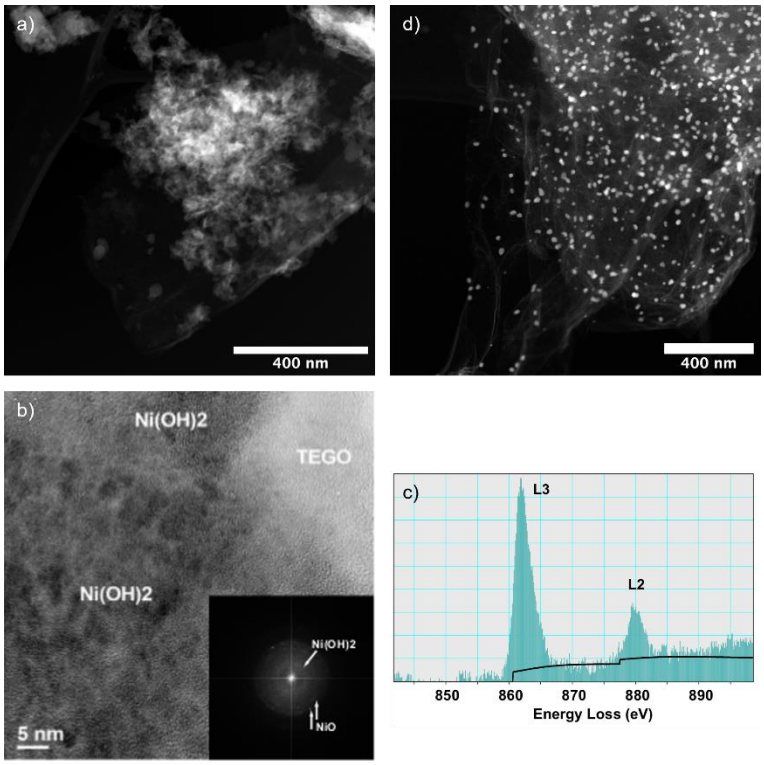

Figure 5.1.2: TEM characterization of $Ni(OH)_2$-TEGO. a) STEM image of a $NiOH)_2$ complex covering the TEGO sheets. b) HRTEM image of $Ni(OH)_2$-TEGO; in the inset is shown the diffractogram of $Ni(OH)_2$. The NiO presence is due to the influence of the microscope. d) STEM image of Ni-TEGO sample previous oxidation. Ni-NPs are outlined as white dots on a TEGO sheet, visible in the background.

The effective coverage of TEGO with oxidized Ni is confirmed by the EDX analysis, displayed in Figure 5.1.3. Here, the presence of carbon (b), nickel (c) and oxygen (d) is outlined by the EDX signals. The nickel and the oxygen signals match the brighter area of the annular dark-field (ADF) STEM image (a), where the carbon (b), being with lower atomic number, is only partially visible.

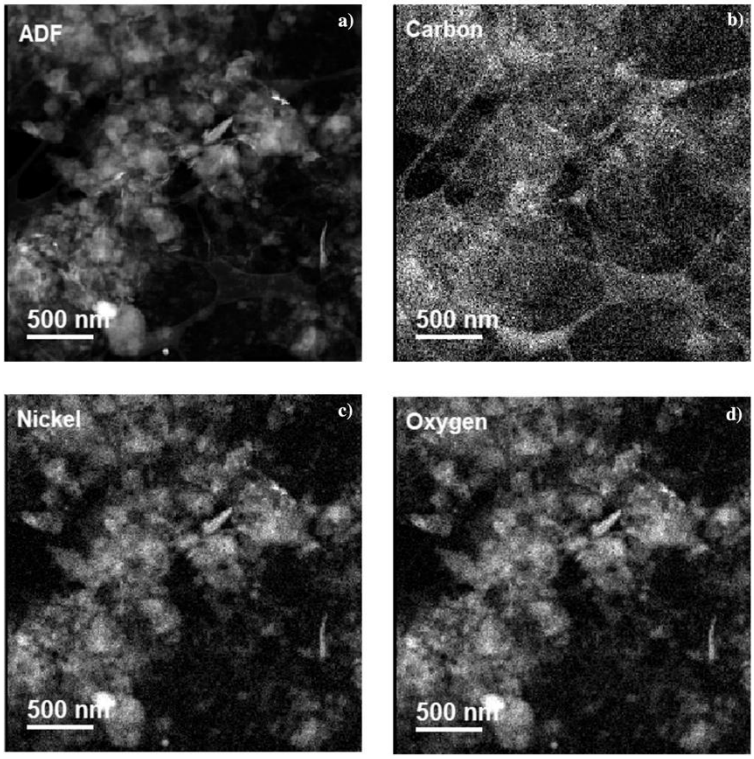

Figure 5.1.3: STEM images with EDX analysis. a) STEM pristine image. b) EDX carbon signal. c) EDX nickel signal. d) EDX oxygen signal.

5.1.3. Powder X-ray diffraction

The crystalline structure of the $Ni(OH)_2$-TEGO, i.e. of the sample after the oxidation, is investigated with powder X-ray diffraction (Figure 5.1.4 black diffractogram). The metallic Ni peaks (2θ=39.3°, 42.6° and 44.5°, marked in red) of the Ni-TEGO pattern (shown in blue) disappear completely after the oxidation. In their place, three broad bands appear in the ranges 10° - 30°, 32° - 35° and 36° - 40° of 2θ due to the presence of both $Ni(OH)_2$ and NiOOH. Specifically, the peaks at 21°, 33° and 40° of 2θ, highlighted in green, are related to the (001), (100) and $(101)/(\bar{1}0\bar{1})$ plane reflections of the $P\bar{3}m1$ hexagonal structure of β-$Ni(OH)_2$ [96]. The first reflection coincides with that observed in the TEM diffraction. On the other hand, the peak at 13°, the broadening of the band between 20° and 30°, and the asymmetric shape of the peak around 38° of 2θ, suggest the presence of γ-NiOOH, which has its main peaks at 13°, 25°, 28°, 37° and 38° of 2θ, corresponding respectively to the (003), (006), (101), (102) and (104) plane reflections [97]. Its presence could be due to a non-complete reduction of the

sample during the electrochemical preparation performed in cyclic voltammetry. The main contribute to the wide band around 25° (marked in gray) is due to the graphene structure. The presence of a diffuse broadening throughout the pattern suggests a highly disordered structure with small domains of nickel hydroxide forms, which is in agreement with the STEM images of a $Ni(OH)_2$ complexed coverage of TEGO, previously shown.

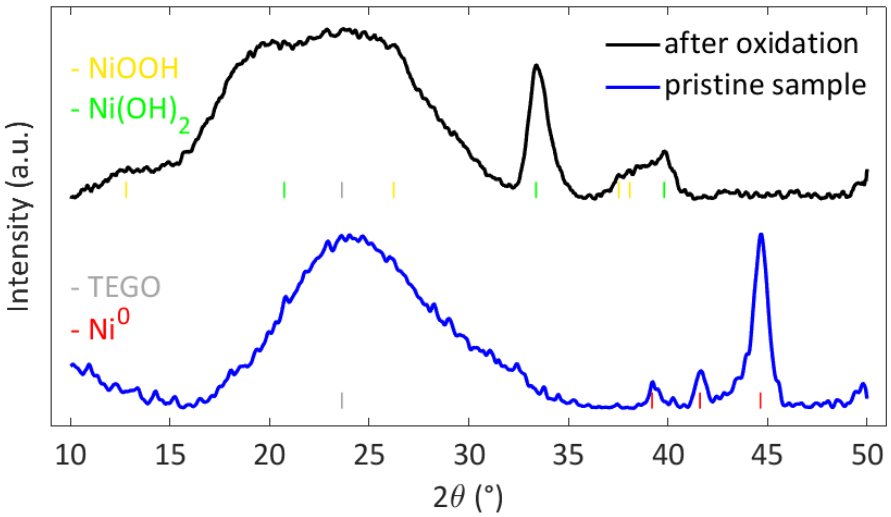

Figure 5.1.4: powder X-ray diffraction pattern of $Ni(OH)_2$/NiOOH-TEGO (blue), thus after the oxidation, and of Ni-TEGO pristine sample before the oxidation (black). The peaks of NiOOH (yellow), $Ni(OH)_2$ (green), TEGO (gray) and Ni^0 (red) are highlighted.

5.1.4. Raman spectro-electrochemistry

The oxidation and reduction processes are further investigated by Raman spectroscopy combined with three-electrode CV measurements. These measurements have been carried out during a traineeship at the Heyrovsky Institute of Physical Chemistry of Prague, under the supervision of Prof. Martin Kalbac. Raman spectro-electrochemistry, perhaps well known among electrochemist, is not a very common technique, thus, in order to understand how the combination of three electrode CV and Raman spectroscopy is carried out, more experimental details are needed. Specifically, the experiment is performed applying a low voltage scan rate, hence maintaining the voltage level constant for a long time. During the time interval at a constant voltage level, a Raman spectrum is acquired. Reaching a tradeoff between the

available time and an accurate characterization, a voltage step of 0.05 V and a time step of 350 s are chosen, resulting in an equivalent 140 µV/s voltage scan rate. During each time interval, a Raman spectrum is acquired in the wavenumber window (300-900) cm^{-1}, with a 30 s acquisition time, repeated 10 times, thus resulting in a total time of 300 s for each spectrum. The electrode investigated is a slurry of Ni-TEGO mixed with PVDF and deposited on a Cu collector. In order to prevent the contact between the copper and the electrolyte, the electrode is finely sealed on the top of a glass tube with the Torr-seal epoxy resin, as deeply described by Figure 5.1.5.

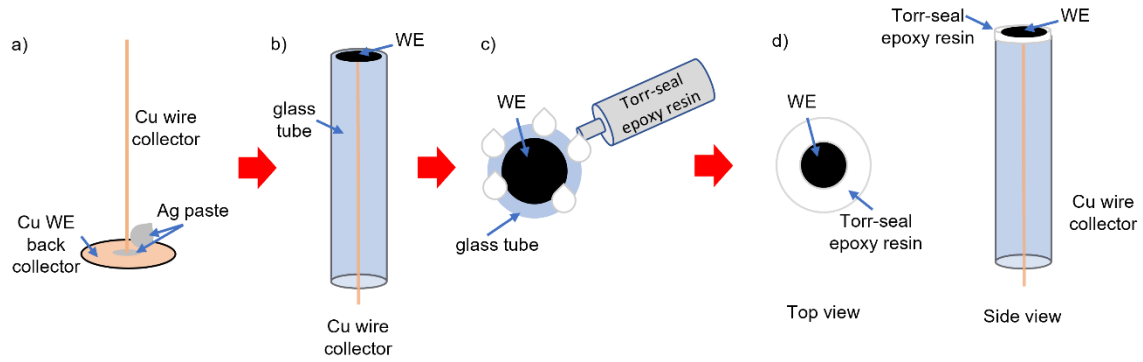

Figure 5.1.5: Preparation of the Ni-TEGO WE for Raman spectro-electrochemistry measurements. a) The working electrode is contacted on the back with a Cu wire by mean of silver paste; b) the copper wire is inserted in a glass tube, while the WE is set on the top; c): sealing of the contact point between the glass tube and the WE by mean of Torr-seal epoxy resin; d) WE final appearance from the top and from the side.

The Ni-TEGO spectrum, before the irreversible oxidation to NiOOH, is compared in Figure 5.1.6 b) with the spectra of NiOOH-TEGO and of $Ni(OH)_2$-TEGO recorded in three electrodes CV. The Ni-TEGO spectrum (pristine blue curve) shows a broad peak between 330 cm^{-1} and 490 cm^{-1} compatible with the TO and LO vibrational modes of NiO, according to literature [98]. Its presence is probably due to the spontaneous oxidation of Ni-NPs once exposed for long times to air during the electrode preparation. In fact, it was not detectable in the X-ray powder diffraction performed on the sample not exposed to the ambient conditions. After the oxidation, occurred at 0.55 V vs Ag RE in the electrochemical cell, the NiO peak disappears and two peaks rise at 477 cm^{-1} and 557 cm^{-1} related, respectively, to NiOOH E_g and A_{1g} vibrational modes [99]. Finally, after the reduction, which occurs at 0.4 V with respect the Ag RE, the NiOOH peaks are substituted by the wide band between 250 cm^{-1} and 550 cm^{-1}, which might be associated to the 315 cm^{-1} E_g, to the 450 cm^{-1} A_{1g} and, to the 510 cm^{-1} acoustic modes of

$Ni(OH)_2$ [100]. The other features might be due to the substrate, to the binder, to the KOH aqueous electrolyte or to graphene impurities which do not participate in any reaction. The evolution of the WE Raman spectrum is accurately recorded as a function of the voltage, and it is shown for completion in Figure 5.1.6 a) for two CV cycles.

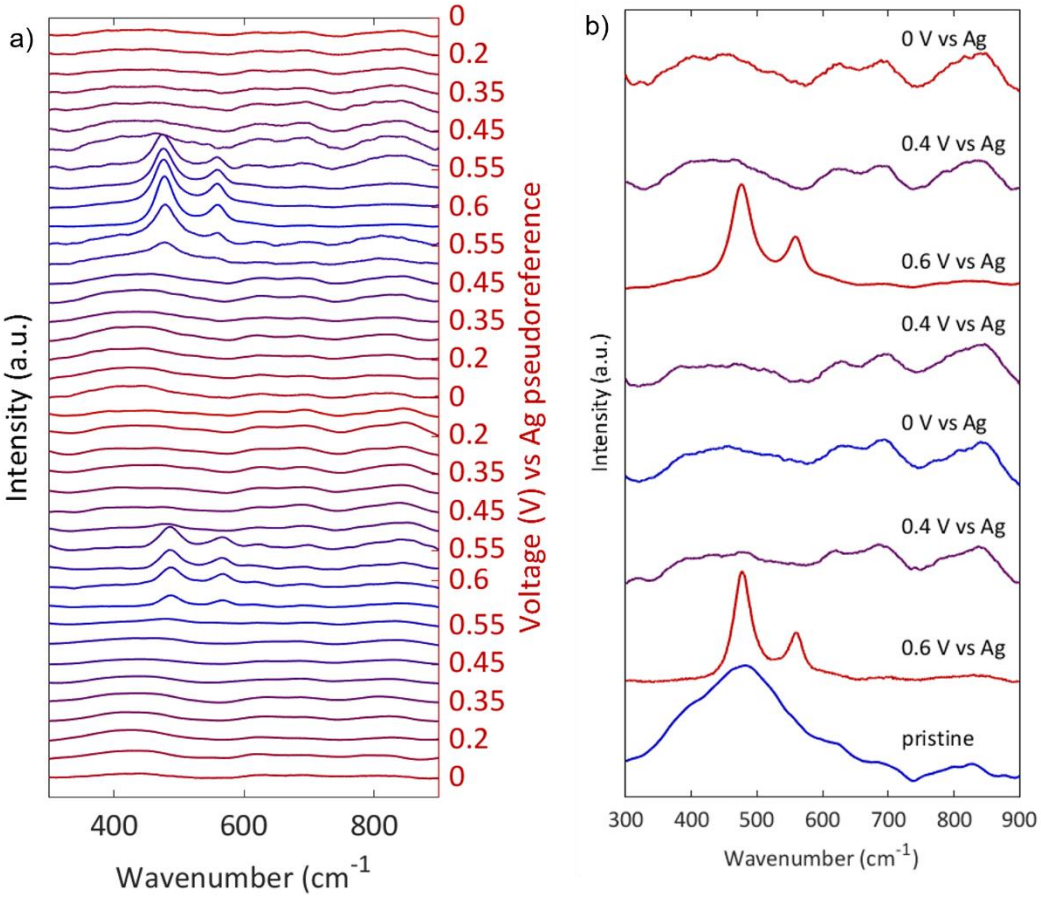

Figure 5.1.6: Raman spectroscopy combined with three-electrodes CV. a) Raman spectra graphed as a function of the three-electrodes CV voltage. b) three electrodes CV cycle relative to the spectra in (a).

Moreover, in order to have deeper insights on the electrode evolution, the 2nd cycle is shown in Figure 5.1.7 a) in a 3D representation. The two present peaks start rising at 0.5 V vs Ag pseudo-reference electrode, suddenly reach their maximum at 0.6 V, then decrease disappearing totally at 0.4 V with respect the Ag reference electrode. In Figure 5.1.7 b) the three electrodes CV of $Ni(OH)_2$-TEGO acquired with an equivalent voltage scan rate, but with shorter voltage steps, are shown. The CV potential and the shape of the CV curves slightly change from those already shown in this thesis. It is probably due to Ag pseudo-reference electrode and to the different electrode preparation, constrained imposed by the peculiar spectro-electrochemistry set-up. Although, the CV curve reflects accurately the behavior

noticed by the Raman spectroscopy spectra, i.e. the oxidation and reduction of the redox-active couple, at 0.55 V and 0.4 V with respect the RE, respectively.

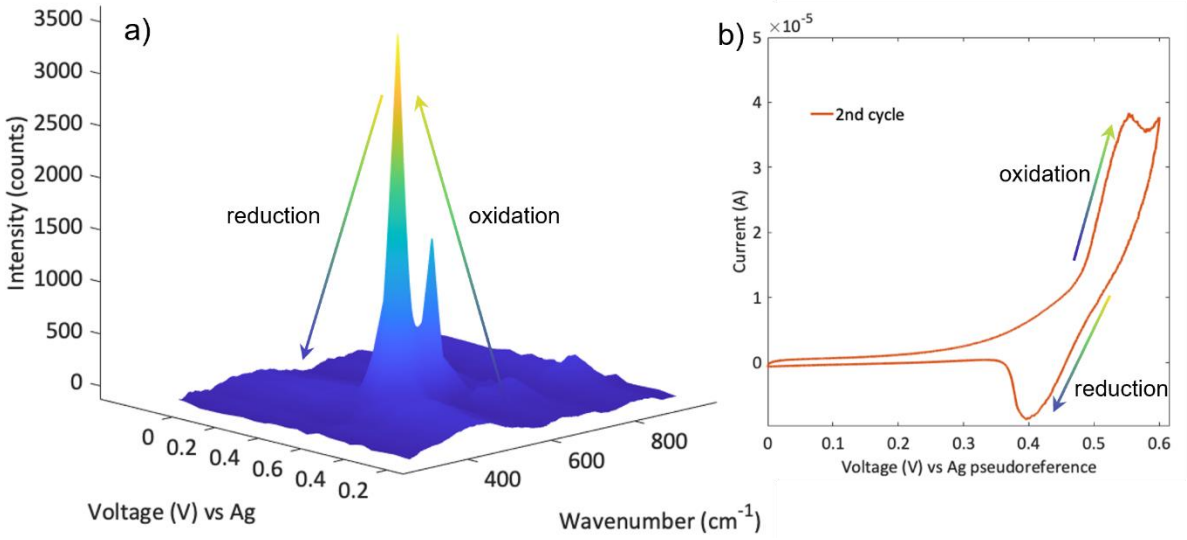

Figure 5.1.7: Raman spectroscopy combined with three-electrodes cyclic voltammetry. a) Raman spectra graphed as a function of the three-electrodes CV voltage. b) three electrodes CV cycle relative to the spectra in (a).

5.2. Three-electrodes cyclic voltammetry

Three-electrodes CV experiments are carried out to evaluate the electrodes electrochemical behavior. Specifically, their storage charge capability and their voltage stability windows are evaluated, allowing to design the asymmetric hybrid SC. The working electrodes preparation consisted in the deposition of the active material, previously dissolved in a solution of MilliQ water-ethanol, 1:1 in volume, on nickel foam by drop casting. The nickel foam is chosen as a collector since it is conductive and able to entrap the active material without using any binder. Its electrochemical activity is negligible in the investigated voltage windows. Specifically, being nickel redox-active in the voltage window 0 V – 0.6 V, the Ni-foam charge capability is evaluated and resulted 45 mC, which is negligible with respect the 1.2 C $Ni(OH)_2$-TEGO one. Both the set-ups consisted in a swagelok three-electrodes cell with Ag/AgCl RE, which is in contact with the 3.5 M KOH electrolyte through a buffering saturated KCl aqueous solution. A Pt disk is used as a counter electrode.

The TEGO is investigated upon the voltage window 0 V to -1 V, and its CV curve (Figure 5.2.1 a) exhibits a quasi-rectangular shape, indicating the capacitive nature of the main contribute to the capacitance. This slightly deviates from an ideal capacitive behavior, due to two small peaks between -0.6 V and -0.45 V, which suggests the presence of faradaic effects. Such mechanisms, accordingly to the literature, might be related to residual oxygen-containing groups attached to the TEGO defects (C-O, C=O and COOH) that act as active redox sites [43,101]. On the contrary, the Ni-TEGO displayed the expected two peaks associated with the oxidation to NiOOH and with the reduction to $Ni(OH)_2$ in the voltage window 0 V – 0.6 V [102]. The stability voltage window results tightened to 0.55 V at 2 mV/s due to both the nickel substrate and to nickel NPs presence, which act as catalysts for the water evolution (Figure 5.2.1 b) [52].

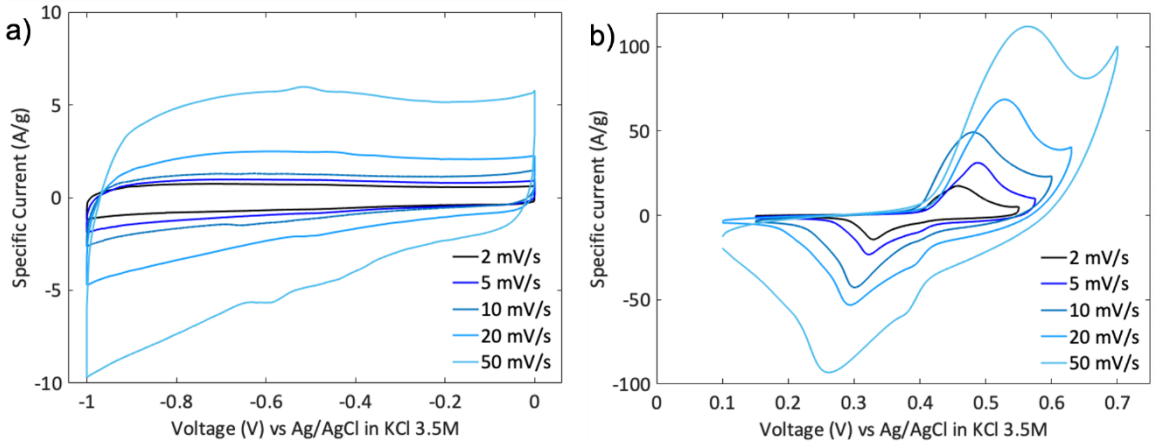

Figure 5.2.1: Three-electrodes cyclic voltammetry curves of TEGO (a) and $Ni(OH)_2$-TEGO performed at different voltage scan rates.

Thus, the specific charge stored in TEGO and $Ni(OH)_2$-TEGO electrodes is evaluated as a function of the voltage scan rate. Such values are reported in the following Table 5.2.1.

Table 5.2.1. $Ni(OH)_2$-TEGO and TEGO specific charge storable, evaluated by three-electrodes CV as a function of ν.

		2 mV/s	*5 mV/s*	*10 mV/s*	*20 mV/s*	*50 mV/s*
Specific Charge (C/g)	$Ni(OH)_2$-TEGO	1200(60)	900(50)	800(40)	504(25)	405(20)
	TEGO	310(40)	165(20)	110(15)	100(13)	95(12)

The high value of the TEGO specific capacitance, which is obtained multiplying the charge capability for the voltage difference (1 V), is ascribable to its specific surface area and to the elevated number of micro-pores [80,101]. On the other hand, the TEGO charge capability is increased by a factor between 5 to 8, thanks to the Ni nanoparticle decoration. Such enhancement is ascribable to the presence of the redox-active couples NiOOH-$Ni(OH)_2$, which promote battery-like reactions [20]. The evaluation of the charge capability enabled the charge balance between the negative and the positive electrode. Furthermore, in order to exploit the high charge capability of $Ni(OH)_2$-TEGO positive electrode, this was coupled with a negative TEGO electrode with an excess of mass. 1:8, 1:12 and 1:16 different mass ratios between the positive and the negative electrodes are investigated, to expand the stability voltage window to the maximum available [103]. Thus, the final devices, called respectively SC-1/8, SC-1/12 and SC-1/16, consisted in a standard coin cell with a glass microfiber separator, provided by Whatman™.

5.3. Two-electrodes cyclic voltammetry

The three cells, characterized in cyclic voltammetry, showed an improved stability up to about 1.5 V (Figure 5.3.1 a, b and c), overcoming the voltage limit of an aqueous electrolyte. The shapes of CV curves are peculiar, being neither rectangular, neither peak-shaped, showing a different behavior between the first part (up to 0.9 V) and the second part (between 0.9 V and 1.5 V). Precisely, in the first part, the specific current is almost constant as a function of the voltage, as for ideal SC. In fact, since the $Ni(OH)_2$ oxidation potential is about 0.45 V vs Ag/AgCl RE as shown in three electrode CV, up to a total voltage difference of 0.9 V only TEGO-related EDL-mechanisms are expected to occur. On the other hand, in the second part, it is noticeable the battery-like role of the $Ni(OH)_2$-NiOOH couple. In fact, a wide peak is shown in the reduction curve, while the oxidation curve presents a quick increase in the specific current at about 0.9 V, which, then, almost stabilizes up to 1.5 V. The current stabilization above 1 V might be due to the combined storage mechanism of the hybrid devices, being both capacitive, for the negative electrode, and battery-like for the positive one. Noteworthy, the higher mass ratio cells, i.e. SC-1/12 and SC-1/16, showed a better stability in oxidation, having a flatter shape than SC-1/8 between 1 V and 1.5 V.

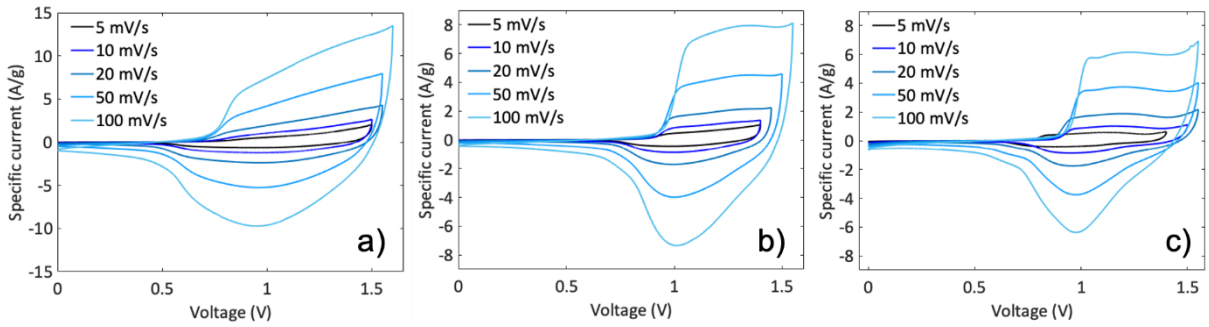

Figure 5.3.1: Two-electrodes cyclic voltammetry curves at different rates of SC. a) SC-1/8; b) SC-1/12; b) SC-1/16.

Such behavior is far from simple to explain but must be related with the mass difference between the three device negative electrodes, thus with their capacitance difference. A daring hypothesis could be that the higher capability of SC-1/12 and SC-1/16 negative electrodes are determining a slower voltage drop upon the positive electrode, thus granting a higher available reaction time to the oxidation of $Ni(OH)_2$. On the other hand, the reduction curves of SC-1/16 and SC-1/12 show a more pronounced peak than SC-1/8 around 1 V, suggesting that in the last device the reduction reactions are distributed on a wider potential range than in the other two.

5.4. Electrochemical impedance spectroscopy

Before of the CV characterization, an EIS experiment is performed for evaluating the devices ESR. The tests are carried out in the frequency range 1 Hz – 2 MHz, with a voltage wave amplitude of 10 mV, applied at the 0 V voltage difference. In fact, the shape of the EIS curves, displaying only an intercept with the real impedance axis and not exhibiting a clear semicircle at low impedance values, suggests the absence of charge-transfer processes, as expected at the 0 V difference between the electrodes, i.e. at the voltage where any redox reaction occur for the system in exam [104]. Every SC has a very low series resistance, with the SC-1/8 showing the best value (0.37 Ω). Since the devices ESR values are increasing with the TEGO mass, reaching 0.5 Ω for SC-1/12 and 0.6 Ω for SC-1/16, it is probably due to the higher TEGO mass load used.

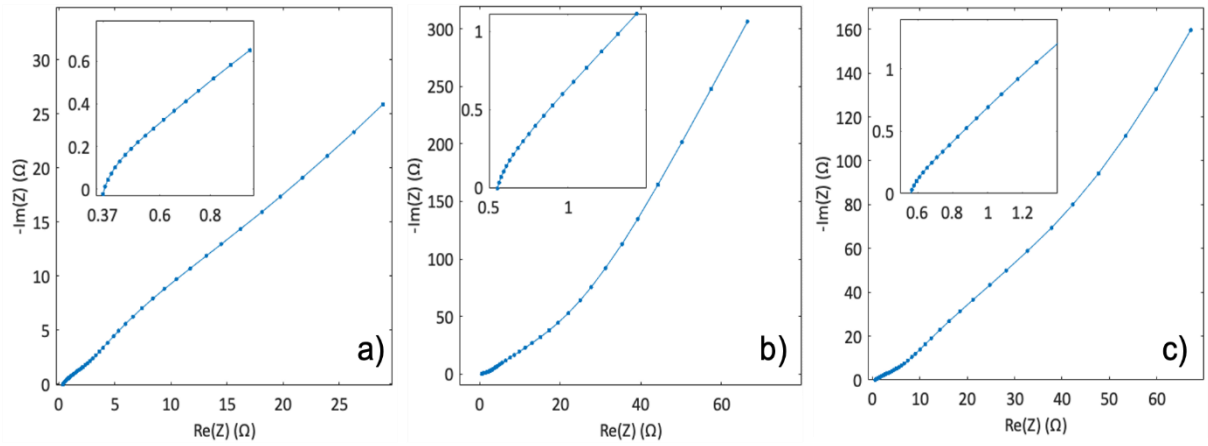

Figure 5.4.1: EIS curves of the three hybrid asymmetric supercapacitors. a) SC-1/8; b) SC-1/12; c) SC-1/16; The insets display the behavior at very high frequencies. The ESR values correspond to the intercept with the real impedance axis.

5.5. Galvanostatic charge-discharge cycles

Successively, galvanostatic charge-discharge cycles (GCDCs) are carried out with eight different current densities, namely 100 mA/g, 200 mA/g, 400 mA/g, 1 A/g, 2 A/g, 4 A/g, 10 A/g. The results are displayed in Figure 5.5.1 a, b and c. Every GCDC shows the typical shape of a hybrid device, without any plateau, typical of batteries, and without the ideal triangular shape, typical of SCs.

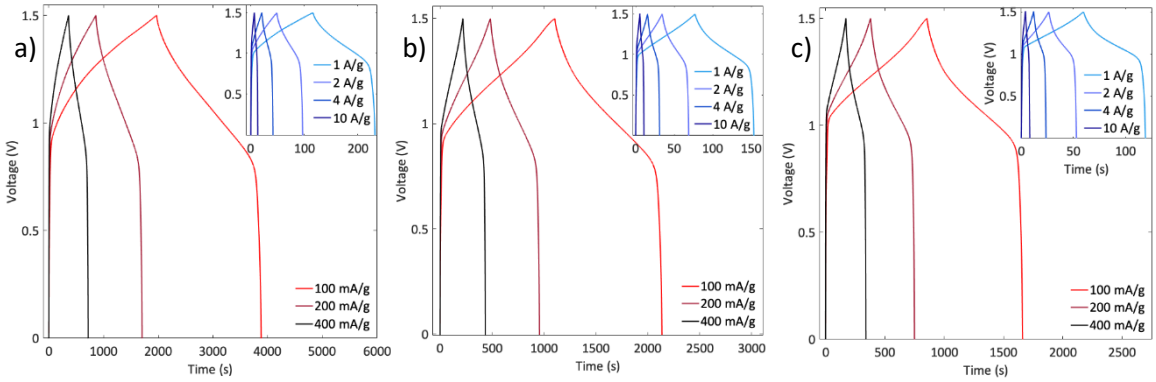

Figure 5.5.1: Galvanostatic charge-discharge cycles of the asymmetric hybrid supercapacitor performed at different current densities. a) SC-1/8; b) SC-1/12; c) SC-1/16.

Focusing deeply on the curve features, as expected, two kinetic behaviors are identified, the first is linear from 0 V up to 1 V and the second is slightly non-linear between 1 V and 1.5 V. The first one is related to the fast charging of the capacitive part of the hybrid device, due to

the presence of TEGO. The second behavior is related to the presence of $Ni(OH)_2$ in the positive electrode, which, being a battery-like material, slows the charge-discharge kinetics. Between 1 V and 1.5 V, the behavior is still almost linear, probably because of the asymmetric configuration, i.e. of the combination between a battery-like material ($Ni(OH)_2$) and a capacitive one (TEGO). Furthermore, a weak potential shift is observable between the charging and the discharging curves. Specifically, the potential shift is concomitant to the NiOOH-$Ni(OH)_2$ reaction, which starts around 1 V and 0.8 V in the charging and in the discharging process, respectively. Such potential shift, named overpotential, is common in batteries [80]. Such polarization is also evident in CV curves, either in the two-electrodes, or in the $Ni(OH)_2$-TEGO three-electrodes, from the enlargement of the peaks distance and from their potential shifting. From GCDCs, the specific energy and specific power of each cell are evaluated, as well as the capability retention over 10000 cycles performed with 200 mA/g current density. These data are shown in Figure 5.5.2 and 5.5.3.

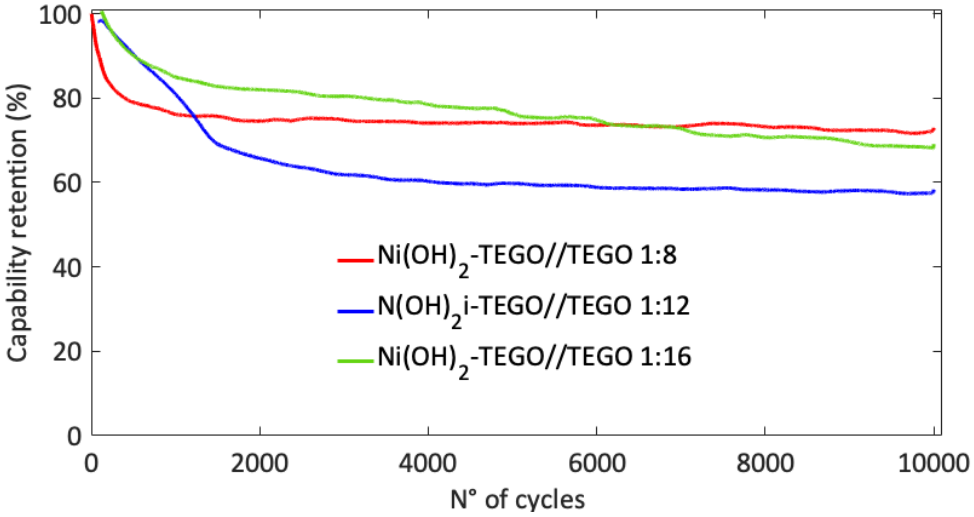

Figure 5.5.2: Capability retention comparison of SC 1/8, 1/12 and 1/16.

The measurements were carried out testing three devices, each repeated three times. The capability of the devices falls rapidly during the first two thousand cycles.

Specifically, the SC-1/12 shows initially the worst performance dropping of 31 % after 1500 cycles, but then falls slowly to the 57 % over the successive 8500 cycles. On the other hand, the SC-1/16 after 1500 cycles retains the 83 % of its initial value, then constantly decay until the 68 % after 10000 cycles. Lastly, the SC-1/8 retention drops almost immediately to the 76 % over the first thousand cycles, but then almost retains this value over the successive cycles reaching the 73% of retention at the end of the 10000 cycles. Since similar decays are common in batteries [20], thus, such initial fast decay is probably ascribable to the battery-like nature

of the positive electrode. In addition, the fact that the capability retention almost stabilizes after 2000 cycles at a values still acceptable (60 % ~ 70 % after 10k cycles) suggests that only a part of $Ni(OH)_2$ is involved in irreversible reactions. Paying attention to the morphology of $Ni(OH)_2$ on the TEGO sheets observed in STEM, which is highly disordered, it is probable that a part of the superficial $Ni(OH)_2$ detaches from TEGO, causing the loss of capability observed. Unfortunately, there is no direct evidence of such process, and it should be further investigated by post-mortem analysis. Moreover, the greater capability loss in higher SC ratios suggests that in those devices is occurring deeper charging/discharging processes than in SC-1/8 [20]. From the galvanostatic charge-discharge cycles, shown in Figure 5.5.1, the performance characteristic specific values are calculated and plotted in the Ragone plot in Figure 5.5.3.

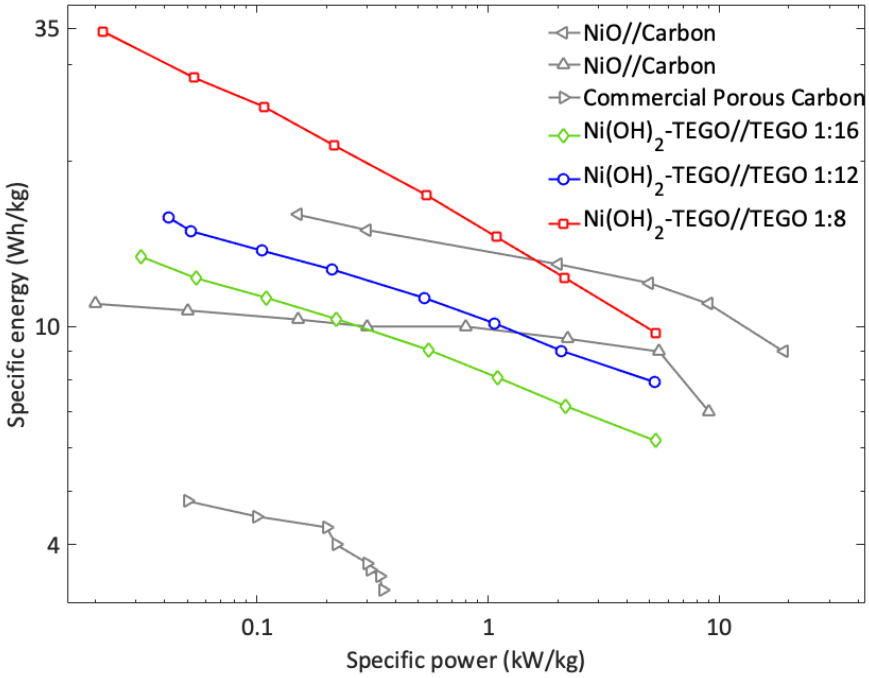

Figure 5.5.3: Ragone plot of the three hybrid asymmetric SCs compared to other literature similar devices. NiO//Carbon references: [51,105]

The SC-1/8 shows the best performance values, confirming the expectations from CV curves, and reaching the highest 34.5 Wh/kg specific energy among the three devices studied, obtained at a specific power of 21 W/kg. Incrementing the discharging rate, SC-1/8 maintains almost the 30 % of the previous specific energy but increasing its specific power of almost 200 times, reaching 7.9 kW/kg. SC-1/12 and SC-1/16, although show a lower specific energy than SC-1/8 at equal specific powers, increasing P_S exhibit a minor E_S decrease, retaining almost the

50 % of the specific energy with respect to the specific power 200 times increase. Since EDL mechanism are expected to have a faster kinetic than the redox one, the different energy dependence from the specific current of the higher mass ratios SC suggests that in SC-1/12 and SC-1/16 the capacitive effects have a major weight than in SC-1/8, which is in agreement with the previous observations. In conclusion, even though asymmetric SC capability retention decrease, and the overall performances can be improved, the performance of these devices is comparable with other literature devices with similar technology [51,105].

6. LASER INDUCED GRAPHENE MICRO-SUPERCAPACITORS

This chapter will focus on the preparation and performance evaluation of two micro-supercapacitor (m-SC) based on laser induced graphene (LIG). The idea is to exploit the planar geometry of LIG-based materials for obtaining flexible and environmentally friendly devices which might be able to power IoT technologies. Thus, aqueous gel electrolyte and eco-compatible materials, such as titanium dioxide, are used. In fact, in order to improve the performances of LIG-based m-SC, accordingly to our previous results [41], a graphene decoration with TiO_2 is implemented. The devices are characterized by means of two-electrodes CV, electrochemical impedance spectroscopy and galvanostatic charge-discharge cycles.

6.1. Micro-supercapacitor (m-SC) preparation

In order to build the m-SCs, both LIG and TiO_2 decorated LIG electrodes with interdigitated designs are contacted on the electrode side with silver paste and copper tape. The collectors were covered with a Kapton® tape for avoiding the contact with the electrolyte, as shown in Figure 6.1.1. Subsequently, a gel electrolyte, based on water and polyvinyl alcohol (PVA), is deposited onto the area between the collectors which are non-covered by the Kapton tape, as shown on the right of Figure 6.1.1. It allows to maintain the flexibility and the planarity of the device. Moreover, being the electrode material rather fragile if touched or scraped, the gel protects the electrodes from possible abrasion and ablation.

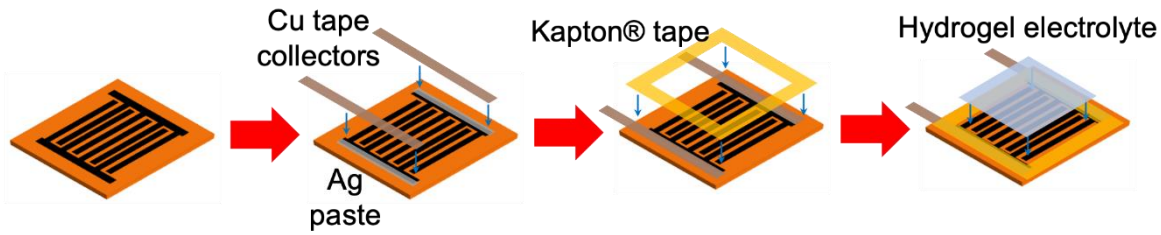

Figure 6.1.1: LIG micro-supercapacitor preparation.

For the hydrogel liquid phase, a 1M H2SO4 aqueous solution is selected. This choice is made considering the stability of the electrolyte at room conditions, the compatibility with the electrodes and based on our previous [41] and literature results [106–108]. The hydrogel is made mixing the solution 1 M of H_2SO_4 in milliQ® water with PVA, in proportion 10:1 in weight. In order to dissolve completely the PVA, and to obtain a homogeneous hydrogel, the solution is left under magnetic stirring for a couple of hours at room temperature. Then, the hydrogel is left resting for other two hours to allow the release of any entrapped bubble. Subsequently, the hydrogel is deposited, as previously described, for both LIG and TiO_2 decorated LIG micro-SCs (m-SC). In Figure 6.1.2 an example of the final m-SC is shown.

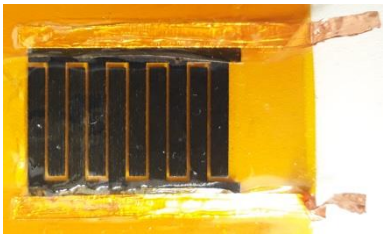

Figure 6.1.2: LIG and TiO_2-LIG m-SC appearance example.

6.2. Symmetric laser induced graphene (LIG) m-SC

In order to investigate the LIG-based m-SC performances, two-electrodes cyclic voltammetry, electrochemical impedance spectroscopy and galvanostatic charge-discharge cycles were performed.

6.2.1. Cyclic voltammetry

The two-electrodes CV experiment was performed for determining the electrochemical stability voltage window, investigating the kinetics and the behavior of symmetric LIG-based m-SC. The CV is carried out with 7 different voltage rates, going from 5 mV/s to 500 mV/s, shown in Figure 6.2.1 a) and b). The shape of the CV curve is quasi-rectangular with rounded corners, indicating a non negligible ESR [109]. The stability voltage window is about 1 V, which is near to the maximum for an aqueous electrolyte in a symmetric design.

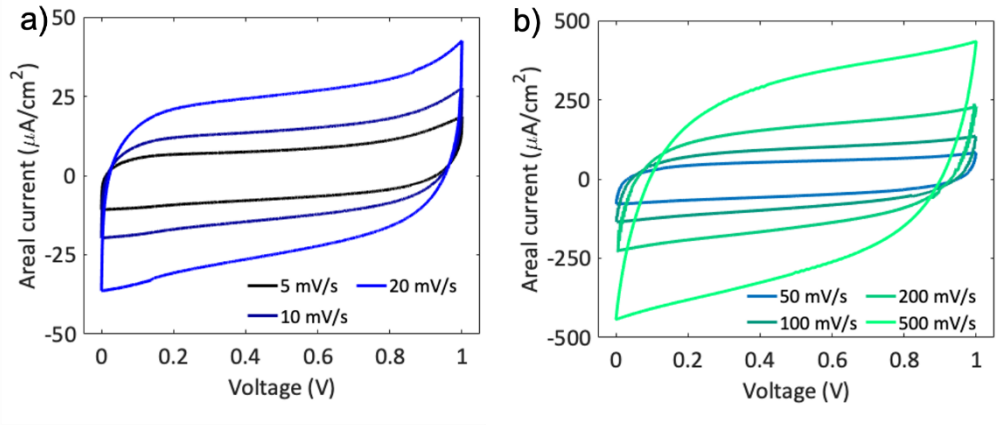

Figure 6.2.1: Cyclic voltammetry curves of LIG-based m-SC.

The capacitance dependence as a function of the voltage rate, evaluated through the CV experiment, is plotted in figure 6.2.2 a) and b). Applying the Trasatti method, the maximum areal capacitance C_T and the fast capacitance contribution C_{surf} are determined. Examining Figure 6.2.2 b), in order to extrapolate the capacitances from the linear fit, it is chosen to consider only the three slower voltage rates, following the theory described in the 3rd chapter. Such choice is made observing that the trend diverges from a linear behavior for higher rates, probably due to the non negligible ESR value [66,67].

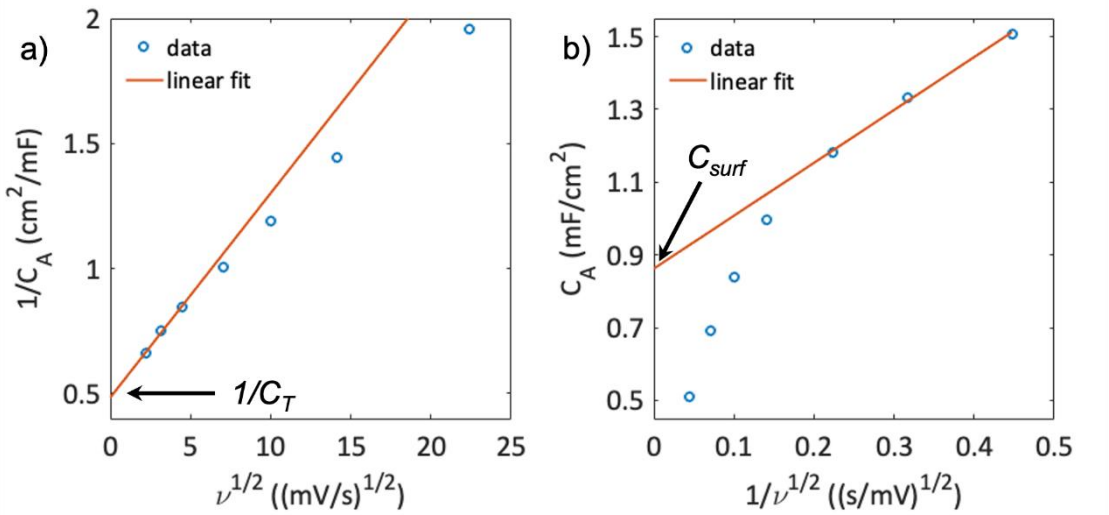

Figure 6.2.2: Behavior of the LIG-based m-SC areal capacitance as a function of the voltage scan rate applying Trasatti method. a) Inverse of the areal capacitance as a function of the scan rate square root. The vertical axis intercept coincides with the maximum value of the areal capacitance. b) Areal capacitance as a function of inverse of the scan rate square root. The intercept estimates the capacitive behaving contribution to the capacitance.

Apparently, only the 43% of the total capacitance is due to capacitive behaving processes. Although defective carbon materials can show faradaic effects related with defects and oxygen-containing groups [101], the cyclic voltammetry curves shapes suggests that the slowing kinetic factor is mostly ascribable to the device equivalent series resistance [109]. The maximum areal capacitance and the capacitive-like contribution results to be respectively, 2.06 mF/cm^2 and 0.86 mF/cm^2. It is worth noting that, in order to make comparison with other literature devices, the parameters used for describing the energy and power capability are, respectively, the areal energy and the areal power, which are calculated by the ratios between the formers and the electrodes area covered by the electrolyte. In particular, the electrodes area is evaluated with the software ImageJ analyzing the device images, such as that shown in figure 6.1.2. Since the evaluation is made for characterizing the final devices, which has substantially a planar geometry, the area of both the electrodes is evaluated neglecting the porosity of the material.

6.2.2. Electrochemical impedance spectroscopy

The electrochemical impedance spectroscopy (EIS) is carried out to evaluate the equivalence series resistance (ESR). The frequency range examined is 1 Hz – 2 MHz with a voltage amplitude pulse of 10 mV. The impedance is measured at the open circuit voltage before of the CV experiment, i.e. at a 0 V voltage difference between the electrodes. The shape of the EIS curve, displayed in figure 6.2.3, is linear for low frequencies and approaches at high frequencies the real impedance axis. As expected, any charge-transfer process, which might be revealed by an impedance arch, is observed [104]. The ESR is evaluated from the intercept with the real impedance axis and resulted of 38.6 Ω. Such value is comparable with similar m-SC resistance values of the literature [110,111] and it is also affected by the inhomogeneous LIG morphology, as described in detail in the Chapter 4.

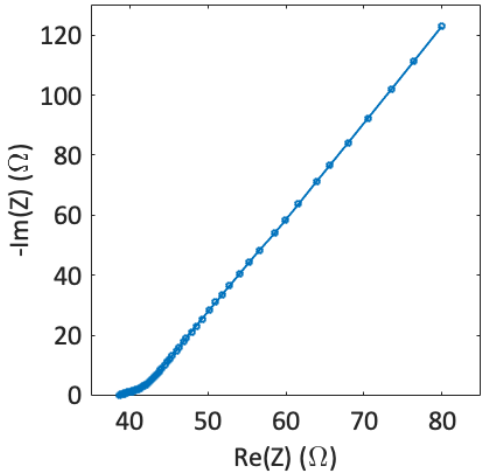

Figure 6.2.3: EIS curve of LIG-based micro-supercapacitor.

6.2.3. Galvanostatic charge-discharge cycles

Galvanostatic charge-discharge cycles (GCDCs) are used for evaluating accurately the overall m-SC performances. The shape of charge-discharge cycles, displayed in Figure 6.2.4 a) and b), is quasi-triangular with a weak distortion, which is mostly present at low specific current and could be attributed to a non-negligible leakage current at such low rates. Specifically, while the discharging time matches the charging time for areal currents higher than 20 μA/cm^2, at 10 μA/cm^2 a leakage current participates to the discharging process, determining a

discharging time (159 s) shorter than the charging time (177 s) of about 18 s. In fact, at 200 μA/cm^2, the shape of the cycle approaches the ideal triangular one.

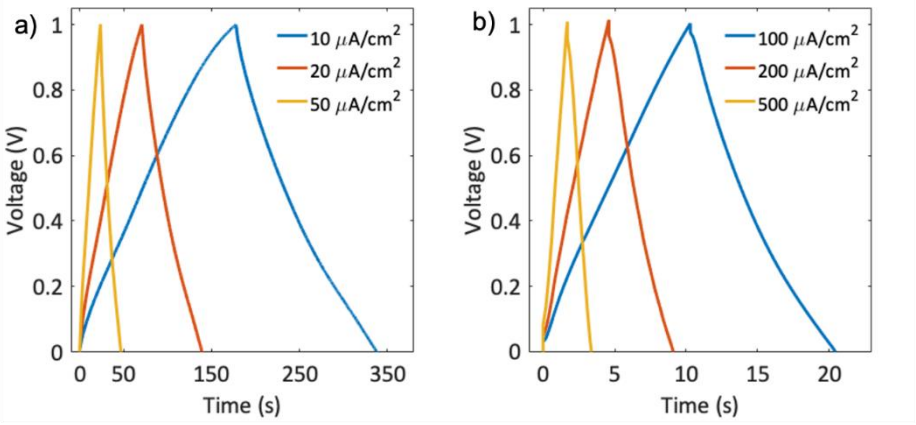

Figure 6.2.4: Galvanostatic charge-discharge cycles of LIG-based m-SC, performed at different current values. a) low current densities. b) high current densities.

Cycling the m-SC over 3500 cycles with a 200 μA/cm^2 current density, the capacitance retention and the coulombic efficiency of the system are evaluated (Figure 6.2.5). The coulombic efficiency oscillates around the maximum, certifying an almost complete reversibility of the system over the single cycle. Nevertheless, such fluctuating behavior suggests the presence of non-completely reversible reactions, probably between the graphene defects and the electrolyte ions [112], which seems to be nearly exhausted after few thousands of cycles. In fact, the capacitance retention falls to 93-94% over the first 1000 cycles, attesting the exhaustion of irreversible reactions, then it is maintained almost constant over 2500 cycles, suggesting an excellent reversibility of the residual storage mechanisms.

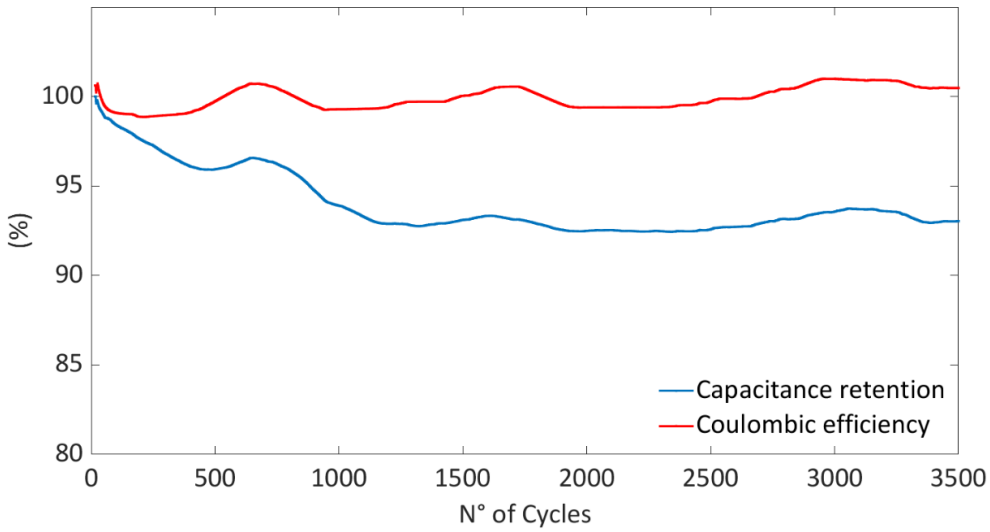

Figure 6.2.5: Capacitance retention and coulombic efficiency of LIG-based m-SC over 3500 charge-discharge cycles.

From the galvanostatic cycles the areal capacitance, the energy density and the power density are evaluated and synthetized in the Table 6.2. The energy density, starting from a maximum value of 221 nWh/cm^2 at 10 μA/cm^2 drops to the 54 % of its initial value at 500 μA/cm^2. A similar behavior is followed by the areal capacitance, while the power density increases 50 times. Such decrease of capacitance and energy density is related to their dependence upon the diffusion kinetics of the electrolyte ions into the graphene pores, which is mainly limited by a high value of the ESR [109,113]. Nevertheless, the m-SC measured capacitance and energy density values are comparable with other similar devices [114], as showed in the Ragone plot of Figure 6.4.2, at the end of this chapter.

Table 6.2: Power and energy densities as a function of the current density for the LIG-based m-SC.

Current density	*10 μA/cm^2*	*20 μA/cm^2*	*50 μA/cm^2*	*100 μA/cm^2*	*200 μA/cm^2*	*500 μA/cm^2*
Areal capacitance (mF/cm^2)	1.58(1)	1.39(2)	1.19(2)	1.05(2)	0.92(2)	0.86(2)
Power density (μW/cm^2)	4.9(2)	10.1(1)	25.7(4)	51.9(8)	102(2)	244(9)
Energy density (nWh/cm^2)	221(1)	193(2)	164(2)	146(2)	128(2)	119(2)

6.3. TiO_2 decorated LIG symmetric m-SC

The same analysis made for the LIG-based m-SC, are performed on the TiO_2-decorated LIG devices, as a comparison.

6.3.1. Cyclic voltammetry

The two-electrodes CV is performed with the same voltage scan rates (displayed in the Figure 6.1.2 legends) and the behavior of the m-SC seems almost equal, with quasi-rectangular CV curves, although the current densities are slightly higher. Although the CV curves does not show any particular feature, the current enhancement is attributable to the presence of TiO_2 particles which are expected to introduce fast faradaic processes in similar devices [41].

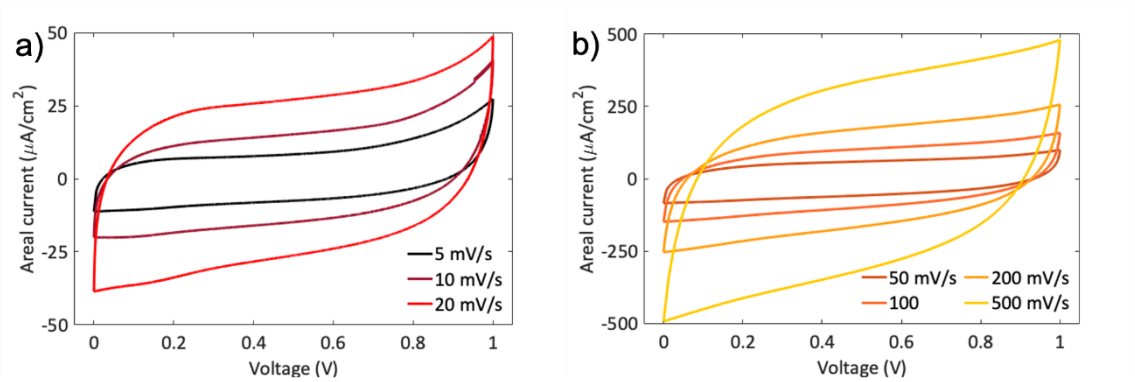

Figure 6.3.1: Cyclic voltammetry curves of TiO_2-decorated LIG m-SC performed with voltage scan rates of 5, 10, 20, 50, 100, 200 and 500 mV/s.

Applying the Trasatti method as before, the areal capacitance dependence from the voltage scan rate is valuated and plotted in Figure 6.3.2 a) and b). As previously done, only the three lower voltage rates are considered for the linear regressions. The total areal capacitance, as expected, results slightly increased to 2.17 mF/cm^2, probably due to the presence of TiO_2-related faradaic reactions, described by equation 2.12 of the 2nd chapter, here recalled [41].

$$(TiO_2)_{surface} + H_3O^+ + e^- \underset{reduction}{\overset{oxidation}{\rightleftharpoons}} (TiO_2^- H_3O^+)_{surface} \qquad \text{Eq. 2.12}$$

On the contrary, the capacitive-like contribution value remains almost equal (0.92 mF/cm^2), suggesting that the reactions introduced by the TiO_2 decoration might be diffusion controlled.

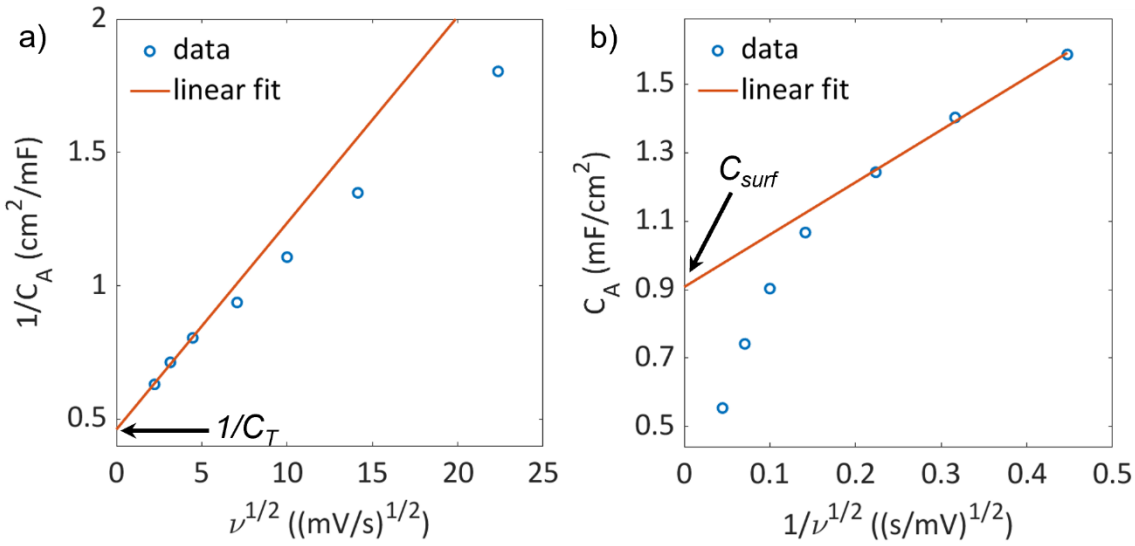

Figure 6.3.2: Behavior of the TiO_2-LIG micro-SC areal capacitance as a function of the voltage scan rate applying Trasatti method. a) Inverse of the areal capacitance as a function of the scan rate square root. The vertical axis intercept coincides with the maximum value of the areal capacitance. b) Areal capacitance as a function of inverse of the scan rate square root. The intercept estimates the capacitive behaving contribution to the capacitance.

The total expected areal capacitance of TiO_2-LIG (2.17 mF/cm^2), for v tending to zero, is higher than the LIG one (2.06 mF/cm^2) of only the 5 % of its value. In our previous work [41], the decoration with titanium oxide, obtained in a similar way, more than doubled the specific capacitance and the specific energy of graphene-based electrodes. Thus, here the TiO_2 contribute is unexpectedly low, suggesting that only a small part of the TiO_2 decorations participate to the electrochemical storage process.

6.3.2. Electrochemical impedance spectroscopy

The ESR of the TiO_2-LIG m-SC is evaluated with EIS with a voltage wave amplitude of 10 mV applied at the open circuit voltage. The frequency range investigated is 1 Hz – 2 MHz. The resulting curve has an identical behavior to the LIG one, i.e. without charge-transfer semicircle and with a single real impedance axis intercept, but, noteworthy, it shows a lower equivalent series resistance (31.8 Ω).

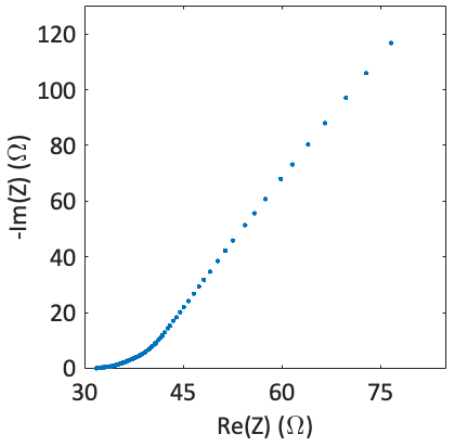

Figure 6.3.3: EIS curve for TiO_2 decorated LIG m-SC.

Such impedance decrease is compatible with an increase in the material conductivity, which, although not proved directly, could be related to a different graphene morphology of TiO_2-LIG with respect the bare LIG. In fact, as shown in the SEM images in Chapter 4, the TiO_2-LIG displays a more macro-porous and uniform structure than the bare LIG. Moreover, as suggested from the Raman spectroscopy analysis of LIG as a function of the converted region (i.e. the center or the edge of the conversion laser spot), the areas with higher macropore density have a lower defectiveness ($1.0(3) \times 10^{11}$ defects/cm^2), larger graphene sheets (lateral size of 18(3) nm) and, as a consequence, greater conductivity [101]. Such insights are compatible with the observation of a lower ESR for the TiO_2-LIG and suggests that the TiO_2 promotes a more uniform conversion of the polyimide. It is probable that the TiO2 conversion process absorbed part of the energy transferred from the laser to the polyimide, thus, lowering the LIG conversion energy. In fact, in the TiO_2 presence, the LIG presented a more macro porous morphology, as previously observed in the bare LIG at the edge of the conversion area, where the laser power density is lower.

6.3.3. Galvanostatic charge-discharge cycles

Galvanostatic charge-discharge cycles (GCDCs) are performed at the same current densities of the bare LIG characterization. The cycles shapes, even if being with a quasi-triangular shape, diverge from an ideal SC behavior mainly for the slower current densities, attesting the Nernstian processes contribution rising from the TiO_2 crystals and amorphous grains.

Specifically, the cycle shape at 10 μA/cm^2 is affected also by the presence of a leakage current, suggested by the time difference between the charging and the discharging curves. For higher current density shown in Figure 6.3.4 b), the cycle shape approaches that of the LIG-based m-SC, although maintaining a greater specific capacitance than the former. It can be noted observing the larger charge-discharge times of the cycles, which suggests that the TiO_2 contributes also with fast and superficial faradaic processes to the overall capacitance.

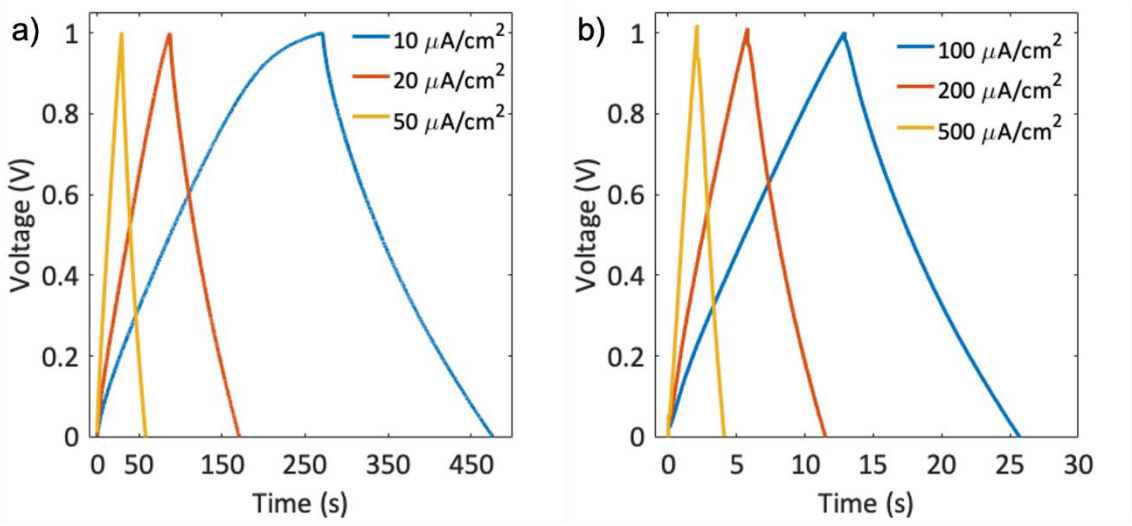

Figure 6.3.4: Galvanostatic charge-discharge cycles of LIG-based m-SC, performed at different current values.

Performing 3500 GCDCs with a current density of 200 μA/cm^2, at which the leakage current is negligible, as shown from the symmetric cycle in figure 6.3.4 b), the capacitance retention and the coulombic efficiency are evaluated.

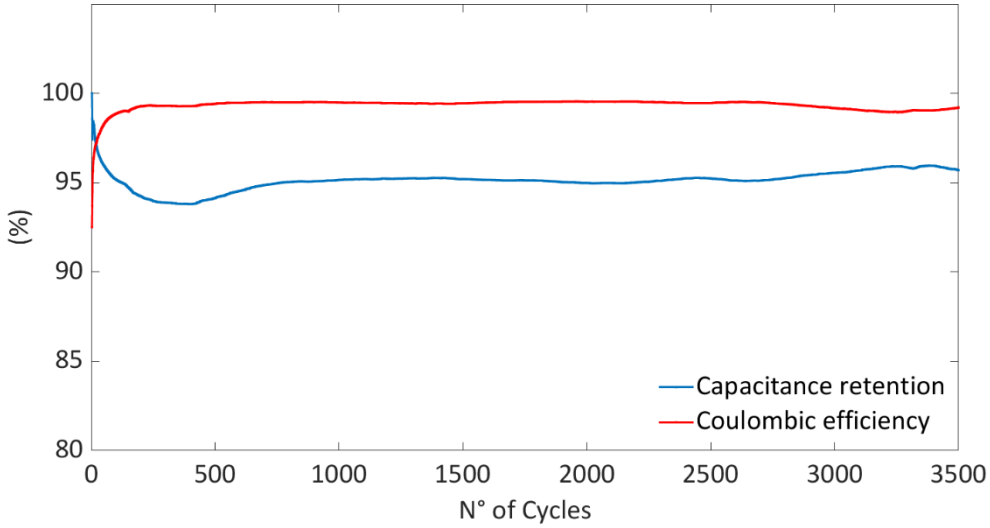

Figure 6.3.5: Capacitance retention and coulombic efficiency of TiO_2-LIG- m-SC over 3500 GCDCs.

The initial coulombic efficiency is around 93 % but suddenly increases during the first cycles, remaining then almost always constant near the maximum (99%). Consequently, the capacitance falls initially to 93% of its initial value, then increases at 95% for more than 3400 cycles. Such behavior is not simple to explain, but it could be also related to the beneficial presence of TiO_2, probably the rutile polymorph, which is already found to stabilize the reversibility of similar systems [41].

Current density	*10 μA/cm²*	*20 μA/cm²*	*50 μA/cm²*	*100 μA/cm²*	*200 μA/cm²*	*500 μA/cm²*
Areal capacitance (mF/cm²)	1.95(1)	1.71(2)	1.44(2)	1.31(2)	1.18(2)	1.05(2)
Power density (μW/cm²)	5.0(1)	10.3(1)	25.0(3)	51.1(7)	104(1.5)	255(8)
Energy density (nWh/cm²)	271(1)	237(3)	200(3)	182.5(2.5)	164(2)	146(2)

Finally, the areal capacitance, the energy and the power densities are calculated as a function of the current densities. As for the previous case examined, the energy density from 0.271 nWh/cm^2 with a related power density of 5 μW/cm^2, drops to the 54% of its initial value reaching 146 nWh/cm^2 but increasing the power density of about 50 times, reaching 255 μW/cm^2.

6.4. LIG and TiO_2-LIG comparison

In order to compare the two m-SCs, the power and energy densities are plotted together in two Ragone plots in Figure 6.4.1 a) and, compared with literature results, in Figure 6.4.2.
The parameters used in Figure 6.4.2 are the volumetric densities of power and energy, which are calculated dividing the respective areal densities by the estimated width (35 μm) of the laser induced graphene. The width estimation is carried out analyzing with ImageJ a cross

sectional image, collected with the optical microscope and shown in the inset of Figure 6.4.1 b).

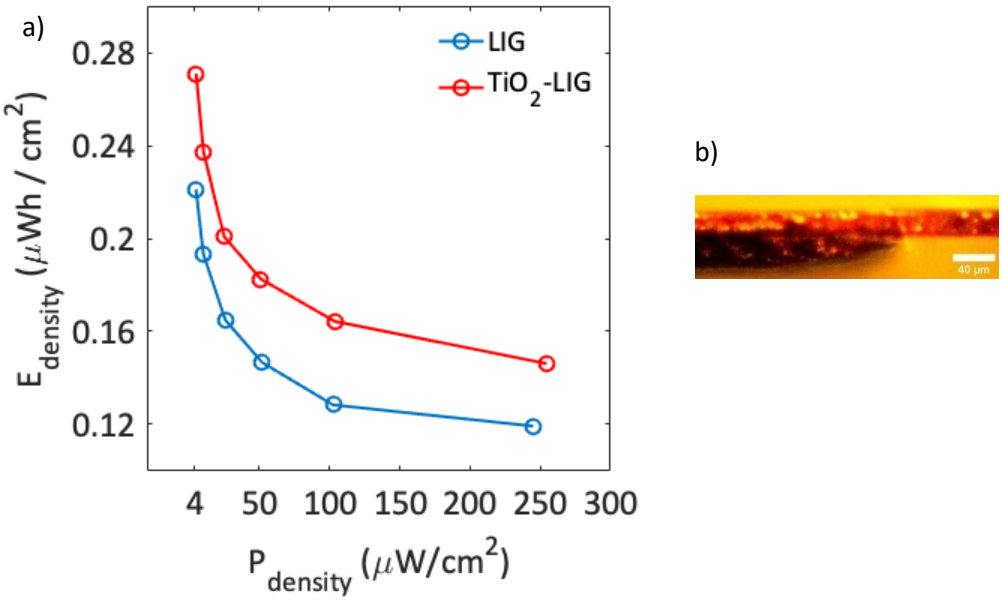

Figure 6.4.1: a) Ragone plot with the comparison of TiO_2-LIG and LIG-based m-SCs. b) cross-sectional optical microscope image of LIG.

First of all, the TiO_2 contributes actively to the energy density introducing faradaic processes, as already demonstrated in L. Fornasini, A. Morenghi et al. in an aqueous acid environment [41]. In particular, since the energy and the capacitance increase also at high current densities, it seems that either Nernstian, or capacitive-like processes, or very fast redox reactions, are present, even though the Trasatti method detected only slightly increase of the C_{surf}. The small increment of the power density of TiO_2 decorated m-SC, with respect to the non-decorated one, is ascribable to the lower ESR of the decorated one, evaluated through the EIS experiment. Secondly, the TiO_2 decoration improve even the reversibility of the system, retaining higher capacitance value than the non-decorated LIG-based m-SC, over more than 3500 charge-discharge cycles, with a 200 $\mu A/cm^2$ current density, as displayed in Figure 6.4.1. Specifically, since the Anatase is known to behave as the more active TiO_2 polymorph in storage processes, the small capacitance and energy density enhancement suggest that only a small part of the TiO_2 is in the form of Anatase. On the contrary, the improved capacitance stability of the TiO_2-LIG based m-SC suggests a considerable amount of Rutile, which is known for improving the cycle stability of similar electrochemical systems [41]. Such insights are in agreement with the Raman spectroscopy analysis, shown in the Chapter 4. In fact, the TiO_2 resulted mainly in form of multiphase structures, containing either amorphous, rutile or

anatase fractions. The poor capacitance enhancement suggests that the amorphous phase, as the rutile phase, is poorly active in storage processes.

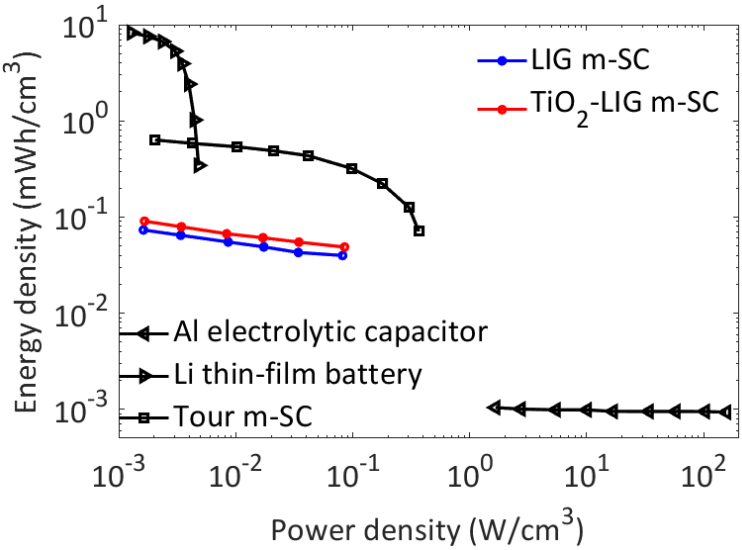

Figure 6.4.2: Ragone plot with the comparison of TiO_2-LIG and LIG-based m-SCs with other literature systems [114].

The LIG-based m-SCs performance places in the middle between the aluminum-based electrolytic capacitors and the Li-based thin-film batteries. With respect to the LIG-based SCs, the Al electrolytic capacitors have greater power density, while the thin-film Li-based batteries can store a higher amount of energy in an equal volume. On the other hand, LIG-SCs deliver the energy 10 to 20 times faster than Li-based thin-film batteries and have a two order of magnitude greater energy density than Al-based capacitors. Comparing with the Tour LIG-based m-SCs state-of-art, our LIG-based micro-SCs are performing in comparatively way in terms of power density, but they still are 10 times lower in energy capability [114].

In order to improve such performances, the laser conversion method must be further optimized. First of all, the morphology uniformity must be improved, and this is expected to be reached by optimizing the laser writing parameters, such as laser power and speed. Such conversion optimization might enable to maximize the conductivity, thus lowering the equivalence series resistance, and also to tune the LIG porosity.

Secondly, a uniform laser power distribution, thus uniform conversion to graphene, is expected to convert the TiO_2 precursor in in the TiO2 polymorphs in a more reliable way. Such optimizations could be obtained investigating a wider range of laser power, laser scanning speeds, and/or operating with the laser in a defocusing mode, i.e. with the substrate out of the focus point, controlling more accurately the laser power and the overlapping between

successive conversion areas. Unfortunately, all these parameters could not be finely tunable in the laser cut machine we have available for this study. However, such preliminary encouraging results enabled us to start a collaboration with a company for the production and optimization of a laser machine, entirely dedicated to the LIG production.

7. TEGO-BASED LI-ION CAPACITOR

7.1. Introduction

This chapter will focus on asymmetric and hybrid capacitors with lithium-based organic electrolyte and TEGO, which is used as both the negative and the positive electrode. The concept behind this application is to exploit the large electrochemical stability window of the organic electrolyte coupled with the TEGO ability to store charges at a high rate. In fact, TEGO is able to substitute the graphite as a negative electrode in batteries, thus, working in the potential window 0.05 V - 1.5 V with respect to the metallic lithium potential. As already demonstrated [80], TEGO ensures a higher storage kinetics than graphite. Specifically, TEGO exploits both the lithium intercalation between the few-layered planes and the EDL, formed at the surface and inside the nanopores, as described in Figure 7.1. On the other hand, as a positive electrode, thus working between 1.5 V and 3 V with respect to lithium, TEGO is expected to act mainly as a capacitive material.

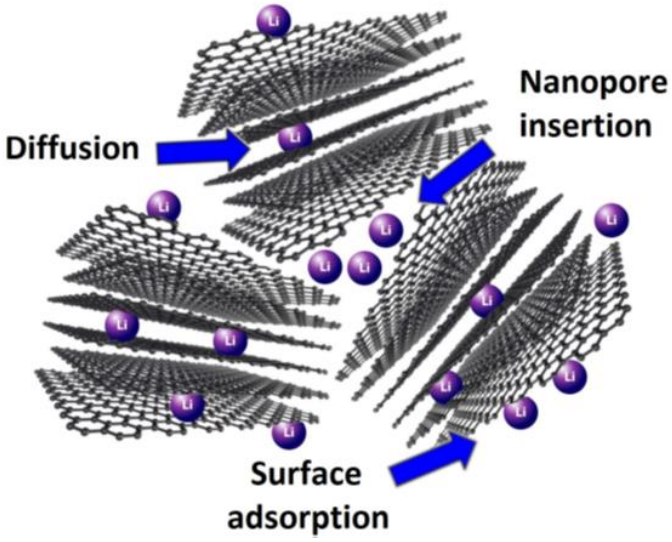

Figure 7.1: Intercalation (diffusion inside the graphene planes) and EDL mechanisms of Lithium in TEGO [80].

7.2. Three electrodes cyclic voltammetry

In the following experiments, three-electrode CV is carried out in a three-arms swagelok-type cell in an Ar-filled glovebox, using metallic lithium as both the reference and the counter electrode and TEGO as working electrode. The employed electrolytes consisted in $LiClO_4$ and $LiPF_6$, dissolved in a solution 1:1 in weight of ethylene carbonate (EC) and dimethyl carbonate (DMC).

First of all, the behavior of TEGO with $LiClO_4$ and with $LiPF_6$ electrolytes is evaluated with three electrode CV in the voltage window 1 V – 3 V (Figure 7.2.1) with respect to metallic lithium reference electrode, where TEGO is expected to work mainly as a capacitive electrode [80,115]. Such experiment enabled to select the best electrolyte for the asymmetric hybrid supercapacitor. As expected, TEGO works as a quasi-ideal capacitive electrode with both the considered electrolytes, showing quasi-rectangular CV curves. The observed slopes are due probably to a non-negligible ESR. In fact, the CV curves present an excellent symmetry with respect to the zero current value, if the enhancement of the negative current approaching 1 V vs Li/Li^+ is neglected. Such current increase is likely related to the solid electrolyte interphase (SEI) formation, which is expected to start at such potential [80,116].

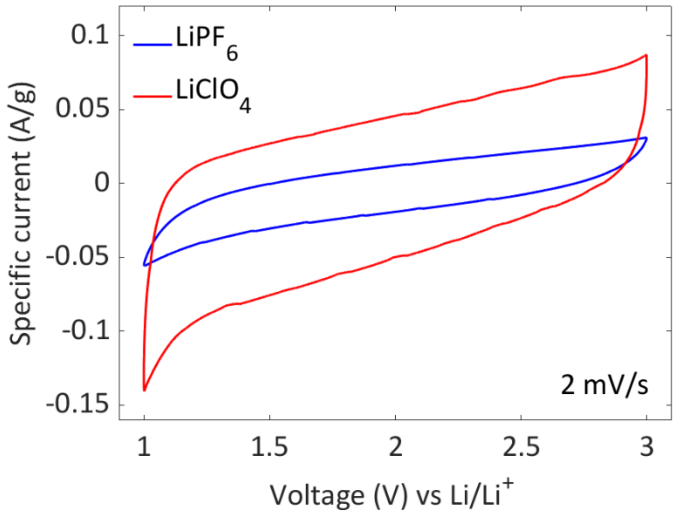

Figure 7.2.1: Comparison of TEGO performance with $LiClO_4$/EC:DMC (red curve) and with $LiPF_6$/EC:DMC (blue curve) electrolytes.

Comparing the CV curves, since the capacitance is proportional to the enclosed area, it is clear that TEGO shows a higher capacitance in presence of $LiClO_4$-based electrolyte. Such result suggests that the TEGO porosity matches better with the dimension of the perchlorate ion than the size of the hexafluorophosphate one. Thus, $LiClO_4$ in EC:DMC organic solvent is chosen for designing the asymmetric hybrid capacitor.

Since the TEGO potential, with respect metallic lithium, is about 3V, and the lithium intercalation potential of TEGO is about 0.1 V [81], it is chosen to design the hybrid capacitor coupling the bare TEGO, as a positive electrode, with TEGO intercalated with lithium, as a negative electrode. Thus, it is necessary to evaluate the behavior of TEGO at two different voltage windows, i.e. at 0.05 V - 1.5 V and at 1.5 V - 3 V. Before the evaluation as a function of the scan rate in the range 0.05 V - 1.5 V, the negative TEGO electrode must undergo a conditioning process, i.e. the SEI formation. It consists in a series of irreversible reactions that occur at the interphase between the negative electrode and the Li-based organic electrolyte [116]. Precisely, the SEI is an electronic insulating and ionic conductive layer, and its presence depends on the surface area available for storing charges. Its formation, which occur around 0.7 V vs Li/Li^+ in TEGO [80], is carried out and recorded in three electrode CV experiment. Such process is shown partially in Figure 7.2.2 for $LiClO_4$-based electrolyte and in Figure 7.2.3 for the $LiPF_6$ electrolyte.

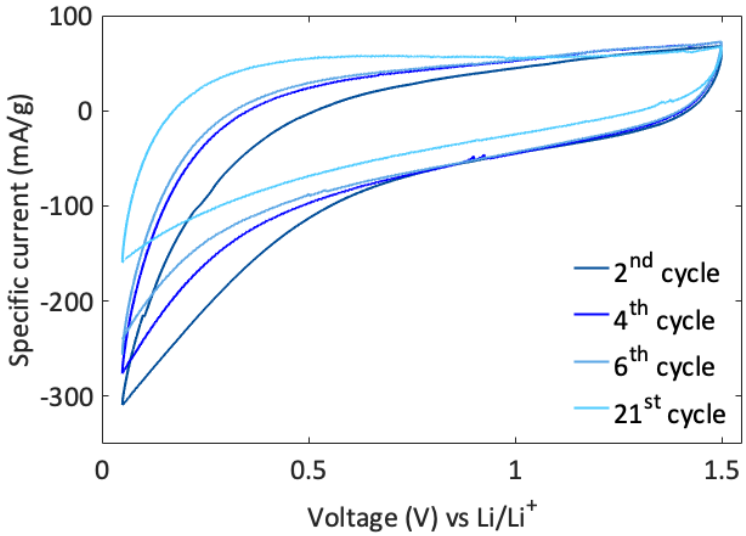

Figure 7.2.2: Visualization of the SEI formation by three-electrodes cyclic voltammetry curves of TEGO with $LiClO_4$-EC:DMC 1:1 in weight electrolyte, in the voltage windows 0.05 V - 1.5 V performed at 750 µV/s.

Since TEGO has a high specific surface area, it is expected an important loss of lithium ions involved in the SEI irreversible reactions. Unfortunately, in the case of $LiClO_4$, the very first cycle has been lost because of instrumentation issues and, being the SEI formation recorded already for TEGO/$LiPF_6$-EC:DMC, shown in Figure 7.2.3, it was reputed not necessary to repeat such time-demanding experiment, which, for instance, consisted in 25 cycles at 0.1 mV/s voltage rate, corresponding to more than 5 days of experiment for an accurate SEI formation evaluation in the $LiPF_6$ electrolyte. The SEI irreversible reactions required a high number of

charges, as confirmed, in the case of $LiPF_6$-based electrolyte, from the comparison between the very first cycle specific capacity (640 mAh/g) and the 25th cycle one (75 mAh/g), corresponding to an irreversible specific capacity of about 565 mAh/g, mainly due to SEI formation processes. Such high loss of charges is directly related to the high surface area of TEGO (about 600 m^2/g), which, being accessible to the electrolyte, is affected by the formation of the solid interphase.

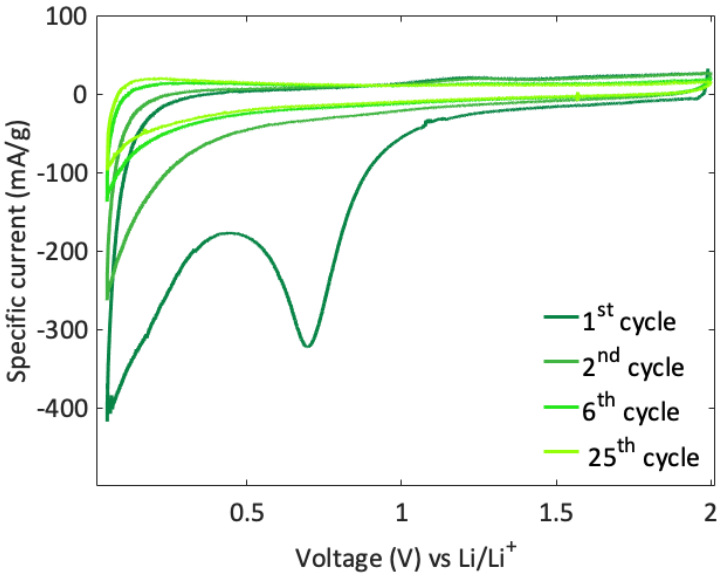

Figure 7.2.3: Visualization of the SEI formation by three-electrodes cyclic voltammetry curves of TEGO with $LiPF_6$-EC:DMC 1:1 in weight electrolyte in the voltage windows 0.05 V - 2 V performed at 100 µV/s.

However, it is evident that, after few cycles, both systems (Figure 7.2.2 and Figure 7.2.3) stabilize, suggesting the end of the SEI formation irreversible process. In fact, the voltammogram of the 21st cycle of Figure 7.2.2 is smoother and without fast current increase at the extremes, which might be associated with degradation processes, thus, allowing the successive characterization as a function of the rate with the $LiClO_4$-based electrolyte (Figure 7.2.4 a and b).

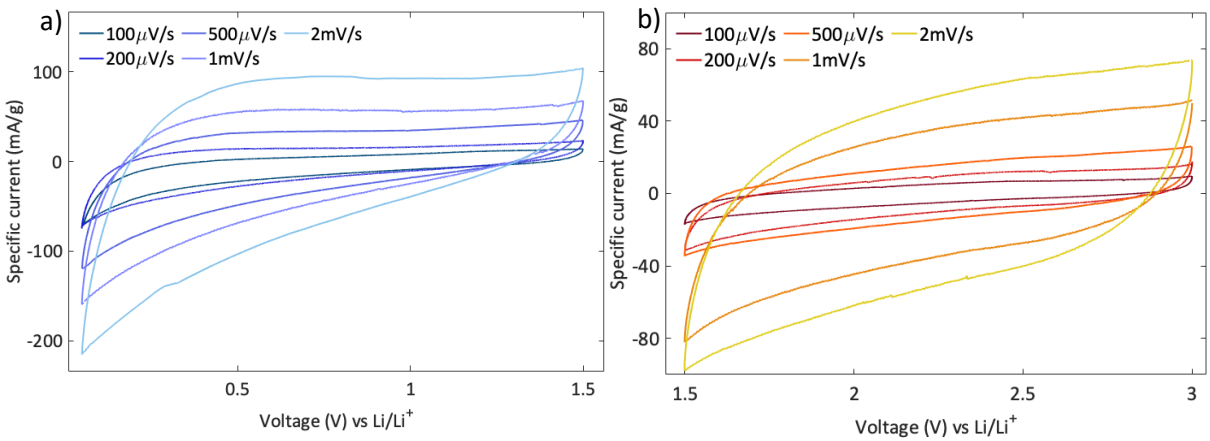

Figure 7.2.4: Three-electrodes cyclic voltammetry curves of TEGO in the voltage windows 0.05 V - 1.5 V (a) and 1.5 V – 3 V (b).

The TEGO behavior is evaluated in the voltage windows 0.05 V - 1.5 V (Figure 7.2.4 a), and 1.5 V - 3 V (Figure 7.2.4 b). In the first one (a), it is investigated the lithium intercalation, in fact, the voltammograms are asymmetrical, exhibiting a pronounced tail near 0.05 V in the reduction curve, associated with the intercalation of lithium ion in few-layered graphene [117,118]. On the contrary, even if not ideal, in the second potential range studied, the CV curves are mostly symmetrical and resemble the behavior of a capacitive material, suggesting that ClO_4^- ions are diffusing in TEGO forming the electrochemical double layer [115].

Moreover, the TEGO storing kinetics are evaluated by means of the Trasatti method previously described (3rd chapter). Thus, in Figure 7.2.5 a) and b) C_S (F/g) and $1/C_S$ (g/mAh) are plotted as a function of $v^{1/2}$ and $v^{1/2}$, respectively. Here, both the capacity (mAh/g) and capacitance (F/g) units are used in order to describe properly the system. As described in the 2nd chapter, the analysis of C_S as a function of $v^{1/2}$ returns the capacitive contribution, thus it is appropriate using F/g. On the other hand, from the analysis shown in Figure 7.2.5 a), it is evaluated the total capacity of the system, rising from both capacitive and battery-like mechanisms, thus, the unit mAh/g is more suitable.

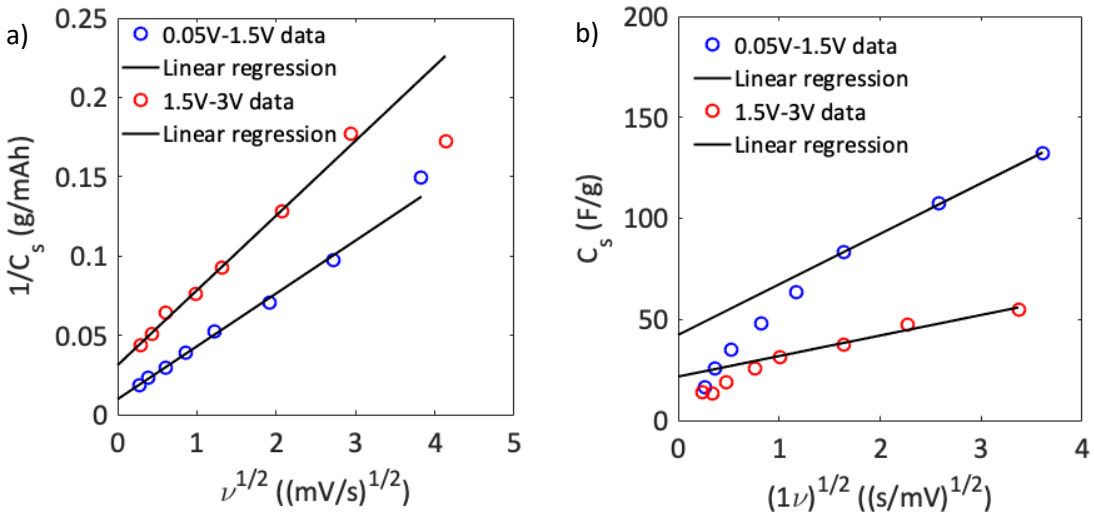

Figure 7.2.5: Graphical extrapolation applying Trasatti method of the total capacity (a) and of the capacitive-like contribute (b) of TEGO in the two different potential range.

In the voltage window 0.05 V - 1.5 V, the TEGO shows a higher maximum capacity (102(9) mAh/g) than in the window 1.5 V - 3 V (32(4) mAh/g), both in terms of capacitive effects (42(3) F/g with respect to 21(2) F/g), and in terms of diffusion-controlled processes. The specific capacity/capacitance values are obtained from the intercepts of the linear fit with the chart vertical axis of Figure 7.2.4 a) and b). As expected, being TEGO intercalating lithium, the capacity is higher for the negative electrode with respect the positive electrode, where ClO_4^- is only forming an electrical double layer at the TEGO surface. In addition, in the 0.05 V – 1.5 V window TEGO displays also a higher capacitance. Such storage difference suggests that Li^+, when does not intercalate, forms the electrical double layer on the TEGO surface, as demonstrated in S. Scaravonati, A. Morenghi et al. [80]. Since lithium ion has a smaller size than the perchlorate one, it is reasonable that TEGO stores a larger number of the former ions on its surface [119,120].

7.3. Mass electrodes balancing and cell preparation

The different specific capacity of TEGO displayed in the two considered voltage windows requires to balance the positive and negative masses following equation 2.13 of the chapter 2, in order to build an asymmetric Li-ions capacitor with equal electrode capacities. Since the

specific capacity, looking at the CV curves, is also dependent on the voltage rates, it is chosen to evaluate the capacities from the voltammograms acquired at 1mV/s, which is an intermediate scan rate between the battery and the SC kinetics. The specific capacity was found to be 25.6(7) mAh/g for the negative electrode and 13.1(5) mAh/g for the positive electrode, in which corresponds to a ratio of about 2:1 between the positive and the negative mass, respectively. The asymmetric lithium-based organic electrolyte capacitor is built using a standard coin cell CR2032. Both the electrodes were made of a TEGO slurry, obtained mixing the carbon material in a NMP solution with PAA, as a binder, and depositing it on a copper foil. As a separator, Celgard is employed. The negative electrode underwent onto a pre-lithiation process for avoiding the SEI formation in the final cell, which might deplete the electrolyte from Li-ions and hence degrade the electrolyte itself.

7.4. Electrochemical impedance spectroscopy

The tests are carried out in the frequency range 1 Hz – 2 MHz, with a voltage wave amplitude of 10 mV, applied when the capacitor is charged, hence at 3 V voltage difference. The EIS

$$Z_{CPE} = \frac{1}{a(j\omega)^b} \qquad \textit{Eq. 3.3.3}$$

curve, displayed in Figure 7.4.1, exhibits a complex behavior caused by the presence of the solid electrolyte interface, which is responsible of the arch at intermediate and high frequencies. Specifically, the EIS curve is fitted with an equivalent circuit model (inset of Figure 7.4.1) consisting in a parallel of the impedance of each electrode and of the geometric impedance, in series with the ESR. As discussed in the Chapter 3, a CPE consists in a variable capacitance in parallel with a variable resistance as described by eq. 3.3.3 of the 3rd chapter, below recalled.

The first branch represents the geometric CPE, thus, due to the geometry of the electrochemical cell, the coin cell contribution. The second branch describes the negative electrode impedance, consisting mainly in the SEI contribution. Specifically, it is composed by a CPE, which describes the ion polarization at the electrode-electrolyte interphase, in series with the interphase ionic charge-transfer resistance. The third branch represents the porous

positive electrode; thus, the CPE represents the capacitance and the leakage resistance related to the ionic polarization at double layer, while R_{EDL} represents the resistance to the diffusion in the electrode. Each parameter is evaluated fitting the EIS data and are summarized in Table 7.4.

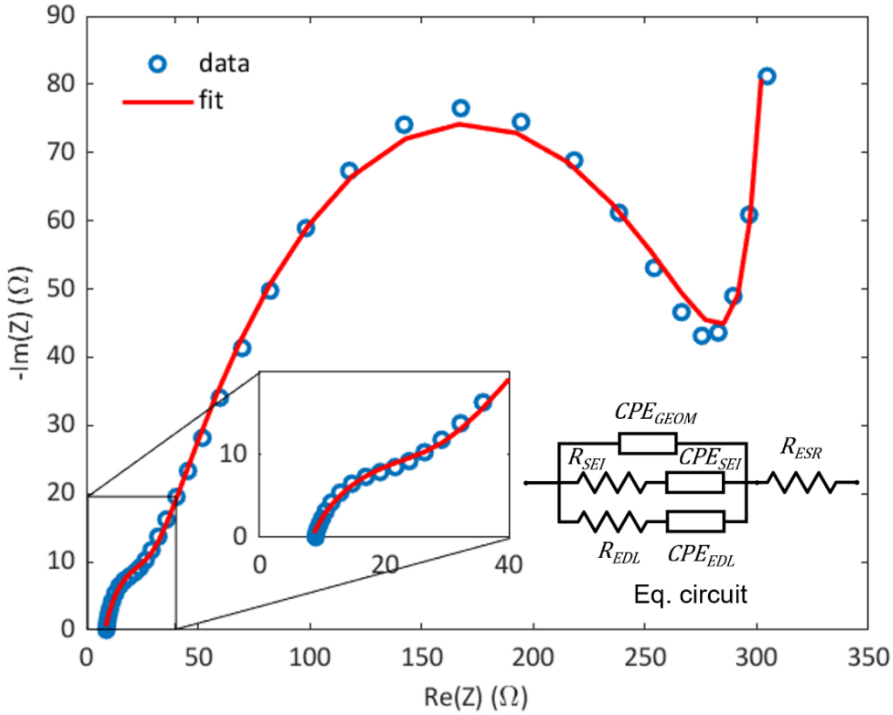

Figure 7.4.1: EIS curve of the final Li-ion capacitor. In the inset is shown the magnification at the intercept which corresponds to the ESR value. Inset: Equivalent circuit model used for fitting the EIS data.

Table 7.4: Parameter values of the equivalent circuit of the inset of Figure 7.4.1, which is used for EIS data analysis. The parameters a and b are the coefficient of the CPE impedance described by equation 3.3.3.

element	*GEOMETRIC CPE*	*SEI*	*EDL*	*ESR*
a_{CPE}	$2.3(1)\times10^{-5}$	$3(1)\times10^{-2}$	$2.7(1)\times10^{-4}$	-
b_{CPE}	0.68	0.94	0.61	-
***R*(Ω)**	-	303(9)	27(3)	8.4(1)

As described in the Chapter 3, a *b* coefficient equal to 1 means that the CPE equals to a capacitance without any leakage resistance. Thus, the SEI has a low leakage resistance, while the geometric capacitance and the EDL capacitance have non-negligible leakages. Regarding the resistances in series, the EDL-related resistance might be due to complex system of pores interconnection [73]. On the contrary, the SEI resistance is strictly related with the local structure of the interphase and, although not monitored, could change during the life cycle of the cell [116]. The last parameter determined is the ESR, which directly affects the SC performances and is an estimation of the total resistance upon the cell. Its sizeable value might be due mainly to the ionic resistance of the organic electrolyte [109].

7.5. Two electrodes cyclic voltammetry

The CV performed on the complete device shows that the system is stable, as expected, up to 2.75 V - 3 V. At higher applied voltage, at least for the lower scan voltage rate examined, the cell exhibits some instabilities, represented by a sudden current increase, probably related to the beginning of lithium plating at the negative electrode. Such process occurs when the negative electrode reaches the 0 V with respect metallic Li. Moreover, the CV curves have a quasi-rectangular shape, suggesting that the capacitive contribution is comparable with the diffusion-controlled one, as also proved by the previously analysis with Trasatti method. In fact, up to 2 V applied voltage, only EDL mechanisms is expected to occur, hence no redox peaks are observable. On the other hand, above 2 V two broad peaks are visible in Figure 7.5 (a), one at 2.5 V in the oxidation curve, and another at 2.3 V in the reduction curve, which might be associated with the lithium intercalation in the negative electrode.

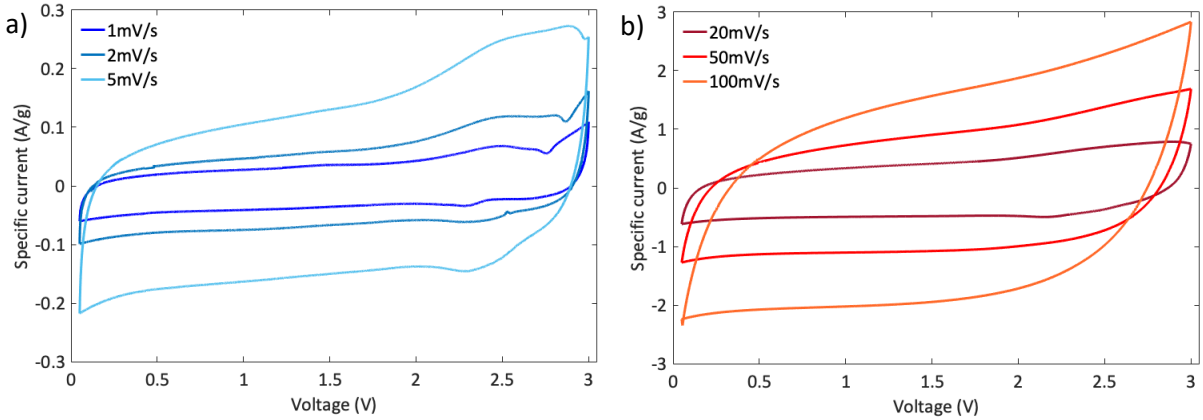

Figure 7.5. Two electrodes cyclic voltammetry of TEGO/$LiClO_4$-EC:DMC/TEGO capacitor at different voltage scan rates.

7.6. Galvanostatic charge-discharge cycles

Galvanostatic charge-discharge cycles, displayed in Figure 7.6.1, are performed on the TEGO based Li hybrid capacitor between 0 V to 2.75 V, at seven different current densities, namely at 5 mA/g, 10 mA/g, 50 mA/g, 100 mA/g, 200 mA/g, 500 mA/g and 1 A/g, and allow to calculate the specific energy and the specific power. The GCDCs shape outlines a behavior between a capacitive and a battery-like material, thus, without a potential plateau and without a linear voltage dependence on time. Although, it reaches the linear behavior at 1 A/g (shown in the inset of Figure 7.6.1 b).

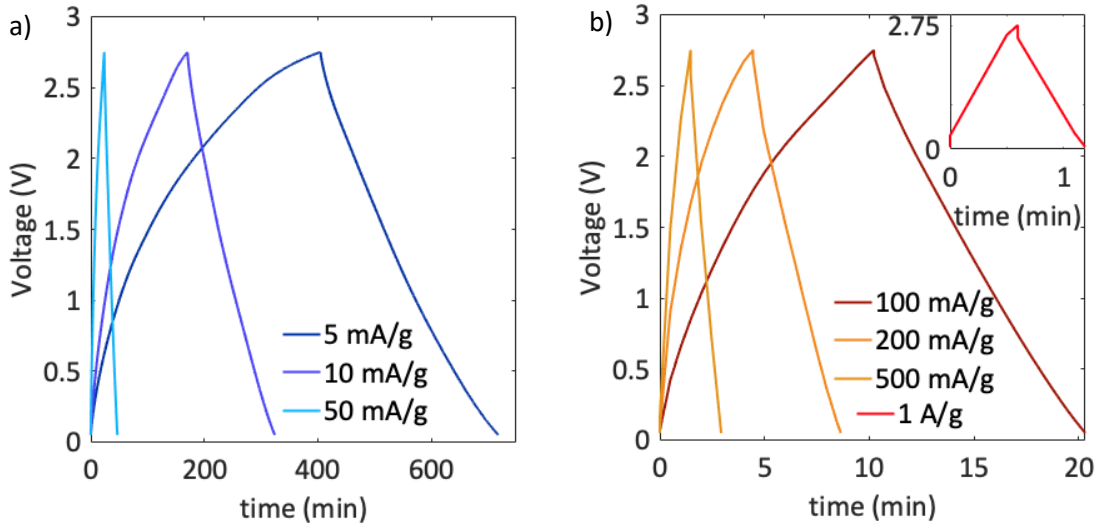

Figure 7.6.1: Galvanostatic charge-discharge cycles of the lithium-based capacitor performed at different current densities between 0V and 2.75V.

It is worth noting that for slower cycles (at 5 mA/g and 10 mA/g), the charging time is longer than the discharging time, while for faster cycles the two times substantially match each other. This suggests the presence of a leakage current comparable with the smaller current densities, thus, of the order of µA, being the electrodes total mass 1.8 mg. Then, the capacity retention and the coulombic efficiency, displayed in the Figure 7.6.2, are evaluated over 2000 cycles performed at 200 mA/g. The capacity drops during the first 500 cycles to the 73% of its initial value, then, stops to fall and oscillates between 73% and 70% for the successive 1500 cycles. On the other hand, the coulombic efficiency, which is evaluated on each single cycle, after an initial 90% value, that last for 50 cycles, is stabilized on the 97%.

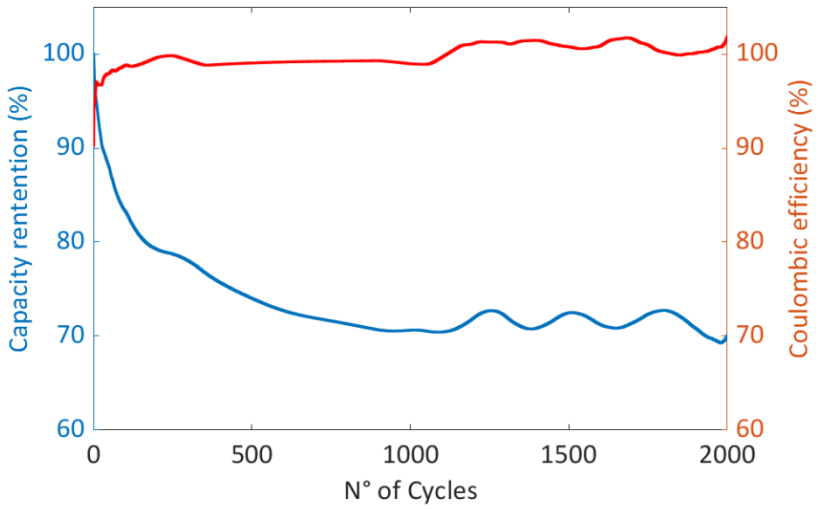

Figure 7.6.2. *Capacity retention and coulombic efficiency evaluated over 2000 GCD-cycles with a 200 mA/g current density.*

The initial drop of the capacity, such as the initial coulombic efficiency, might be due to a non-complete formation of the SEI and/or to its evolution during the first thousand cycles [80,116]. Nevertheless, since after 1000 cycles the capacity stabilizes and the coulombic efficiency reaches almost the maximum value, it could be that, once the SEI is completely formed the capacitor is able to maintain a good reversibility even after 2000 cycles. Such hypothesis could be eventually confirmed performing an operando monitoring of the EIS impedance related to the SEI.

Moreover, from galvanostatic charge-discharge cycles, the specific energy as a function of the specific power is calculated and graphed in Figure 7.7.

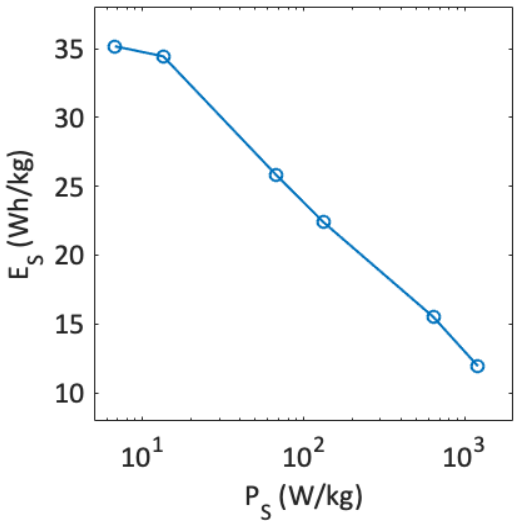

Figure 7.7: Specific energy as a function of the specific power for the TEGO-based Li-Ion capacitor, evaluated from the GCDCs previously presented.

The TEGO-based Li hybrid capacitor displays a 12(1) Wh/kg specific energy at the 1 A/g specific current, thus delivering a high specific power (1.21(1) kWh/kg). Such valuable performance must be attributed to the TEGO exploitation. In fact, being a few-layered graphene [39], it grants a high charge storing pace, profiteering from both fast Li intercalation and EDL mechanisms [80].

8. CONCLUSIONS

The aim of this work was to investigate different typologies of supercapacitors based on graphene and graphene-based materials. Two different graphene-based materials were employed and optimized for the application in supercapacitor electrodes and three supercapacitor designs were investigated. The main concept behind this thesis was to investigate hybrid supercapacitors exploiting the strength of both battery and supercapacitor technology.

8.1 TEGO/Ni-TEGO based supercapacitor

An aqueous supercapacitor based on TEGO, as negative electrode, and on TEGO-decorated with Ni-NPs, as positive electrode, was built.

Thanks to the decoration with nickel, electrochemically oxidized to nickel oxide-hydroxide and deeply investigated by TEM, p-XRD, Raman spectro-electrochemistry and three-electrodes CV, the charges storing ability of TEGO has improved, going from 110 C/g to 800 C/g at 10 mV/s.

Such high enhancement must be attributed to the introduction of the NiOOH/$Ni(OH)_2$ redox-active couple, obtained through an in-situ and operando oxidation of the TEGO Ni-NPs decorations, as proved in A. Morenghi et al. [46].

Then, the final device is obtained by coupling the Ni-TEGO battery-like positive electrode with TEGO capacitive-like negative electrode. Two-electrodes CV tests confirmed that the device was able to overcome the voltage window limit of aqueous electrolytes, reaching an operational voltage of 1.5 V.

Furthermore, three different mass ratios between the positive and the negative electrode were investigated and compared. The 1/8 mass ratio device showed the best specific energy, reaching 34.5 Wh/kg at a 40 mA/g specific current and a maximum specific power of 7.9 kW/kg maintaining a 12 Wh/kg specific energy. On the other hand, SC-1/12 and SC-1/16 showed the

best energy dependence upon the specific power, losing only half of the energy storable increasing the specific power to 7.9 kW/kg. The specific energies and powers of Ni-TEGO based SCs are comparable with the SCs state-of-market [121] and with other literature SCs based on similar technologies [50–53,105,122]

Concerning the capability retention, the three devices retained between the 57% and the 73% of their initial capability over 10000 cycles, with the best performance reached by SC-1/8. Nevertheless, their performances in terms of capability retention must be further improved, in order to match the standard life span of a supercapacitor (>100000 cycles). Thus, further operando analysis, such as EIS operando experiments or operando spectroscopic techniques, might be performed to understand the mechanisms that affects these device efficiencies and capacity retentions

8.2 LIG-based micro-supercapacitors

Laser induced graphene synthesis was successfully employed and improved introducing TiO_2 micro-particles decoration, through a one-pot and easily scalable synthesis reaction. This strategy has been already successfully employed to produce high performance m-SCs with the Lightscribe® technology, exploiting the low power laser of a DVD burner. Here, the technique was successfully extended to LIG based devices.

The morphologies were investigated in depth with SEM and Raman spectroscopy, revealing that both the polyimide and the titania precursor were efficiently converted during the laser treatment. After the termoconversion, rutile and anatase microparticles were found upon the graphene sheets.

Then, symmetric m-SCs were built exploiting a hydrogel electrolyte based on sulfuric acid. Their performances were evaluated by two-electrodes CV, electrochemical impedance spectroscopy and galvanostatic charge-discharge cycles.

Both LIG and TiO_2-LIG showed a good capacitive behavior, with quasi-rectangular CV curves. Moreover, through the Trasatti method, the maximum capacitances and the capacitive-like contributions are calculated.

Finally, the areal and volumetric energy density, the areal power density and the capacitance retention were evaluated. The TiO_2-LIG showed an improved performance retaining more capacitance and storing more energy at equal power density than LIG-based m-SC.

It is worth noting, that the decoration with TiO_2 not only boosted the performances of the m-SC introducing fast redox reactions, but also improved the homogeneity of conversion, suggested by SEM images, and proved by the smaller ESR measured in EIS.

The m-SCs reached higher power density than thin-film Li-ion batteries and higher energy density than electrolytic capacitors. Nevertheless, their energy density is still lower than to the state-of-art m-SCs based on similar technology, as the laser apparatus employed for this study needs to be further optimized for this specific application [114].

For this purpose, this study disclosed to a collaboration of our research group with a company for developing a laser cut machine specifically dedicated to LIG synthesis.

8.3 TEGO-based Li-Ion capacitor

A hybrid Li-ion capacitor based on TEGO electrodes was developed, using Li-based organic electrolyte and exploiting the peculiar combined capacitive and electrochemical charge storage mechanism of TEGO [80].

First of all, it was investigated the behavior of TEGO with two different Li salts based electrolytes. We found that$LiClO_4$ dissolved in EC:DMC) grants a larger TEGO capacitance than $LiPF_6$ in the voltage window 1V – 2.5 V vs Li/Li^+. Such difference could be related with a better fitting of TEGO pores with the ClO_4^- ions [120].

Thus, with the $LiClO_4$-based electrolyte, three-electrode CV was performed on TEGO. At higher potentials, TEGO showed a predominant capacitive behavior. On the other hand, at lower potentials, the CV curve exhibited features related to the Li-ion intercalation. In fact, the maximum total capacity of the TEGO negative electrode, extrapolated by the Trasatti method, resulted almost 3 times larger than for the TEGO positive electrode. Moreover, for the negative electrode, even the non-diffusion-controlled process contribution was enhanced. Such features are due the simultaneous intercalation (diffusion-controlled processes) and adsorption (EDL mechanisms) of Li-ions in the few-layered TEGO, as previously proved in S. Scaravonati, A. Morenghi et al. [80].

Then a capacitor using a mass ratio of 1:2 between the negative and the positive electrodes was produced and characterized in CV, GCD cycles and EIS.

The device performed halfway between a supercapacitor and a battery, exhibiting quasi-triangular charge-discharge profiles. The SC impedance evaluation exhibited a complex behavior associated with the SEI presence and leakage resistances of the interphases.

From GCD cycles the coulombic efficiency, the capacity retention, the specific energy and the specific power are evaluated. The coulombic efficiency, after an initial 90% value, is stabilized around 97% over 2000 cycles. On the other hand, the capacity retention initial decay suggests that TEGO might need a long time of conditioning in order to achieve stability. It could be related to a non-complete formation of the SEI during the first cycles. In order to understand deeply such mechanisms, operando EIS experiment could be performed, investigating the eventual evolution of the SEI by monitoring its impedance.

Concerning the energy and power densities, the SC achieved a high 35 Wh/kg at 7 W/kg, retaining a good 12 Wh/kg at the 1.2 kW/kg specific power, thus delivering very good performance as compared with other Li-ion capacitor based on carbon materials [115,118].

Nevertheless, better understanding the processes occurring at the interphases might enable to optimize its performances. Moreover, the decoration of TEGO with metal or metal oxide nanoparticles, is expected to further boost these results.

BIBLIOGRAPHY

[1] Our World in Data, (n.d.). https://ourworldindata.org/ (accessed December 4, 2022).

[2] K. Ferreira, W. Marques, D. Santos, A. César, R. Medina, Sizing of Supercapacitor and BESS for peak shaving applications; Sizing of Supercapacitor and BESS for peak shaving applications, 2019.

[3] P. Simon, Y. Gogotsi, Materials for electrochemical capacitors, in: Nanoscience and Technology: A Collection of Reviews from Nature Journals, World Scientific, 2010: pp. 320–329.

[4] C.M. Costa, J.C. Barbosa, R. Gonçalves, H. Castro, F.J.D. Campo, S. Lanceros-Méndez, Recycling and environmental issues of lithium-ion batteries: Advances, challenges and opportunities, Energy Storage Mater. 37 (2021). https://doi.org/10.1016/j.ensm.2021.02.032.

[5] M.E. Sahin, F. Blaabjerg, A. Sangwongwanich, A Comprehensive Review on Supercapacitor Applications and Developments, Comprehensive Review on Supercapacitor Applications and Developments. Energies. (2022) 15. https://doi.org/10.3390/en15030674.

[6] Y. Wu, H. Gao, Optimization of fuel cell and supercapacitor for fuel-cell electric vehicles, IEEE Trans Veh Technol. 55 (2006) 1748–1755. https://doi.org/10.1109/TVT.2006.883764.

[7] P. Rodatz, O. Garcia, L. Guzzella, F. Büchi, M. Bärtschi, A. Tsukada, P. Dietrich, R. Kötz, G. Scherer, A. Wokaun, Performance and operational characteristics of a hybrid vehicle powered by fuel cells and supercapacitors, SAE Technical Papers. (2003). https://doi.org/10.4271/2003-01-0418.

[8] A. Burke, H. Zhao, Applications of Supercapacitors in Electric and Hybrid Vehicles, (2015).

[9] Z. Zhang, X. Zhang, W. Chen, Y. Rasim, W. Salman, H. Pan, Y. Yuan, C. Wang, A high-efficiency energy regenerative shock absorber using supercapacitors for renewable energy applications in range extended electric vehicle, Appl Energy. 178 (2016) 177–188. https://doi.org/10.1016/J.APENERGY.2016.06.054.

[10] E. Pipitone, G. Vitale, A regenerative braking system for internal combustion engine vehicles using supercapacitors as energy storage elements - Part 1: System analysis and modelling, J Power Sources. 448 (2020) 227368. https://doi.org/10.1016/J.JPOWSOUR.2019.227368.

[11] M. Uddin, F. Romlie, M. Faris Abdullah, A. Halim, A. Halim, A. Bakar, T.C. Kwang, A review on peak load shaving strategies, (2017). https://doi.org/10.1016/j.rser.2017.10.056.

[12] C. Lethien, J. Le Bideau, T. Brousse, Challenges and prospects of 3D micro-supercapacitors for powering the internet of things, Energy Environ Sci. 12 (2019) 96–115. https://doi.org/10.1039/C8EE02029A.

[13] E. Frackowiak, Carbon materials for supercapacitor application, Physical Chemistry Chemical Physics. 9 (2007) 1774–1785. https://doi.org/10.1039/B618139M.

[14] L. Yu, G.Z. Chen, Ionic liquid-based electrolytes for supercapacitor and supercapattery, Front Chem. 7 (2019) 272. https://doi.org/10.3389/FCHEM.2019.00272/BIBTEX.

[15] F. Béguin, V. Presser, A. Balducci, E. Frackowiak, Carbons and electrolytes for advanced supercapacitors, Advanced Materials. 26 (2014) 2219–2251.

[16] A. Muzaffar, M.B. Ahamed, K. Deshmukh, J. Thirumalai, A review on recent advances in hybrid supercapacitors: Design, fabrication and applications, Renewable and Sustainable Energy Reviews. 101 (2019) 123–145. https://doi.org/10.1016/J.RSER.2018.10.026.

[17] D.P. Chatterjee, A.K. Nandi, A review on the recent advances in hybrid supercapacitors, J Mater Chem A Mater. 9 (2021) 15880–15918. https://doi.org/10.1039/D1TA02505H.

[18] A. Afif, S.M. Rahman, A. Tasfiah Azad, J. Zaini, M.A. Islam, A.K. Azad, Advanced materials and technologies for hybrid supercapacitors for energy storage – A review, J Energy Storage. 25 (2019) 100852. https://doi.org/10.1016/J.EST.2019.100852.

[19] Y. Shao, M. El-Kady, J. Sun, Y. Li, … Q.Z.-C., undefined 2018, Design and mechanisms of asymmetric supercapacitors, ACS Publications. 118 (2018) 9233–9280. https://doi.org/10.1021/acs.chemrev.8b00252.

[20] S. Natarajan, M. Ulaganathan, V. Aravindan, Building next-generation supercapacitors with battery type Ni(OH)2, J Mater Chem A Mater. 9 (2021). https://doi.org/10.1039/d1ta03262c.

[21] S.W. Kimmel, B.J. Hopkins, C.N. Chervin, N.L. Skeele, J.S. Ko, R.H. Deblock, J.W. Long, J.F. Parker, B.M. Hudak, R.M. Stroud, D.R. Rolison, C.P. Rhodes, Capacity and phase stability of metal-substituted α-Ni(OH) 2 nanosheets in aqueous Ni–Zn batteries, Mater Adv. 2 (2021) 3060–3074. https://doi.org/10.1039/D1MA00080B.

[22] M.E. Şahin, F. Blaabjerg, A. Sangwongwanich, A Comprehensive Review on Supercapacitor Applications and Developments, Energies 2022, Vol. 15, Page 674. 15 (2022) 674. https://doi.org/10.3390/EN15030674.

[23] A. Yu, V. Chabot, J. Zhang, Electrochemical supercapacitors for energy storage and delivery: Fundamentals and applications, 2017. https://doi.org/10.1201/b14671.

[24] T. Brousse, D. Bélanger, J.W. Long, To Be or Not To Be Pseudocapacitive?, J Electrochem Soc. 162 (2015) A5185–A5189. https://doi.org/10.1149/2.0201505JES/XML.

[25] B.E. Conway, Electrochemical supercapacitors: scientific fundamentals and technological applications, Springer Science & Business Media, 2013.

[26] V.I. Birss, B.E. Conway, J. Wojtowicz, The role and utilization of pseudocapacitance for energy storage by supercapacitors, (1997).

[27] Allen J. Bard and Larry R. Faulkner, Electrochemical Methods: Fundamentals and Applications, New York: Wiley, 2001, 2nd ed., Russian Journal of Electrochemistry. 38 (2002) 1364–1365. https://doi.org/10.1023/A:1021637209564.

[28] C. Zhong, Y. Deng, W. Hu, J. Qiao, L. Zhang, J. Zhang, A review of electrolyte materials and compositions for electrochemical supercapacitors, Chem Soc Rev. 44 (2015) 7484–7539. https://doi.org/10.1039/C5CS00303B.

[29] C.L. Berhaut, D. Lemordant, P. Porion, L. Timperman, G. Schmidt, M. Anouti, Ionic association analysis of LiTDI, LiFSI and LiPF 6 in EC/DMC for better Li-ion battery performances, RSC Adv. 9 (2019) 4599–4608. https://doi.org/10.1039/C8RA08430K.

[30] L. Borchardt, M. Oschatz, S. Kaskel, Tailoring porosity in carbon materials for supercapacitor applications, (2014). https://doi.org/10.1039/c3mh00112a.

[31] K.S. Novoselov, S. V Morozov, T.M.G. Mohinddin, L.A. Ponomarenko, D.C. Elias, R. Yang, I.I. Barbolina, P. Blake, T.J. Booth, D. Jiang, J. Giesbers, E.W. Hill, A.K. Geim, Electronic properties of graphene, Phys. Stat. Sol. (b). 244 (2007) 4106–4111. https://doi.org/10.1002/pssb.200776208.

[32] M.D. Stoller, S. Park, Z. Yanwu, J. An, R.S. Ruoff, Graphene-Based ultracapacitors, Nano Lett. 8 (2008) 3498–3502. https://doi.org/10.1021/NL802558Y/ASSET/IMAGES/LARGE/NL-2008-02558Y_0002.JPEG.

[33] C.K. Chua, M. Pumera, Chemical reduction of graphene oxide: a synthetic chemistry viewpoint, Chem Soc Rev. 43 (2013) 291–312. https://doi.org/10.1039/C3CS60303B.

[34] A.E.F. Oliveira, G.B. Braga, C.R.T. Tarley, A.C. Pereira, Thermally reduced graphene oxide: synthesis, studies and characterization, J Mater Sci. 53 (2018) 12005–12015.

[35] D. Pontiroli, M. Aramini, M. Gaboardi, M. Mazzani, S. Sanna, F. Caracciolo, P. Carretta, C. Cavallari, S. Rols, R. Tatti, L. Aversa, R. Verucchi, M. Riccò, Tracking the hydrogen motion in defective graphene, Journal of Physical Chemistry C. 118 (2014) 7110–7116.

[36] R. Ye, D.K. James, J.M. Tour, Laser-induced graphene, Acc Chem Res. 51 (2018) 1609–1620.

[37] M.F. El-Kady, V. Strong, S. Dubin, R.B. Kaner, Laser scribing of high-performance and flexible graphene-based electrochemical capacitors, Science (1979). 335 (2012) 1326–1330. https://doi.org/10.1126/SCIENCE.1216744/SUPPL_FILE/EL-KADY-SOM.PDF.

[38] F. Banhart, J. Kotakoski, A. V. Krasheninnikov, Structural defects in graphene, ACS Nano. 5 (2011) 26–41. https://doi.org/10.1021/NN102598M/ASSET/IMAGES/LARGE/NN-2010-02598M_0003.JPEG.

[39] C. Cavallari, S. Rols, H.E. Fischer, M. Brunelli, M. Gaboardi, G. Magnani, M. Riccò, D. Pontiroli, Neutron scattering study of nickel decorated thermally exfoliated graphite oxide, Int J Hydrogen Energy. 44 (2019) 30999–31007. https://doi.org/10.1016/J.IJHYDENE.2019.09.226.

[40] R. Ye, Z. Peng, T. Wang, Y. Xu, J. Zhang, Y. Li, L.G. Nilewski, J. Lin, J.M. Tour, In Situ Formation of Metal Oxide Nanocrystals Embedded in Laser-Induced Graphene, ACS Nano. 9 (2015) 9244–9251. https://doi.org/10.1021/acsnano.5b04138.

[41] L. Fornasini, S. Scaravonati, G. Magnani, A. Morenghi, M. Sidoli, D. Bersani, G. Bertoni, L. Aversa, R. Verucchi, M. Riccò, P.P. Lottici, D. Pontiroli, In situ decoration of laser-scribed graphene with TiO2 nanoparticles for scalable high-performance micro-supercapacitors, Carbon N Y. 176 (2021) 296–306. https://doi.org/https://doi.org/10.1016/j.carbon.2021.01.129.

[42] M. Gaboardi, R. Tatti, G. Bertoni, G. Magnani, R. Della Pergola, L. Aversa, R. Verucchi, D. Pontiroli, M. Riccò, Platinum carbonyl clusters decomposition on defective graphene surface, Surf Sci. 691 (2020) 121499. https://doi.org/10.1016/J.SUSC.2019.121499.

[43] M. Gaboardi, A. Bliersbach, G. Bertoni, M. Aramini, G. Vlahopoulou, D. Pontiroli, P. Mauron, G. Magnani, G. Salviati, A. Züttel, Decoration of graphene with nickel nanoparticles: study of the interaction with hydrogen, J Mater Chem A Mater. 2 (2014) 1039–1046.

[44] A. Forner-Cuenca, E.E. Penn, A.M. Oliveira, F.R. Brushett, Exploring the Role of Electrode Microstructure on the Performance of Non-Aqueous Redox Flow Batteries, J Electrochem Soc. 166 (2019) A2230–A2241. https://doi.org/10.1149/2.0611910JES/XML.

[45] U. Patil, S.C. Lee, S. Kulkarni, J.S. Sohn, M.S. Nam, S. Han, S.C. Jun, Nanostructured pseudocapacitive materials decorated 3D graphene foam electrodes for next generation supercapacitors, Nanoscale. 7 (2015) 6999–7021.

[46] A. Morenghi, S. Scaravonati, G. Magnani, M. Sidoli, L. Aversa, R. Verucchi, G. Bertoni, M. Riccò, D. Pontiroli, Asymmetric supercapacitors based on nickel decorated graphene and porous graphene electrodes, Electrochim Acta. 424 (2022) 140626. https://doi.org/10.1016/J.ELECTACTA.2022.140626.

[47] D.S. Hall, D.J. Lockwood, C. Bock, B.R. MacDougall, Nickel hydroxides and related materials: a review of their structures, synthesis and properties, Proceedings of the Royal Society A: Mathematical, Physical and Engineering Sciences. 471 (2015). https://doi.org/10.1098/RSPA.2014.0792.

[48] N. Parveen, M. Hwan Cho, Self-Assembled 3D Flower-Like Nickel Hydroxide Nanostructures and Their Supercapacitor Applications OPEN, (2016). https://doi.org/10.1038/srep27318.

[49] J. Xu, C. Yang, Y. Xue, C. Wang, J. Cao, Z. Chen, Facile synthesis of novel metal-organic nickel hydroxide nanorods for high performance supercapacitor, Electrochim Acta. 211 (2016) 595–602. https://doi.org/10.1016/J.ELECTACTA.2016.06.090.

[50] H.M. Yadav, N.C.D. Nath, J. Kim, S.K. Shinde, S. Ramesh, F. Hossain, O. Ibukun, J.J. Lee, Nickel-Graphene nanoplatelet deposited on carbon fiber as binder-free electrode for electrochemical supercapacitor application, Polymers (Basel). 12 (2020). https://doi.org/10.3390/POLYM12081666.

[51] D.W. Wang, F. Li, H.M. Cheng, Hierarchical porous nickel oxide and carbon as electrode materials for asymmetric supercapacitor, J Power Sources. 185 (2008) 1563–1568. https://doi.org/10.1016/J.JPOWSOUR.2008.08.032.

[52] Hao Jiang, Ting Zhao, Chunzhong Li, Jan Ma, Hierarchical self-assembly of ultrathin nickel hydroxide nanoflakes for high-performance supercapacitors, J Mater Chem. 21 (2011) 3818–3823. https://doi.org/10.1039/C0JM03830J.

[53] Y. Liu, R. Wang, X. Yan, Synergistic effect between ultra-small nickel hydroxide nanoparticles and reduced graphene oxide sheets for the application in high-performance asymmetric supercapacitor, Sci Rep. 5 (2015) 11095.

[54] S. Deabate, F. Henn, S. Devautour, J.C. Giuntini, Conductivity and Dielectric Relaxation in Various Ni(OH)[sub 2] Samples, J Electrochem Soc. 150 (2003) J23. https://doi.org/10.1149/1.1573203/XML.

[55] P. Prasannalakshmi, N. Shanmugam, A.S. kumar, N. Kannadasan, Phase-dependent electrochemistry of TiO2 nanocrystals for supercapacitor applications, Journal of Electroanalytical Chemistry. 775 (2016) 356–363. https://doi.org/10.1016/J.JELECHEM.2016.06.027.

[56] A. Ramadoss, S.J. Kim, Improved activity of a graphene–TiO2 hybrid electrode in an electrochemical supercapacitor, Carbon N Y. 63 (2013) 434–445. https://doi.org/10.1016/J.CARBON.2013.07.006.

[57] D. Dastan, Effect of preparation methods on the properties of titania nanoparticles: solvothermal versus sol–gel, Appl Phys A Mater Sci Process. 123 (2017) 1–13. https://doi.org/10.1007/S00339-017-1309-3/TABLES/3.

[58] Y.M. Jiang, K.X. Wang, X.X. Guo, X. Wei, J.F. Wang, J.S. Chen, Mesoporous titania rods as an anode material for high performance lithium-ion batteries, J Power Sources. 214 (2012) 298–302. https://doi.org/10.1016/J.JPOWSOUR.2012.04.091.

[59] L.L. Jiang, X. Lu, C.M. Xie, G.J. Wan, H.P. Zhang, T. Youhong, Flexible, free-standing TiO2-graphene-polypyrrole composite films as electrodes for supercapacitors, Journal of Physical Chemistry C. 119 (2015) 3903–3910. https://doi.org/10.1021/JP511022Z/SUPPL_FILE/JP511022Z_SI_001.PDF.

[60] A. Ramadoss, S.J. Kim, Improved activity of a graphene–TiO2 hybrid electrode in an electrochemical supercapacitor, Carbon N Y. 63 (2013) 434–445. https://doi.org/10.1016/J.CARBON.2013.07.006.

[61] P. Prasannalakshmi, N. Shanmugam, A.S. kumar, N. Kannadasan, Phase-dependent electrochemistry of TiO2 nanocrystals for supercapacitor applications, Journal of Electroanalytical Chemistry. 775 (2016) 356–363. https://doi.org/10.1016/J.JELECHEM.2016.06.027.

[62] S.K. Jha, R. Raj, The Effect of Electric Field on Sintering and Electrical Conductivity of Titania, Journal of the American Ceramic Society. 97 (2014) 527–534. https://doi.org/10.1111/JACE.12682.

[63] R.J. Gilliam, J.W. Graydon, D.W. Kirk, S.J. Thorpe, A review of specific conductivities of potassium hydroxide solutions for various concentrations and temperatures, Int J Hydrogen Energy. 32 (2007) 359–364. https://doi.org/10.1016/J.IJHYDENE.2006.10.062.

[64] W. Wu, S. Shabhag, J. Chang, A. Rutt, J.F. Whitacre, Relating Electrolyte Concentration to Performance and Stability for NaTi 2 (PO 4) 3 /Na 0.44 MnO 2 Aqueous Sodium-Ion Batteries , J Electrochem Soc. 162 (2015) A803–A808. https://doi.org/10.1149/2.0121506JES/XML.

[65] X. Sun, X. Zhang, K. Wang, Y. An, X. Zhang, C. Li, Y. Ma, Determination strategy of stable electrochemical operating voltage window for practical lithium-ion capacitors, Electrochim Acta. 428 (2022). https://doi.org/10.1016/J.ELECTACTA.2022.140972.

[66] S. Ardizzone, G. Fregonara, S. Trasatti, “Inner” and “outer” active surface of RuO2 electrodes, Electrochim Acta. 35 (1990) 263–267. https://doi.org/10.1016/0013-4686(90)85068-X.

[67] C. Liu, E.I. Gillette, X. Chen, A.J. Pearse, A.C. Kozen, M.A. Schroeder, K.E. Gregorczyk, S.B. Lee, G.W. Rubloff, An all-in-one nanopore battery array, Nature Nanotechnology 2014 9:12. 9 (2014) 1031–1039. https://doi.org/10.1038/nnano.2014.247.

[68] J. Wang, J. Polleux, J. Lim, B. Dunn, Pseudocapacitive contributions to electrochemical energy storage in TiO 2 (anatase) nanoparticles, Journal of Physical Chemistry C. 111 (2007) 14925–14931. https://doi.org/10.1021/JP074464W/SUPPL_FILE/JP074464WSI20070731_064452.PDF.

[69] V. Augustyn, J. Come, M.A. Lowe, J.W. Kim, P.L. Taberna, S.H. Tolbert, H.D. Abruña, P. Simon, B. Dunn, High-rate electrochemical energy storage through Li+ intercalation pseudocapacitance, Nature Materials 2013 12:6. 12 (2013) 518–522. https://doi.org/10.1038/nmat3601.

[70] C. Huang, J. Zhang, N.P. Young, H.J. Snaith, P.S. Grant, Solid-state supercapacitors with rationally designed heterogeneous electrodes fabricated by large area spray processing for wearable energy storage applications, Scientific Reports 2016 6:1. 6 (2016) 1–15. https://doi.org/10.1038/srep25684.

[71] S. Zhang, N. Pan, Supercapacitors Performance Evaluation, Adv Energy Mater. 5 (2014). https://doi.org/10.1002/aenm.201401401.

[72] R.A. Huggins, Simple method to determine electronic conductivity and ionic components of the conductors in mixed a review, Ionics (Kiel). 8 (2002) 300–313. https://doi.org/10.1007/BF02376083/METRICS.

[73] S. Fletcher, V.J. Black, I. Kirkpatrick, A universal equivalent circuit for carbon-based supercapacitors, Journal of Solid State Electrochemistry. 18 (2014) 1377–1387. https://doi.org/10.1007/S10008-013-2328-4/FIGURES/15.

[74] Z. Vlčková Živcová, M. Bouša, M. Velický, O. Frank, L. Kavan, In situ raman microdroplet spectroelectrochemical investigation of cuscn electrodeposited on different substrates, Nanomaterials. 11 (2021) 1256. https://doi.org/10.3390/NANO11051256/S1.

[75] L. Kavan, Lithium insertion into TiO2 (anatase): Electrochemistry, Raman spectroscopy, and isotope labeling, Journal of Solid State Electrochemistry. 18 (2014) 2297–2306. https://doi.org/10.1007/S10008-014-2435-X/FIGURES/4.

[76] J.C. Pramudita, D. Pontiroli, G. Magnani, M. Gaboardi, C. Milanese, G. Bertoni, N. Sharma, M. Riccò, Effect of Ni-nanoparticles decoration on graphene to enable high capacity sodium-ion battery negative electrodes, Electrochim Acta. 250 (2017) 212–218.

[77] J.C. Pramudita, A. Rawal, M. Choucair, D. Pontiroli, G. Magnani, M. Gaboardi, M. Riccò, N. Sharma, Mechanisms of Sodium Insertion/Extraction on the Surface of Defective Graphenes, ACS Appl Mater Interfaces. 9 (2016) 431–438. https://doi.org/10.1021/ACSAMI.6B13104.

[78] B.C. Brodie, Sur le poids atomique du graphite, Ann. Chim. Phys. (1860) 466–472.

[79] S.E. Drewniak, T.P. Pustelny, R. Muzyka, A. Plis, Studies of physicochemical properties of graphite oxide and thermally exfoliated/reduced graphene oxide, Polish Journal of Chemical Technology. 17 (2015) 109--114. https://doi.org/10.1515/PJCT-2015-0076.

[80] S. Scaravonati, M. Sidoli, G. Magnani, A. Morenghi, M. Canova, J.-H. Kim, M. Riccò, D. Pontiroli, Combined capacitive and electrochemical charge storage mechanism in high-performance graphene-based lithium-ion batteries, Mater Today Energy. 24 (2022) 100928. https://doi.org/10.1016/J.MTENER.2021.100928.

[81] J.C. Pramudita, D. Pontiroli, G. Magnani, M. Gaboardi, M. Riccò, C. Milanese, H.E.A. Brand, N. Sharma, Graphene and Selected Derivatives as Negative Electrodes in Sodium-and Lithium-Ion Batteries, ChemElectroChem. 2 (2015) 600–610.

[82] S.Y. Sawant, R.S. Somani, M.H. Cho, H.C. Bajaj, A low temperature bottom-up approach for the synthesis of few layered graphene nanosheets via C–C bond formation using a modified Ullmann reaction, RSC Adv. 5 (2015) 46589–46597. https://doi.org/10.1039/C5RA07196H.

[83] M.G. Stanford, J.T. Li, Y. Chyan, Z. Wang, W. Wang, J.M. Tour, Laser-Induced Graphene Triboelectric Nanogenerators, ACS Nano. (2019). https://doi.org/10.1021/acsnano.9b02596.

[84] C.A. Nunes, M.C. Guerreiro, Estimation of surface area and pore volume of activated carbons by methylene blue and iodine numbers, Quim Nova. 34 (2011) 472–476. https://doi.org/10.1590/S0100-40422011000300020.

[85] J.J. Kipling, R.B. Wilson, Adsorption of methylene blue in the determination of surface areas, Journal of Applied Chemistry. 10 (1960) 109–113. https://doi.org/10.1002/JCTB.5010100303.

[86] R. Ye, D.K. James, J.M. Tour, R. Ye, D.K. James, M. Tour, Laser-Induced Graphene: From Discovery to Translation, Advanced Materials. 31 (2019) 1803621. https://doi.org/10.1002/ADMA.201803621.

[87] Z. Wan, X. Chen, M. Gu, Laser scribed graphene for supercapacitors, (n.d.). https://doi.org/10.29026/oea.2021.200079.

[88] C. Casiraghi, A. Hartschuh, H. Qian, S. Pliscanec, C. Georgia, A. Fasoli, K.S. Novoselov, D.M. Basko, A.C. Ferrari, Raman spectroscopy of graphene edges, Nano Lett. 9 (2009) 1433–1441. https://doi.org/10.1021/NL8032697/ASSET/IMAGES/LARGE/NL-2008-032697_0013.JPEG.

[89] S.M. Jung, D.L. Mafra, C. Te Lin, H.Y. Jung, J. Kong, Controlled porous structures of graphene aerogels and their effect on supercapacitor performance, Nanoscale. 7 (2015) 4386–4393. https://doi.org/10.1039/C4NR07564A.

[90] A.C. Ferrari, Raman spectroscopy of graphene and graphite: Disorder, electron–phonon coupling, doping and nonadiabatic effects, Solid State Commun. 143 (2007) 47–57. https://doi.org/10.1016/J.SSC.2007.03.052.

[91] C. Casiraghi, Probing disorder and charged impurities in graphene by Raman spectroscopy, Physica Status Solidi (RRL) – Rapid Research Letters. 3 (2009) 175–177. https://doi.org/10.1002/PSSR.200903135.

[92] H. Yin, Y. Wada, T. Kitamura, S. Kambe, S. Murasawa, H. Mori, T. Sakata, S. Yanagida, Hydrothermal synthesis of nanosized anatase and rutile TiO 2 using amorphous phase TiO 2, (n.d.). https://doi.org/10.1039/b008974p.

[93] M. Ocaña, J. V. Garcia-Ramos, C.J. Serna, Low-Temperature Nucleation of Rutile Observed by Raman Spectroscopy during Crystallization of TiO2, Journal of the American Ceramic Society. 75 (1992) 2010–2012. https://doi.org/10.1111/J.1151-2916.1992.TB07237.X.

[94] P.P. Lottici, D. Bersani, M. Braghini, A. Montenero, Raman scattering characterization of gel-derived titania glass, J Mater Sci. 28 (1993) 177–183. https://doi.org/10.1007/BF00349049/METRICS.

[95] J. Graetz, C.C. Ahn, H. Ouyang, P. Rez, B. Fultz, White lines and d-band occupancy for the 3d transition-metal oxides and lithium transition-metal oxides, Phys Rev B Condens Matter Mater Phys. 69 (2004) 235103. https://doi.org/10.1103/PHYSREVB.69.235103/FIGURES/7/MEDIUM.

[96] E. Howe, J.D. Hanawalt, H.W. Rinn, L.K. Frevel, INDUSTRIAL ENGINEERING CHEMISTRY ANALYTICAL EDITION Harrison Chemical Analysis by X-Ray Diffraction Classification and Use of X-Ray Diffraction Patterns, (n.d.). https://pubs.acs.org/sharingguidelines (accessed March 23, 2023).

[97] D. Singh, Characteristics and Effects of γ-NiOOH on Cell Performance and a Method to Quantify It in Nickel Electrodes, J Electrochem Soc. 145 (1998) 116–120. https://doi.org/10.1149/1.1838222/XML.

[98] K.N. Patel, M.P. Deshpande, V.P. Gujarati, S. Pandya, V. Sathe, S.H. Chaki, Structural and optical analysis of Fe doped NiO nanoparticles synthesized by chemical precipitation route, Mater Res Bull. 106 (2018) 187–196. https://doi.org/10.1016/J.MATERRESBULL.2018.06.003.

[99] W. Lai, L. Ge, H. Li, Y. Deng, B. Xu, B. Ouyang, E. Kan, In situ Raman spectroscopic study towards the growth and excellent HER catalysis of Ni/Ni(OH)2 heterostructure, Int J Hydrogen Energy. 46 (2021) 26861–26872. https://doi.org/10.1016/J.IJHYDENE.2021.05.158.

[100] D.S. Hall, D.J. Lockwood, S. Poirier, C. Bock, B.R. MacDougall, Raman and infrared spectroscopy of α and β phases of thin nickel hydroxide films electrochemically formed on nickel, Journal of Physical Chemistry A. 116 (2012) 6771–6784. https://doi.org/10.1021/JP303546R/ASSET/IMAGES/LARGE/JP-2012-03546R_0011.JPEG.

[101] J. Kim, J.H. Eum, J. Kang, O. Kwon, H. Kim, D.W. Kim, Tuning the hierarchical pore structure of graphene oxide through dual thermal activation for high-performance supercapacitor, Scientific Reports 2021 11:1. 11 (2021) 1–10. https://doi.org/10.1038/s41598-021-81759-7.

[102] Y. Tian, J. Yan, L. Huang, R. Xue, L. Hao, B. Yi, Effects of single electrodes of Ni (OH) 2 and activated carbon on electrochemical performance of Ni (OH) 2–activated carbon asymmetric supercapacitor, Mater Chem Phys. 143 (2014) 1164–1170.

[103] Z. Dai, C. Peng, J.H. Chae, K.C. Ng, G.Z. Chen, Cell voltage versus electrode potential range in aqueous supercapacitors, Sci Rep. 5 (2015) 9854.

[104] A. Adán-Más, T.M. Silva, L. Guerlou-Demourgues, M.F. Montemor, Application of the Mott-Schottky model to select potentials for EIS studies on electrodes for electrochemical charge storage, Electrochim Acta. 289 (2018) 47–55. https://doi.org/10.1016/J.ELECTACTA.2018.08.077.

[105] M. Chiku, M. Toda, E. Higuchi, H. Inoue, NiO layers grown on a Ni substrate by galvanostatic anodization as a positive electrode material for aqueous hybrid capacitors, J Power Sources. 286 (2015) 193–196. https://doi.org/10.1016/J.JPOWSOUR.2015.03.095.

[106] N. Kurra, Q. Jiang, P. Nayak, H.N. Alshareef, Laser-derived graphene: A three-dimensional printed graphene electrode and its emerging applications, Nano Today. 24 (2019) 81–102.

[107] M.F. El-Kady, R.B. Kaner, Scalable fabrication of high-power graphene micro-supercapacitors for flexible and on-chip energy storage, Nat Commun. 4 (2013) 1475.

[108] J. Lin, Z. Peng, Y. Liu, F. Ruiz-Zepeda, R. Ye, E.L.G. Samuel, M.J. Yacaman, B.I. Yakobson, J.M. Tour, Laser-induced porous graphene films from commercial polymers, Nature Communications 2014 5:1. 5 (2014) 1–8. https://doi.org/10.1038/ncomms6714.

[109] W.G. Pell, B.E. Conway, Analysis of power limitations at porous supercapacitor electrodes under cyclic voltammetry modulation and dc charge, in: J Power Sources, 2001. https://doi.org/10.1016/S0378-7753(00)00682-0.

[110] F. Clerici, M. Fontana, S. Bianco, M. Serrapede, F. Perrucci, S. Ferrero, E. Tresso, A. Lamberti, In situ MoS2 Decoration of Laser-Induced Graphene as Flexible Supercapacitor Electrodes, ACS Appl Mater Interfaces. 8 (2016) 10459–10465. https://doi.org/10.1021/ACSAMI.6B00808/ASSET/IMAGES/LARGE/AM-2016-00808B_0007.JPEG.

[111] R. Ye, Y. Chyan, J. Zhang, Y. Li, X. Han, C. Kittrell, J.M. Tour, R. Ye, Y. Chyan, J. Zhang, Y. Li, X. Han, C. Kittrell, J.M. Tour, Laser-Induced Graphene Formation on Wood, Advanced Materials. 29 (2017) 1702211. https://doi.org/10.1002/ADMA.201702211.

[112] R. Raccichini, A. Varzi, S. Passerini, B. Scrosati, The role of graphene for electrochemical energy storage, Nat Mater. 14 (2015) 271–279.

[113] J.P. Zheng, J. Huang, T.R. Jow, The limitations of energy density for electrochemical capacitors, J Electrochem Soc. 144 (1997) 2026.

[114] Z. Peng, J. Lin, R. Ye, E.L.G. Samuel, J.M. Tour, Flexible and stackable laser-induced graphene supercapacitors, ACS Appl Mater Interfaces. 7 (2015). https://doi.org/10.1021/am509065d.

[115] J. Ajuria, M. Arnaiz, C. Botas, D. Carriazo, R. Mysyk, T. Rojo, A. V. Talyzin, E. Goikolea, Graphene-based lithium ion capacitor with high gravimetric energy and power densities, J Power Sources. 363 (2017). https://doi.org/10.1016/j.jpowsour.2017.07.096.

[116] S.J. An, J. Li, C. Daniel, D. Mohanty, S. Nagpure, D.L. Wood, The state of understanding of the lithium-ion-battery graphite solid electrolyte interphase (SEI) and its relationship to formation cycling, Carbon N Y. 105 (2016). https://doi.org/10.1016/j.carbon.2016.04.008.

[117] Z. Xiao, L. Zhao, Z. Yu, M. Zhang, S. Li, R. Zhang, M. Ayub, X. Ma, G. Ning, C. Xu, Multilayered graphene endowing superior dispersibility for excellent low temperature performance in lithium-ion capacitor as both anode and cathode, Chemical Engineering Journal. 429 (2022) 132358. https://doi.org/10.1016/J.CEJ.2021.132358.

[118] C. Li, X. Zhang, C. Sun, K. Wang, X. Sun, Y. Ma, Recent progress of graphene-based materials in lithium-ion capacitors, J Phys D Appl Phys. 52 (2019) 143001. https://doi.org/10.1088/1361-6463/AAFF3A.

[119] J.L. Gómez-Urbano, G. Moreno-Fernández, M. Arnaiz, J. Ajuria, T. Rojo, D. Carriazo, Graphene-coffee waste derived carbon composites as electrodes for optimized lithium ion capacitors, Carbon N Y. 162 (2020). https://doi.org/10.1016/j.carbon.2020.02.052.

[120] C. Largeot, C. Portet, J. Chmiola, P.L. Taberna, Y. Gogotsi, P. Simon, Relation between the ion size and pore size for an electric double-layer capacitor, J Am Chem Soc. 130 (2008). https://doi.org/10.1021/ja7106178.

[121] Supercapacitor Energy Storage Cells | Skeleton, (n.d.). https://www.skeletontech.com/en/skelcap-supercapacitors (accessed April 13, 2023).

[122] H.B. Li, M.H. Yu, F.X. Wang, P. Liu, Y. Liang, J. Xiao, C.X. Wang, Y.X. Tong, G.W. Yang, Amorphous nickel hydroxide nanospheres with ultrahigh capacitance and energy density as electrochemical pseudocapacitor materials, Nature Communications 2013 4:1. 4 (2013) 1–7. https://doi.org/10.1038/ncomms2932.